TEL AVIV UNIVERSITY

The Iby and Aladar Fleischman Faculty of Engineering

The Zandman-Slaner School of Graduate Studies

Frequency Mixing as a Platform for Enhanced Contrast Harmonic Imaging with Microbubbles

A thesis submitted toward the degree of

Master of Science in Biomedical Engineering

by

Keren Tchelet Karlinsky

February 22

TEL AVIV UNIVERSITY

The Iby and Aladar Fleischman Faculty of Engineering

The Zandman-Slaner School of Graduate Studies

Frequency Mixing as a Platform for Enhanced Contrast Harmonic Imaging with Microbubbles

A thesis submitted toward the degree of

Master of Science in Biomedical Engineering

by

Keren Tchelet Karlinsky

This research was carried out in the Department of Biomedical Engineering

Under the supervision of Dr. Tali Ilovitsh

February 22

Acknowledgments

I would like to thank the following people:

Dr. Tali Ilovitsh, my supervisor, for her continuous guidance and support in professional and moral, throughout the research.

Mike Bismuth for assistance in MB preparation and all Ilovitsh lab members for helpful discussions that made a substantial impact on this work.

Most of all, I would like to dedicate this thesis to my dear family and my fiancé, Lev Korchagin, for continually believing in me, supporting me, and pushing me to succeed. Their endless encouragement allowed the completion of this work.

Abstract

Ultrasound imaging is the most widely used medical imaging modality since it is non-invasive, deep penetrating, cost-effective, and capable of real-time imaging. Microbubbles serve as contrast agents in diagnostic ultrasound imaging. Contrast harmonic imaging of microbubbles takes advantage of their nonlinear properties that generate additional harmonic frequencies in the received spectrum. This enables them to separate their echoes from the surrounding tissue, which is mainly linear. By eliminating the linear components on receive, e.g. with pulse inversion technique, the obtained beam-formed image, contains only the nonlinear microbubbles signals. While this method is being clinically used, its main limitations are the nonlinearity of the tissue itself and the fact that the harmonic content is significantly weaker than the linear signal. As a result, contrast harmonic imaging suffers from limitations in contrast, signal-to-noise ratio, and generated artifacts.

The purpose of this study is to develop and validate an enhanced, real-time, contrast harmonic imaging technique. This technique relies on the excitation of microbubbles with a dual-frequency waveform. The microbubbles trigger a frequency mixing effect that generates additional frequency components in the received spectrum, including difference and sum frequencies, in addition to the standard harmonics, thus amplifying microbubbles' nonlinear response and enhancing image contrast.

Our real-time approach relies on the superposition of two single-frequency waveforms into a single dual-frequency transmission. The dual-frequency waveform is incorporated into a standard pulse inversion sequence and is transmitted by a single transducer using an arbitrary waveform generator in a programmable ultrasound system. On receive, standard dynamic receive beamforming, identical to pulse inversion, is used, without additional post-processing. The proposed method is described analytically, while numerical simulations via the Marmottant model are used to confirm the generation of the sum and difference frequencies in

the microbubble's backscattered echoes. The resulting image quality enhancement is demonstrated in tissue-mimicking phantoms containing a cavity of microbubbles suspension. A maximal contrast improvement of 3.71 dB compared to standard pulse inversion is achieved, along with a reduction by 4.5 fold in the mechanical index.

Contents

Abbreviations and symbols

US ……..……..... Ultrasound	LRI …….…….... Low resolution image
HI …….…… Harmonic imaging	HRI ……..... High resolution image
CHI …….…… Contrast harmonic imaging	BF ……..…. Beamforming
UCA ……. Ultrasound contrast agents	DAS ……..…..… Delay and sum
MB …….……... Microbubble	CNR ……..……... Contrast-to-Noise Ratio
PI ……..... Pulse-inversion	PZT ……..... Lead-zirconate-titanate
RF ……..... Radiofrequency	FOV …….....….…..... Field of view
FT ……....…….... Fourier Transform	FWHM ……..……..... Full-width-half-max
BW ……..….. Bandwidth	FDA ……... Food and Drug Administration
CR ……..…….. Contrast ratio	MI ……..….... Mechanical index
Field II …. US simulator software package	TIS …….……. Thermal index
B-mode ……..……... Brightness mode	PNP ……..... Peak negative pressure
PW…… Plane-wave	
p [MPa] ……..…….. Pressure	ω [$\frac{\text{rad}}{sec}$] ……... radial wave frequency
c [$\frac{m}{s^2}$] ……..… Speed of sound	Z [$Rayl$] ……..... Acoustic impedance
ρ [$\frac{kg}{m^3}$]……..… Density	W_i …... Apodization coefficient of element i
κ [Pa^{-1}]……Compressibility	f_R [$\frac{1}{SEC}$] ……... Frame rate
$\mathcal{F}$ …….. Fourier Transform	T_{frame} [sec] …… Time to obtain one frame
f [MHz] ……... Frequency	N ……..…. Number of scan-lines
k ……..….. Wave number	N_c…….……... Number of cycles in a pulse
Δf[MHz]……..... Frequency bandwidth	I[$\frac{W}{m^2}$]…..…….…..... Intensity
η [$\frac{kg}{m \cdot s}$]……..…… Viscosity	κ_s ……..….. Surface dilatational viscosity
d [mm] ……..….. Aperture width	σ [$\frac{N}{m}$] ……...… MB's surface tension
z [mm]……..... Depth	Δz_{axial} [mm]……..…… Axial resolution
θ [°] ……. Angle	$\Delta x_{lateral}$[mm] ……... Lateral resolution
τ [sec]……..…… Time delay	W_0[mW] ……..…….. Power
λ [mm] ……..….. Wavelength	β …….……..... Coefficient of nonlinearity
R [mm] ……. MB dynamic radius	

List of figures

List of Publications

Journal paper based on this thesis is now under review:

- **Keren T. Karlinsky** and **Tali Ilovitsh**, “Ultrasound Frequency Mixing for Enhanced Contrast Harmonic Imaging of Microbubbles” under review in *IEEE transactions ultrasonic ferroelectrics frequency control*.

Conference presentations:

- **K. Karlinsky** and **T. Ilovitsh**, “Frequency Multiplexing Ultrasound as a Platform for Enhanced Harmonic Imaging,” *Virtual APS March Meeting 2021*, Online, March 15-19, 2021. (Oral presentation).
- **K. Karlinsky** and **T. Ilovitsh**, “Multiplexed Frequency Transmit for Enhanced Harmonic Imaging with Microbubbles” *IEEE IUS2021 Virtual symposium*, September 11-16, 2021. (Oral presentation).
- **K. Karlinsky** and **T. Ilovitsh**, "Frequency Multiplexing Ultrasound as a Platform for Enhanced Harmonic Imaging", Annual retreat, Department of Biomedical Engineering, Tel Aviv University, Israel, May 2021. (Oral presentation).

1 Introduction

Since the first sonogram usage for medical diagnosis by Karl Dussik in 1942, ultrasound (US) has become one of the most widely used medical imaging modality, since it is non-invasive, deep penetrating, cost-effective, portable, and capable of real-time imaging [1], [2]. The diagnostic US has found wide application for different parts of the human body, as well as in veterinary medicine. The major imaging categories of US imaging are female breast, cardiac, gynecologic, radiology (internal organs of the abdomen), obstetrics (fetuses in vivo), vascular system, etc. [3]. Moreover, there are even specialized US applications that have been honored by their terminology, derived from the region the transducer is placed or the application process itself. For example, Laparoscopic (imaging carried out to guide and evaluate laparoscopic surgery) or Musculoskeletal (imaging of muscles, tendons, and ligaments) [4].

With hardware and software developments, diagnostic US is constantly in progress, getting optimized and new techniques and methods are invented [5]. In addition, the US has many advantages over other imaging methods. For example, there is no ionizing radiation (for example in CT and X-ray), which enables unlimited imaging time, in terms of safety concerns. In addition, it is an affordable imaging device and therefore US is much more accessible than other expensive methods, such as MRI, CT, and PET. The last is very rare, making them unavailable compared to the US [3].

Given the many benefits of a US system, new US imaging methods are being investigated and applied in clinics at a high rate [5]. However, most of the newly developed software-based US methods, especially real-time imaging, could not have come without the development of powerful and fast computers, continuing improvements in electronics, advanced hardware, etc., in the last decade [6]. Improving US performance can greatly affect the accuracy of diagnosis,

improve monitoring (e.g., cancerous tissues), and even assist in treatment's success when it is guided with US imaging. Therefore, there is no doubt that developing advanced and improved US imaging methods is essential [7].

US imaging can be divided into standard linear imaging and nonlinear imaging, where in both cases short acoustic pulses at a specific center frequency are transmitted into the human body, and the difference between them is at the receive [8]. In the first standard method, image reconstruction is based on capturing returned echoes with the same transmitted frequency, whereas in the nonlinear, the harmonic frequencies (integer multiples of the transmitted frequency) are detected and filtered with different imaging techniques to generate a contrast-enhanced US image, called harmonic image (HI) [9]. Moreover, to increase the nonlinear signal to improve HI contrast and quality, ultrasound contrast agents (UCA), are injected into the vascular beds to enhance US reflections [10]. This imaging technique is known as contrast harmonic imaging (CHI). UCA are gas-filled microbubbles (MBs) encapsulated with phospholipid shells, which have a significant nonlinear response under US excitation, that increases their back-scattering signal, compared to other soft tissues and fluids without MBs [11], [12].

Although CHI is used clinically, its main limitations are the nonlinearity of the tissue itself and the fact that the harmonic content is significantly weaker than the linear signal, and further attenuates as it propagates through the tissue. Therefore, nonlinear imaging methods are more sensitive to attenuation, noise, and artifacts [9]. When increasing the US pressure, the undesired nonlinear echoes from the tissues also increase, thus reducing the MBs signal [13]. Overall, these challenges interfere with image quality, especially under poor imaging conditions [14], [15].

To overcome that limitation, this work proposes to use an additional non-linear mechanism, called the frequency-mixing effect. This phenomenon occurs when an MB is excited by a signal, which contains several frequencies, resulting in new frequency components of their difference and sum within MB signal response, in addition to their harmonics [15], [16]. The presence of additional nonlinear components amplifies the MBs signal, leading to an increase in the resulting harmonic image quality and contrast. in CHI. This concept was suggested in several previous works, but most of them did not include MBs [17], [18], or were not practical due to the requirement of complex setup, post-processing, mechanical scanning, or pulse synchronization [19]–[21]. Therefore, the goal of this work was to simplify that and to develop a practical method with a single transducer, which provides enhanced CHI with MBs in real-time.

This thesis describes the different stages of developing a new proposed approach, from simulations to US experiments with MBs inside a phantom. To begin with, a summary of the general US imaging principles is presented in chapter 3. In addition, it includes different methods for US image formation, the common metrics, and parameters to evaluate and to characterize US imaging, the existing CHI techniques and their implementations, physical mechanisms, and limitations. At the end of the 3rd chapter, the concept of the proposed method is described. Chapter 4 presents the methods and materials, which were used for this work and the two major stages during this research. First, includes the numerical simulations of MB dynamic response to our designed multiplexed signal excitation, compared to the standard transmit signal. The second includes US experiments of our implementation, with the programmable US system in the lab. Chapter 5 performs the obtained results and the sixth chapter discusses them. Finally, the main conclusions, further work plan, and possible optimization are described in chapter 7.

2 Research objectives

As explained in the introduction, this work aims to develop an enhanced and real-time CHI of MBs based on the nonlinear mechanism of frequency mixing, to increase their nonlinear backscatter signal. For this purpose, the first milestone in the study was to prove that the frequency-mixing effect occurs within MBs. To do so, numerical simulations were implemented with matching parameters to the MBs produced in our lab. Other configurations and optimization, regarding the transmit and the waveform design, were determined after trial and error within the simulations.

The next milestone was to perform US experiments, including designing the setup and programming the US system to perform the desired imaging technique. The main goals for this stage were:

- Engineering a costumed dual-frequency US waveform, to trigger frequency-mixing within MBs suspension inside a tissue-mimicking phantom.
- Implementation of CHI, based on the traditional Pulse-Inversion (PI) technique, with the programmable US system in the lab.
- To plan a reproducible experimental protocol and a contrast evaluation metric, which provide a valid comparison between the standard PI and our purposed method for different emitted pressures.

3 Theoretical Background

For a better understanding of the written in the thesis and the proposed US imaging technique, it is necessary to present the main principles of US imaging in general and then the CHI US imaging with MBs specifically, which is the imaging method this study aims to improve. Thus, this

chapter presents the most important aspects of US imaging, including the basic physical phenomenon, commonly used transducers, imaging modalities, and evaluation metrics, based on two US books [1], [22].

3.1 Ultrasound imaging principles

The US is defined as a sound wave with frequencies ≥20 kHz, which are higher than the upper audible limit of human hearing. The US is an acoustic wave, which moves and advances by expansion and compression of the medium, through which, it is moving at a certain speed, depending on the material. Those waves can be absorbed, refracted, focused, reflected, and scattered. After World War II, inspired by sonar and radar technologies, a few medical practitioners suggested using the pulse-echo technique for the human body, for medical purposes. Of course, sonar and medical US applications have many differences. The first detects hard targets, such as metal ships in the water, and the second forms an image of soft tissues in the human body, but they both obtain spatial information of a region or an object within a medium, by receiving the backscattered acoustic signals (echo-response), of the transmitted sound waves towards them [1].

The US provides a noninvasive technique for imaging human anatomy using a transducer, which converts electrical signals to acoustic signals. In standard US imaging, short acoustic pulses at a specific center frequency are transmitted into the human body and focused to a specific depth [8]. Because of the inhomogeneity of the medium (e.g., different tissues and internal organs), the US wave is partially reflected and scattered, i.e., echoes are generated and then propagate back toward the transducer, with the same frequency spectrum [9]. The detected echoes are converted from acoustic to electrical signals by the piezoelectric elements inside the transducer. These received signals are then processed by the system's software to a grayscale

image, called a B-mode image. Each point in the B-mode image corresponds to the anatomic location of an echo-generating structure, and its brightness corresponds to the echo strength [23]. The frame rate of the imaging depends on the time required to transmit, receive and process the reflected echoes (beamforming process). At a maximum depth, z_{max}, the pulse repetition interval T_R, and the pulse repetition rate f_R, defined by [1]:

$$T_R \geq \frac{2z_{max}}{c}, \quad f_R \geq \frac{1}{T_R} \tag{1}$$

3.2 Sound propagation in a medium

A sound wave is produced when an object vibrates, creating a pressure wave (transducer's basic principle). This pressure wave causes particles in the surrounding medium (air, liquid, or solid) to have vibrational motion (kinetic energy). When the new particles "have been charged" with that energy, they repeat the process and transmit their energy to other nearby particles and then, their motion (kinetic energy) diminishes until they are affected by another passing wave [1]. That is how the sound wave travels through the medium and creates alternating compression and rarefaction (expansion) patterns, typical for longitudinal waves, as displayed in Figure 1. A longitudinal wave is a wave in which particles displacement (in a medium), is parallel to the direction of wave propagation [24]. Compression is characterized by densely packed particles, causing a high pressure, whereas rarefaction is characterized by distanced particles, causing low pressure.

Soft tissues have high water content and therefore, US waves propagation inside them can be approximated as waves propagation in liquids, although tissues are more elastic solids with complicated structures. The main difference between waves in fluids and solids is that in the first, exist only longitudinal waves, while in solids can appear also other types of waves e.g., shear

waves (particles displacement perpendicular to the direction of wave propagation) [22]. Another convenient simplification is that the waves in tissue behave linearly. That means, they keep their shape even when their amplitude is changed and when several different waves are combined, they form a superposition wave. The principle of linearity is an extremely important condition, on which most of the US imaging theory is based [1].

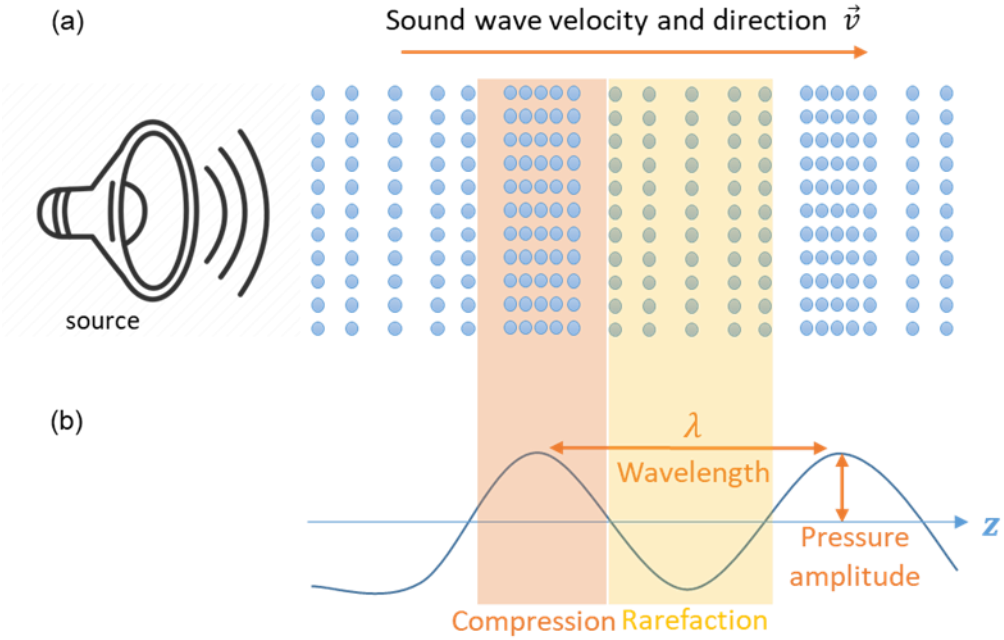

Figure 1. Propagation of longitudinal wave illustration. (a) One dimensional sound wave propagates by compression and rarefaction of particles in the medium. (b) Pressure graph produced by the sound wave in (a), displayed as a transverse wave.

The wave propagation phenomenon is commonly described by the wave equation. For simplicity, the second-order differential wave equation will be described for **a homogeneous** medium without attenuation, at a position (x, y, z) of the propagating space and at a time t [22]:

$$\nabla^2 p - \frac{1}{c^2}\frac{\partial^2 p(x,y,z,t)}{\partial t^2} = 0, \quad \nabla^2 p = \frac{\partial^2}{\partial x^2}p + \frac{\partial^2}{\partial y^2}p + \frac{\partial^2}{\partial z^2}p\,, \tag{2}$$

where ∇^2 is the Laplacian operator and c is the speed of sound in the medium:

$$c = \frac{1}{\sqrt{\kappa\rho}}, \tag{3}$$

where ρ is the medium density and $\kappa[Pa^{-1}]$ is its compressibility. The average speed of sound in the human body is 1540 m/s. It is the slowest in air/gasses and the fastest in solids. Here, the wave propagation description will refer to a plane-wave (PW), which propagates in x (positive) direction only:

$$\frac{\partial^2 p(x,t)}{\partial x^2} - \frac{1}{c^2}\frac{\partial^2 p(x,t)}{\partial t^2} = 0, \tag{4}$$

where $p(x,t)$ represents the pressure that is a function of the position *x* and time *t*. A possible general solution of (4) can be:

$$p(x,t) = p_0 e^{j(\omega t - kx)} \ , \tag{5}$$

where p_0 is the amplitude of the propagating wave, $\frac{\omega}{2\pi}$ is wave frequency, and $k = \frac{\omega}{c}$ is the wavenumber. In addition, it is common to represent the acoustic pressure by its magnitude, i.e., the real part of the expression in (5):

$$p(x,t) = p_0 \cos(\omega\left(t - \frac{x}{c}\right)). \tag{6}$$

Sound intensity *I*, for a PW, is defined as the power per unit area carried by a sound wave, and it is proportional to pressure amplitude oscillations [1]:

$$I = \frac{1}{T}\int_0^T p(t)\cdot v(t)dt \tag{7}$$

The relation between the generated pressure, *p*, and the particle velocity of the medium, *v*, is a specific acoustic property of the medium, known as the acoustic impedance *Z*, defined also by the product of the medium density and the speed of sound [23]:

$$Z = \frac{p(t)}{v(t)} = \rho c, \tag{8}$$

The impedance units are Rayls, 1[Rayl]=1[$\frac{kg}{m^2 \cdot sec}$]. By extracting particle velocity from (8) and substituting it with the pressure from (6) into (7), intensity can be described by:

$$I = \frac{{p_0}^2}{2Z} \left[\frac{W}{m^2}\right] \tag{9}$$

When a PW hits a boundary of another tissue/medium/object, the acoustic impedance changes and causes a portion of the incident wave energy to reflect and the rest continues to propagate further, but with some steering of the original wave direction because of the change in the speed of sound in the new medium, as illustrated in Figure 2. The angle of the reflected wave θ_r , is the same as for the incident wave θ_i (relative to the vertical of the boundary surface) but only backward. The angle of the transmitted wave θ_t in the new medium, can be calculated using Snell's low:

$$\frac{sin\theta_i}{sin\theta_t} = \frac{C_1}{C_2} \tag{10}$$

$$\theta_i = \theta_r$$

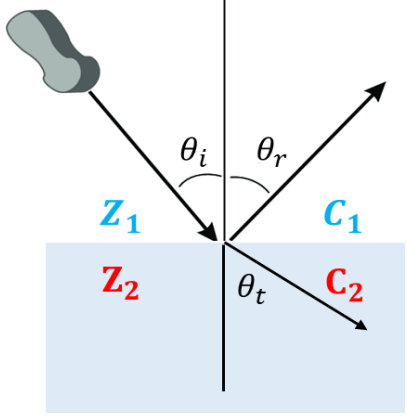

Figure 2. Ultrasound wave interactions. Reflection and refraction (transmission) of the incident wave in a medium with different acoustic impedance Z_2 and speed of sound C_2. C_1, Z_1 are the speed of sound and the acoustic impedance of the first medium respectively.

An important note to consider is that the reflection and refraction attenuate the original transmitted US beam, but without them, US echoes could not be generated.

Biological tissues are characterized by a strong absorption, which leads to a great energy loss of the transmitted beam. Therefore, the pressure wave representation in (5) must include also the attenuation component:

$$p(x,t) = p_0 e^{j(\omega t - kx)} \cdot e^{-\alpha x} \tag{11}$$

where α is an attenuation factor, dependent on wave frequency and medium viscosity and x is the wave penetration direction. As the frequency increases, so does the attenuation factor α. As a result, US imaging is limited by penetration depth, but if lower frequencies, we can increase the depth of penetration [1], as displayed in Figure 3:

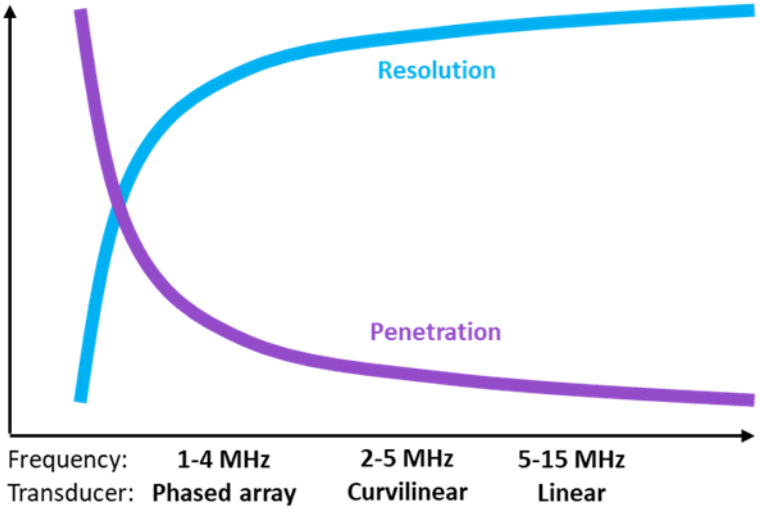

Figure 3. Resolution and penetration tradeoffs

3.3 Transducers

The simplest transducer is a piece of piezoelectric material, crystal such as lead-zirconate-titanate (PZT), with electrodes at both sides. When the transducer resonates (vibrates), it has a distinctive electrical impedance signature that can be measured electrically. By applying a potential difference across the electrodes, each piezoelectric material vibrates at its natural center-frequency and generates the ultrasonic signal [25]. This frequency specification is defined by the

transducer's frequency bandwidth (BW), which for diagnosis is mostly within the range of 1 MHz to 15 MHz. Most piezoelectric transducers are reciprocal, so they act as receivers equally well [1]. When receiving an echo, if the acoustical wave is within the range of the piezoelectric frequency BW, it will be detected and transferred to an electrical signal.

Early US imaging transducers used a single piezoelectric element, but they were not practical for the clinic, because they had to be mechanically scanned and they had a fixed focus that could not be changed. These two limited dramatically imaging depth, resolution, and real-time performance. Multi-elements arrays consist of many small piezoelectric elements (Figure 4), which are excited by phased-delayed signals to steer and focus beams electronically, at different depths and angles. This provides much more flexibility in controlling the delays and the waveform design of each element of the array, without moving any parts, which minimizes artifacts and scanning time. Moreover, arrays enable dynamic focusing (at the receive and transmit), changing the lateral resolution (lateral direction defined in Figure 4), and beam shaping, throughout apodization, which is applying weighting coefficients on the elements' excitation signals. Nowadays, the multi-element arrays became the standard transducers for US imaging systems in clinics and they include a large number of piezoelectric crystals, ranging between 64 to 512 [26].

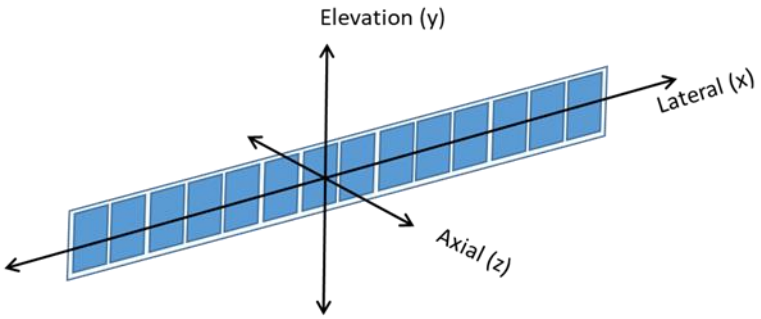

Figure 4. The spatial coordinate system for 1-D ultrasound transducer of the multi-elements array. The transmitted ultrasound wave propagates in the axial direction. The lateral direction is parallel to the surface of the elements.

In electronic focusing, all elements (or sometimes only a part of them) are excited with the same pulse at different times, such that the inner elements are delayed with respect to the outer elements. For example, (12) defines the delay time of each element in a linear array and a focal point position at (x_f, y_f, z_f), as defined in [23]:

$$\Delta t_i = \frac{1}{c}\left(\sqrt{(x_c - x_f)^2 + (y_c - y_f)^2 + (z_c - z_f)^2} - \sqrt{(x_i - x_f)^2 + (y_i - y_f)^2 + (z_i - z_f)^2}\right). \quad (12)$$

where (x_c, y_c, z_c) is the reference center point on the aperture (center of the transducer) and (x_i, y_i, z_i) is a center of a single piezo-electric element i. A focused beam results from the interference of the whole produced small wavelets, as illustrated in Figure 5. The time delays determine the depth of focus for the transmitted beam and can be changed during scanning.

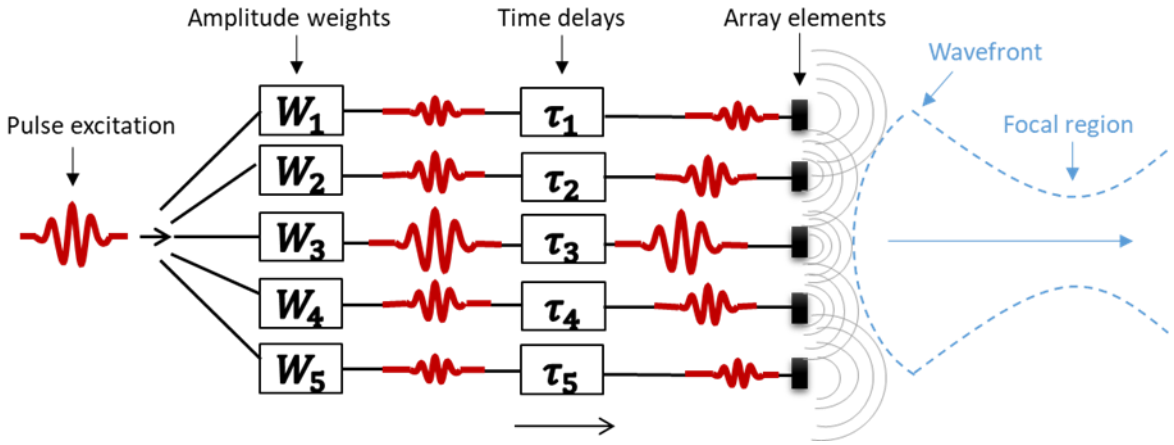

Figure 5. Electronic focusing with the multi-elements array at the transmit. Apodization and time delay are applied to each element's excitation pulse.

Depending on their clinical applications and scanning methods, US transducers appear in a wide variety of shapes, sizes, and frequencies. The three most conventional configurations are

linear, convex, and phased arrays. Figure 6 presents the three common types of arrays and their electronic steering for each case [27].

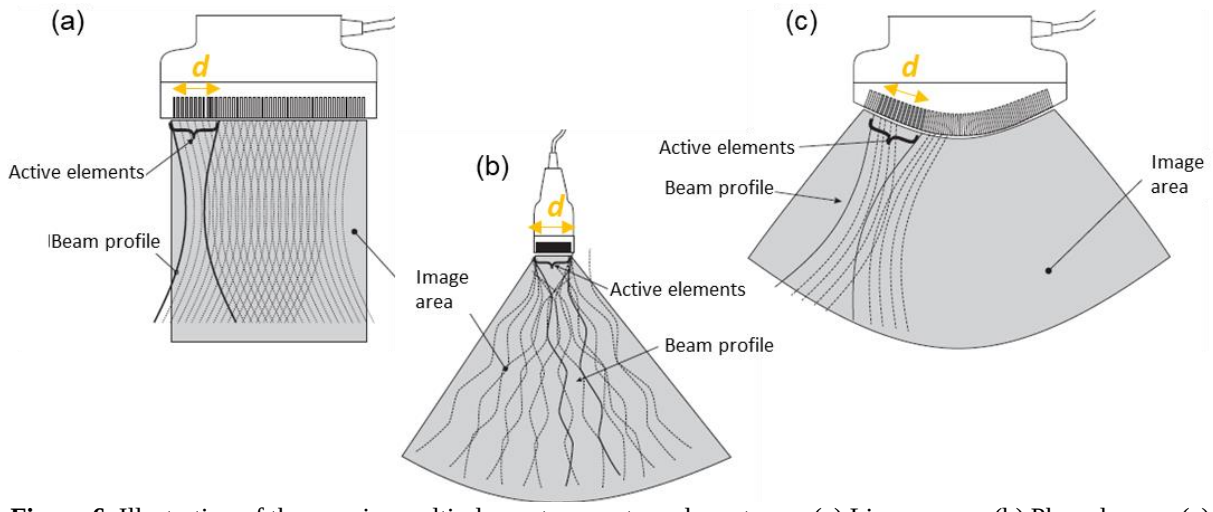

Figure 6. Illustration of three major multi-elements array transducer types: (a) Linear array, (b) Phased array, (c) Convex array, and their corresponded scanning modalities. *d* represents aperture width determined by the number of active elements.

3.4 B-mode and scanning

The most frequently used US imaging mode is the B-mode that uses the brightness of an imaging pixel to represent the strength of the echo from the corresponding voxel (imaging volume) inside the imaged tissue, where the sound wave scatters due to in-homogeneities of the speed of sound and density within it [19].

In standard US imaging, a typical B-mode image is reconstructed by multiple scan lines (64 to 512). Each scan-line is obtained by transmitting a focused pulse into the tissue, and then the transducer detects all generated echoes by reflections and scattering from the tissue. Typically, scanning with a linear array (Figure 6. (a)) is performed with a different part of activated elements of the array, in each scan-line. This sub-aperture contains 8-16 elements and is shifted over a region of interest in the body. I.e., the active elements are moved stepwise to the side, and a new

focused pulse is emitted and echoes received until all elements have been used. The shape of the field of view (FOV) and the resulting images is rectangular. Such transducers are usually used for imaging shallow objects because of the limited depth penetration due to their high frequencies relative to a phased transducer (Figure 6. (b)). When scanning with convex or phased array transducers, the FOV is enlarged by its fan shape, created by beam steering in different angles. Scanning with a convex array is the same as for a linear array, using sub-aperture and shifting the active elements in the array but with a larger area. However, when scanning with a phased array, all elements are activated in transmission and reception. Moreover, phased arrays permit reducing the number of elements of the transducer, which means a smaller array size, while obtaining a large FOV. The advantage of a small transducer is that it can reach "hard to get" regions for imaging e.g., the heart between ribs [28].

In general, each scanning configuration sets limits to the temporal resolution as the frame rate of a full B-mode image is limited by the number of scan-lines *N*, the speed of sound in tissue *c*, and scan depth Z_{max}, as described below:

$$f_R = \frac{1}{T_{frame}} = \frac{1}{t_{line} \cdot N} = \frac{1}{N \cdot \frac{2 \cdot Z_{max}}{c}} \tag{13}$$

But if decreasing scan lines, each scan line becomes wider (more active elements) to cover the entire scanned region, leading to a wider beam, and that decreases the spatial resolution. I.e., image resolution and frame rate compete with each other.

3.5 Image formation and quality metrics

After discussing the main concepts of US transmit and scanning, here is described image formation from the received echoes. When the scanning process is complete, all echo-response signals, received by the transducer's elements, are converted to radiofrequency (RF) raw data.

Then, the raw data go through beamforming (BF), which is the main stage in image formation. BF determines the resulted pulse-echo beam shape, which is the product of the transmit and the receive beams. The main two roles of BF are:

1. Steering or focusing the receive beam towards the coming signal from a known direction, usually from the focal point.
2. Improving the spatial resolution, the signal-to-noise ratio, and image contrast.

BF can be considered as a spatial filter. It enables the selectivity of acoustic signals, reflected from some known positions while attenuating the signals from other positions. This is classically done by delaying (focusing) and applying some specific weights (apodization) to the reflected signals and summing them to one RF signal, also known as DAS (delay and sum) [28]. This concept is illustrated in Figure 7 and displayed in Figure 8. BF process repeated for each scan-line.

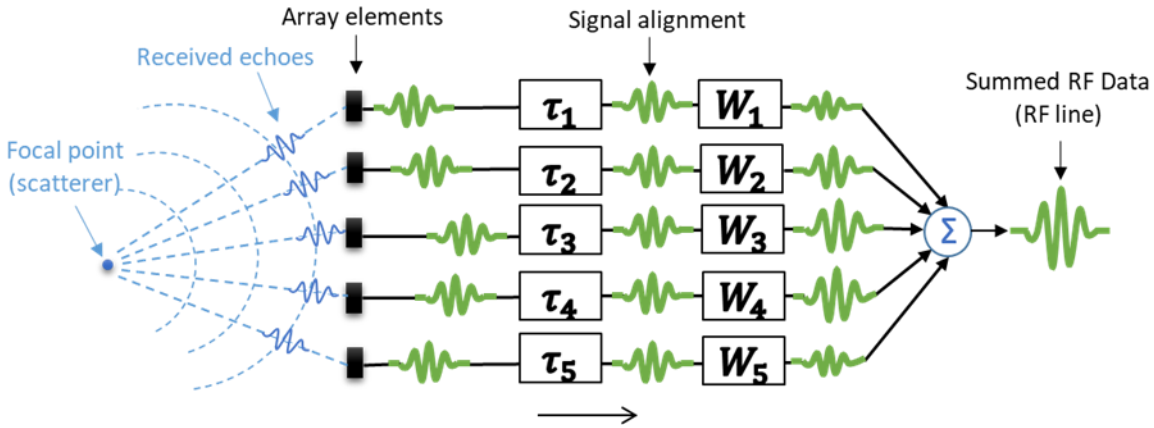

Figure 7. Beamforming principle to produce raw RF data, using 5 element-array. DAS technique includes a summation of the received echoes followed by time alignment and weighting according to the spatial position of the focal point.

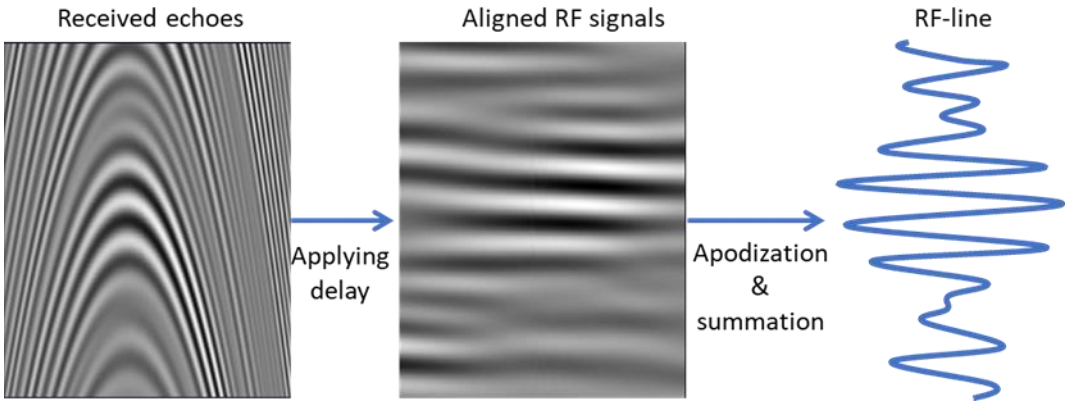

Figure 8. RF data generation with DAS. (a) Gray scale image of the received echoes detected by 64 elements for a single scan line. (b) Time alignment of (a). (c) The summation of all 64 signals forms the RF line.

BF process is applied also on the transmit beam and is the name of the overall process of designing the transmit waveform with a multi-array transducer. Mathematically, the RF-line can be expressed by:

$$RF(t) = \sum_{1}^{N} W_i y_i(t - \tau_i) \ , \qquad \tau_i = \frac{|\vec{r}_c - \vec{r}_f| - |\vec{r}_i - \vec{r}_f|}{c} \ , \tag{14}$$

where y_i represents the received echo detected by the i element, W_i and τ_i are the apodization coefficient and time delay applied on the received y_i echo, respectively. N is the total number of elements in the array. $\vec{r}_i$, $\vec{r}_c$, $\vec{r}_f$ are the coordination of the i element, the central element, and the element in front of the focal point in the array, respectively. c is the speed of sound in the medium. At the end of scanning, all obtained RF lines are juxtaposed to one matrix, called the RF image. However, it is still not a US B-mode image. The RF image needs to go through several processing steps until the final result (see a diagram example in Figure 9). These steps are usually as follows [29]:

- **Band/low-pass filtering –** to minimize noise and artifacts by frequency filtering according to different considerations, mainly dependent on the imaging technique.

- **Envelope detection** –provides the intensity magnitude of the RF signal, usually by applying the Hilbert transform on the RF image.
- **Gray scale mapping and logarithmic compression -**are techniques to determine the dynamic range of an image to optimize its smoothness and contrast performance.
- **Scan conversion-** transforming the collection of discreet pixels in a matrix to the final display of the B-mode image with the shape of the imaged region (see Figure 9. (e)).

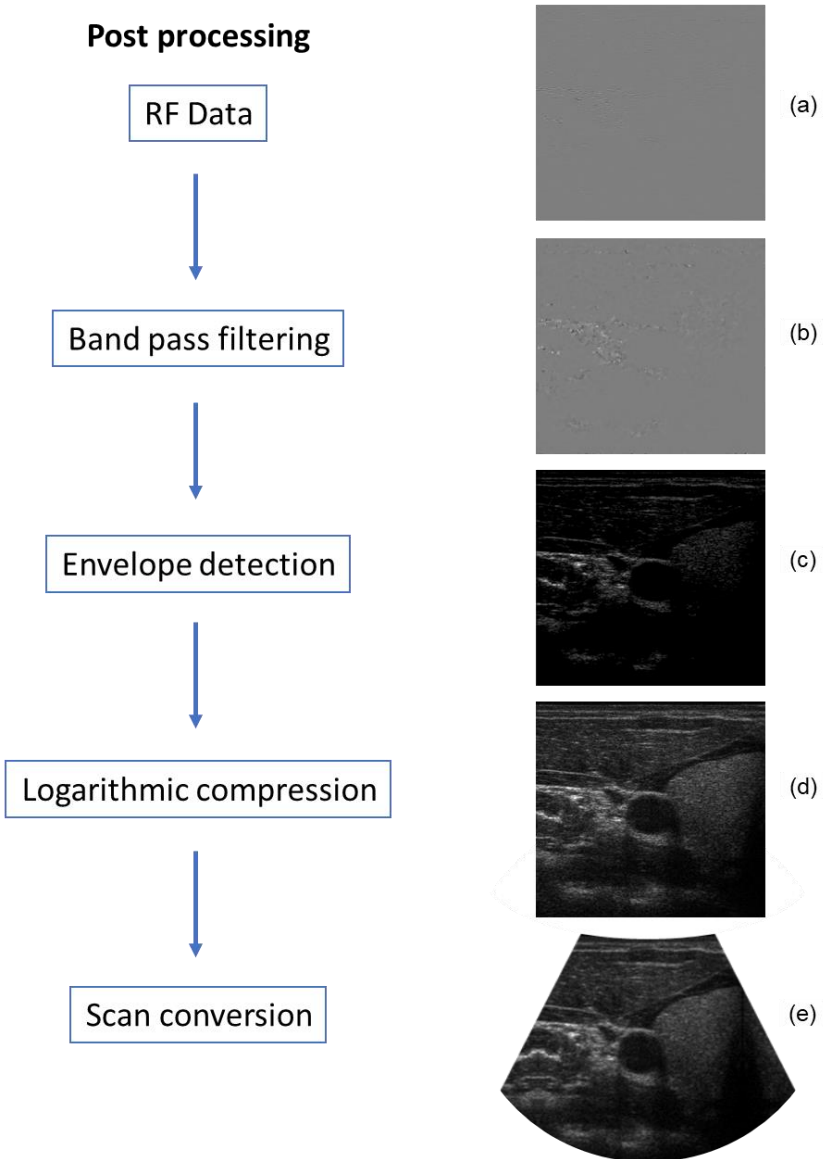

Figure 9. Diagram of typical post-processing steps applied on the RF image to obtain a B mode image. (a) the original RF image, (b) the RF image after band-pass filtering, (c) a gray scale image resulting after envelop detection with Hilbert transform, (d) a gray scale image after logarithmic compression, (e) a fan-shaped image after scan conversion.

To characterize a US imaging system, a variety of acoustical and electrical measurements must be taken to know its capabilities e.g., voltage range, frequency BW, the resulted pressure field, etc. In addition, imaging performance is evaluated by several standardized parameters and metrics. The most common are imaging resolution, contrast, noise level, and frame rate. The last was defined in (13) and the first three will be described below.

US image quality is strongly influenced by spatial resolution, both axial and lateral resolution. Figure. 4 illustrates the spatial coordinate system of the 1D US transducer.

Axial resolution- is the capability to distinguish between two objects lying in the direction of the US wave propagation [28] and it depends on the number of cycles, N_c, and the wavelength, λ, of the transmitted pulse :

$$\Delta z_{axial} \geq \frac{N_c \cdot \lambda}{2} \tag{15}$$

Lateral resolution- is the smallest distance between two objects lying in the lateral direction (perpendicular to wave propagation direction), that can be detected. I.e., if two scatterers are positioned at a smaller distance, they will be performed as one spot (object) in the B-mode image. This resolution is determined by the diffraction limitation, due to the beam width (at the transmit and receive), also known as the full-width-half-max (FWHM). For plane-wave imaging (no focusing at the transmit), with a rectangular aperture, as performed at this study, the FWHM parameter is defined as [2]:

$$\Delta x_{lateral} = FWHM \geq 1.206 \cdot \frac{\lambda \cdot z}{d} \tag{16}$$

d is the aperture width as demonstrated in Figure 4.

To describe US imaging visualization performance, there are common metrics to evaluate image quality. In this study, we focused on improving the contrast between a "cyst" with MBs

and the surrounding tissue and therefore, evaluation of the resulting images, conducted via contrast ratio (CR), [28] that is used from 1985 [30] :

$$CR = \frac{\mu_i}{\mu_o} \quad , \quad CR[dB] = 20log_{10}(\frac{\mu_i}{\mu_o}). \tag{17}$$

μ_i is the mean intensity inside the object or the region of interest (ROI) whereas, μ_o is the mean intensity of the outside of that region. When imaging a cyst, CR is simply the average gray-scale brightness level in the cyst compared to its surround.

3.6 Plane-wave and coherent compounding

To increase the frame rate and decrease acquisition time, PW imaging can be a great solution. PW imaging uses all the elements in transmission/reception to construct a US image. Of course, this image has a lower resolution than the one obtained with a standard US imaging with focusing. However, the resolution of the image can be increased by coherent-compounding. Coherent compounding imaging is a promising BF technique to obtain high frame rate imaging, where scanning is performed without focusing, but with a few PW transmits at different angles [31]. At each transmit event, a US wave is transmitted from the whole transducer array for PW imaging, where the delay profile of the excitation, for the steering angle, θ, can be defined by [23] :

$$\Delta t = \frac{dsin\theta}{c}, \tag{19}$$

where d is the aperture width (the width of all active elements and the spaces between them), and c is the speed of sound in the relevant medium. Figure 10, illustrates a steered PW transmit with a 5-element array:

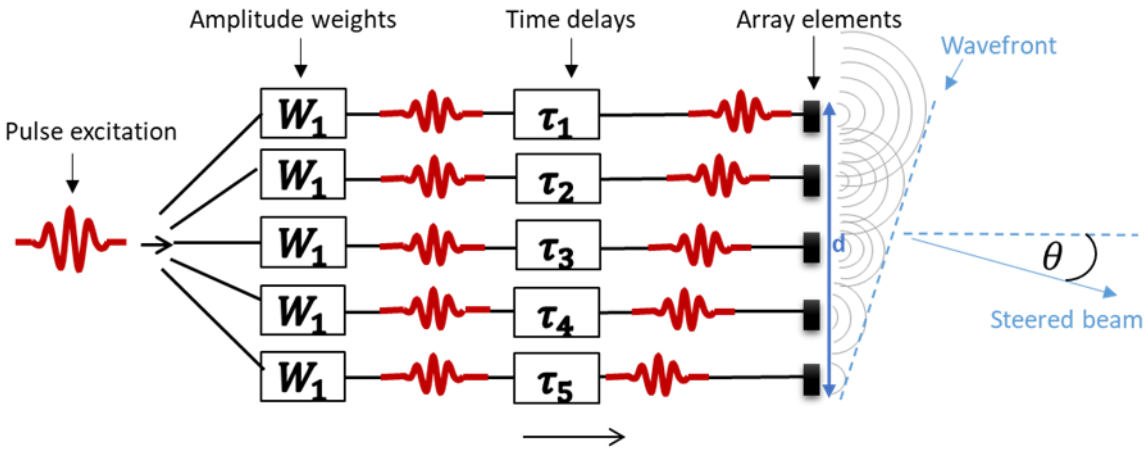

Figure 10. Transmit of Steered plane-wave at $\theta°$ angle. Specific delays applied on elements pulse excitation to obtain wavefront of $\theta°$.

The backscattered echoes are focused and then recorded using all elements on the receive aperture. The absence of a focus in the transmit, results in a low-resolution image (LRI) reconstruction. Then, this process is repeated for the desired number of steered PWs in different directions. Combining all resulted LRIs, by summing phase-aligned RF-signals, gives a high-resolution image (HRI) [32], (see illustration in Figure 11).

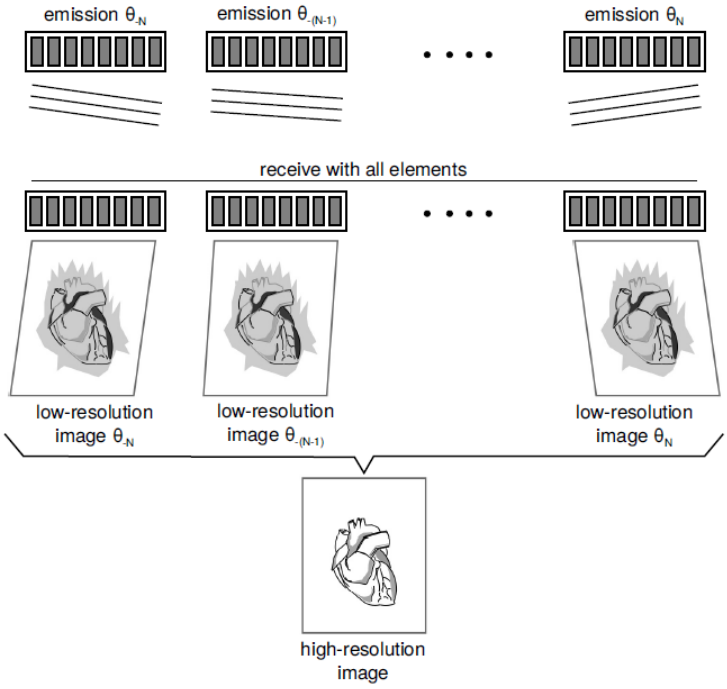

Figure 11. Coherent compounding beamforming principle. Transmitting N steered plane waves provides N low-resolution images. Then combination of their phase-aligned RF signals achieves a high-resolution image. Reprinted from Jensen, Jonas. "*Fast plane wave imaging*." Ph. D. dissertation (2017).

3.7 Safety in ultrasound imaging

Diagnostic imaging with the US is the safest imaging method. Therefore, it is not surprising that the last case of harm from the diagnostic US was reported in 1998 [33]. There are three main factors responsible for this impressive level of safety: First, is the large number of scientists studying ultrasound-induced bio-effects and different phenomena and processes under US radiation. Second, is the extensive knowledge of the two main bio-effects triggered by the US waves in tissue, cavitation, and thermal heating, and the ability to control and limit them with the acoustic output. Third, is the international standards of diagnostic US equipment that ensure safe imaging for humans and require measurements and characterization of the systems according to worldwide-accepted standards organizations, such as the American Institute of Ultrasound in Medicine (AIUM), the National Electronics Manufacturers Association (NEMA), etc. For example, the Food and Drug Administration (FDA) requires all US manufacturers that sell in the USA, to meet certain parameters and to measure acoustic output levels with a calibrated, broad-band hydrophone and report them the results on a regular basis [1]. However, there will always be unintended side effects as a result of the biophysics at the interaction of sound and tissue. Therefore, they came up with real-time algorithms for predicting relative temperature rises and potential for inertial cavitation, processes that can harm the tissue, and defined the thermal and mechanical indexes.

To assess the safety of the US and to predict the possibility for undesired mechanical bio-effects, mechanical-index (MI) was defined (20) and is commonly used. For imaging applications, the FDA limits the MI to be below 1.9 [34].

$$\mathrm{MI} = \frac{\mathrm{PNP}}{\sqrt{\mathrm{f}}}, \tag{20}$$

where the PNP is given in MPa and the frequency f is given in MHz. To evaluate the thermal effects in soft tissues, induced by the US during imaging, there is a thermal index for soft tissues (TIS), which is defined as the ratio of the transmitted acoustic power, (commonly set by the user during the scan), to the power required to raise the irradiated tissue temperature by $1°C$. TIS can be calculated using the following equation [33]:

$$\mathrm{TIS} = \frac{\mathrm{W}_0 \cdot f}{210\mathrm{mW} \cdot \mathrm{MHz}}, \tag{21}$$

where f [MHz] is the transmitted frequency and W_0 [mW] is the power applied, which depends on the transmit mode and beam's cross-section area at the most energetic depth. This unit-less index gives a rough estimate of the potential for temperature rise and its risk, from thermal causes, associated with the US beam. FDA has limited its maximal value for ophthalmology applications to $TIS \leq 1$ and for other applications $TIS \leq 6$ [24].

Any US imaging system in the clinic must measure and report in real-time these indexes, dependent on the settings of the device, imaging mode, and the transducer. A larger TI/MI value represents a higher heating/mechanical effect and potential for tissue damage.

3.8 Non-linear ultrasound imaging

In chapter 3.2, wave propagation in a tissue is assumed to be linear. However, like much of the real world around us, it does not always behave this way and in fact, the tissue has also nonlinear

characteristics. I.e., while propagating within the tissue, the wave's shape and amplitude are no longer proportional to the input excitation. Therefore, for a better understanding of propagation within a nonlinear medium, including the energy loss, there were developed and investigated many wave equations, which can be solved only numerically. One of them is known as the Westervelt equation- a full-wave, nonlinear equation that describes cumulative distortion, (based on conservation momentum) [35]:

$$\left(\nabla^2 - \frac{1}{c^2}\frac{\partial^2}{\partial t^2}\right)p = -\frac{\beta}{\rho c^4}\frac{\partial^2 p^2}{\partial t^2} \quad . \tag{22}$$

here, β is the coefficient of nonlinearity and it appears in the literature, papers, and characterization tables of tissues and mediums. For most tissues β falls in the range of 3 to 7 [1]. As a result, the general pressure solution in (5), has to be modified to a non-linear expression:

$$p(x,t) = [A \cdot p + B \cdot p^2] = p_0 e^{j(\omega t - kx)} + p_1 e^{2j(\omega t - kx)} \, , \tag{23}$$

where A and B represent constants, the first exponent in the expression is the linear solution and the second, the quadratic term, refers to the non-linear part and p_1 is its magnitude.

The major consequences of tissue non-linearity on the US wave, are pulse accumulation and beam distortion (Figure 12), which lead to harmonic frequencies generation. This phenomenon refers to the appearance of new frequency components in the wave's frequency spectrum, which contains not only the transmitted, fundamental frequency but also its integer multiples, called 'harmonic frequencies' (Figure 12. (b)). As the wave propagates, the distortion increases until the wave shape becomes a "sawtooth" (Figure 12. (c)), when it has the maximal harmonic frequencies [1]. And finally, at great distances and higher frequencies, the wave's distortion reaches saturation, where the whole wave signal is attenuated and is no longer proportional to the original emitted amplitude (Figure 12. (d)).

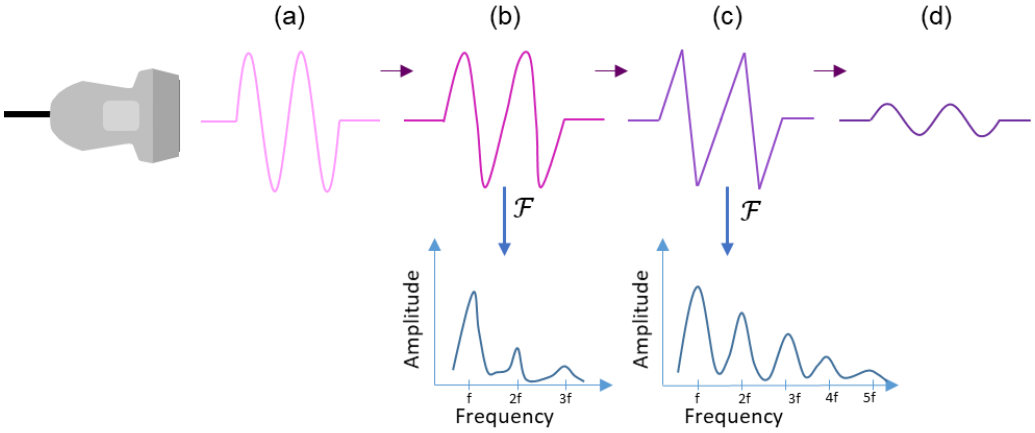

Figure 12. Harmonic frequency generation in a non-linear medium. (a) The transmitted sine wave of frequency *f*. (b) Initial wave distortion caused by asymmetric velocity of the two wave phases. (c) A wave "sawtooth" shape, rich with harmonics. (d) Attenuated sine wave followed by saturation of the non-linearity.

US imaging can be divided into linear and nonlinear imaging. Linear imaging occurs when the transducer captures only the backscattered echoes, that contain the same fundamental center frequency that was transmitted [1]. Nonlinear US imaging forms an image by detecting the additional frequency component observed in the returning echoes. These nonlinear components include harmonics, subharmonics, and ultra-harmonics [36]. The most commonly known nonlinear imaging methods are harmonic imaging (HI) and contrast harmonic imaging (CHI). The first is widely used for soft tissue imaging, whereas the latter is mainly used for vascular sonography with contrast agents [14], [37].

Although the nonlinear equation provides more accurate approximations to real waves propagation, it is more complicated for simulation use and design. Therefore, when designing the wavefront of the transmitted beam, where non-linearity was not necessary, simulations were performed with Field II, a MATLAB package, which is based on the linear equation only. Whereas, for the MBs simulations, where their nonlinear echo-response is responsible for the nonlinear US imaging technique we wanted to improve, the model had to include the nonlinearity term.

3.9 Harmonic imaging

One of the non-linear imaging modalities, that was introduced in the previous section is HI. This modality does not use UCA and is based on the harmonic frequencies generation in tissues, due to the US wave deformation while propagating through them. HI improves image quality even without UCA, compared to fundamental imaging [38] and is an important diagnostic tool in many clinical sonographic procedures and applications, such as the cardiac, abdomen, or fetal head imaging [11], tumors detection, and characterization [6], Doppler [10], and Elastography [12]. Advantages of HI include an increase in signal to noise ratio, contrast, and spatial resolution compared to standard linear imaging, as displayed in Figure 13:

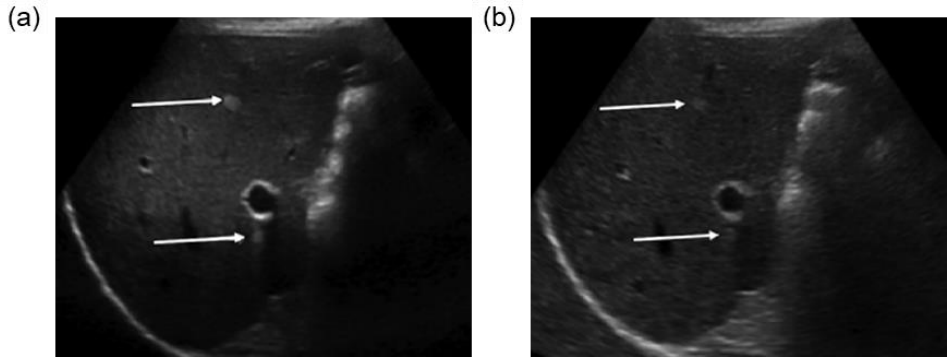

Figure 13. Images of two small hepatic abnormalities (arrows), were obtained by (a) harmonic imaging and (b) fundamental imaging. Reprinted from "*A primer on the physical principles of tissue harmonic imaging*,", Anvari et. al. (2015). Copyright *Radiographics*.

The most straightforward approach for HI is to bandpass filter the harmonic frequencies. However, this method is more effective when transmitting long pulses in order to narrow the spectrum and reduce spectral overlap. As a result, axial resolution is compromised, or additional post-processing is required [1]. This includes the use of a matching filter to restore axial resolution at the expense of reduced frame rate and increased complexity [17], [39]. Alternatively, pulse inversion (PI) is a method that uses two subsequent transmissions, where a

short pulse with positive polarity (+1) is initially sent, followed by an inverted pulse (-1) [40]. When the two waves propagate through a linear medium, such as water and liquids, the summation of their backscattered echoes cancels out. Whereas the waves propagate through a non-linear medium, such as elastic soft tissues, the summation of their backscattered echoes is retained and forms a high-frequency RF signal. I.e., this technique cancels the linear components, such that only the nonlinear components remain (illustrated in Figure 14). Other similar methods such as contrast pulse sequence [41], and power amplitude modulation [9] yield a similar overall result.

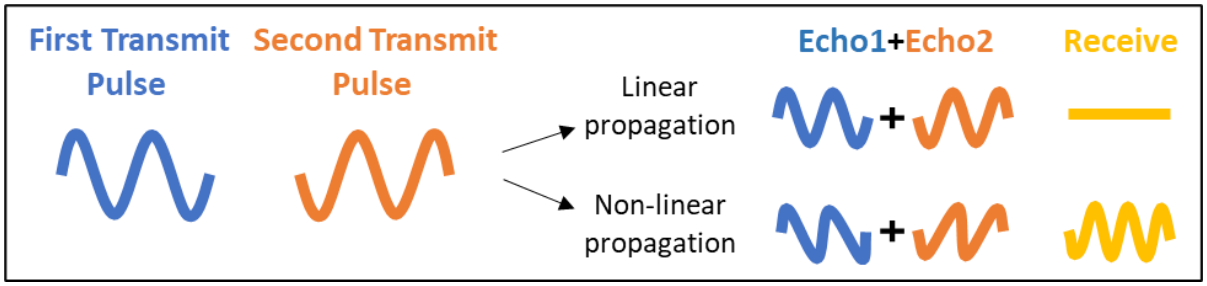

Figure 14. Pulse-inversion technique for harmonic imaging. Two phased inverted pulses (180° phase shift) are transmitted and their receive echoes are summed to an RF line. This technique removes the fundamental frequency from the entire image and remains only the non-linear, harmonic frequency components.

Although HI is used clinically, its main limitation is that the harmonic content is significantly weaker than the linear signal, and further attenuates as it propagates through the tissue. Therefore, nonlinear imaging methods are more sensitive to attenuation, noise, and artifacts [1].

3.10 Contrast harmonic imaging with UCA

Since the harmonic content is significantly weaker compared to the fundamental frequency, the standard HI method is not good enough in some cases, for example when imaging blood vessels that are almost invisible to the US without special processing. As a result, CHI, which uses UCA,

is also a commonly used nonlinear imaging technique in clinics, since it amplifies the harmonics and further enhances imaging [11], [42].

UCA are gas-filled MBs, usually with perfluorocarbon, encapsulated with phospholipid or albumin shells. The MBs are about 1-5 μm diameter, near the red blood cells size. They are injected into the vascular beds to reach the regions we want to image and to enhance their US reflections. After traveling in the blood system, they diffuse and are released through the lungs [1], [16]. Upon US excitation, a microbubble expands and contracts repeatedly, tracking the compressional and rarefaction cycles of the excitation sound wave [15]. As a result, their US scattering increases significantly. This, together with their impedance mismatch compared to the surrounding tissue, makes them highly echogenic [43], such that even a single microbubble can be detected in vivo [17].

All mentioned refers to MB's linear pulse-echo response, but the MBs have a non-linear characterization too. MBs act as nonlinear oscillators and oscillate asymmetrically, such that the expansion phase is larger than the compression. As a result, harmonics of the fundamental frequency are generated in the MBs echo spectrum, making them ideal contrast agents for CHI [44]. This phenomenon reminds the non-linearity within the soft tissues, but the harmonics generation in both cases are triggered by different mechanisms. While the tissue itself also possesses a nonlinear behavior at high pressures, MB's nonlinear response initiates at significantly lower pressures, and immediately under US excitation, where the tissue response remains mainly linear [40], [45], [46]. Moreover, MB's coefficient of nonlinearity, β, can be 10^3 times higher than for the soft tissues [46]. Since the nonlinear characteristics of MB are several orders of magnitude greater than tissue, a significant enhancement of MB's back-scattered signal is achieved, leading to a higher contrast relative to the surrounding tissue. In addition, this

phenomenon has a maximum at a specific frequency called resonance frequency. E.g., for a 4 μm bubble the resonance frequency is approximately 1.6 MHz [38].

In the fundamental, linear imaging, MBs demonstrate an increase in grey-scale values, which enhances the contrast between organs or regions with MBs to those without. For example, they can improve the endocardial border image of the heart ventricles or chambers, providing more accurate volume and movement analysis for the detection of abnormalities [38], as presented in Figure 15. Moreover, contrast agents significantly improve the ability and sensitivity of US to follow the flow of blood, especially in small vessels as in muscle perfusion. However, fundamental gray-scale imaging with MBs sometimes performs insufficient detectability in the presence of tissue, mostly in hyperechoic regions, where the fundamental backscattered component of the MBs is very low, relative to the component of the hyperechoic tissues. Therefore, CHI has a great advantage over HI and fundamental imaging, since it utilizes MB's non-linearity feature and separates their signal from the tissue by detection and filtration of the received harmonic frequencies from the entire echoes. This mode improves image performance dramatically and therefore, is widely used for different applications. The most common are: vasculature imaging, including artery stenosis [47], endocardial abnormalities [48], thrombosis [49], organ and cavities imaging [10], [50], tumors [51], and super-resolution US imaging [13], [52].

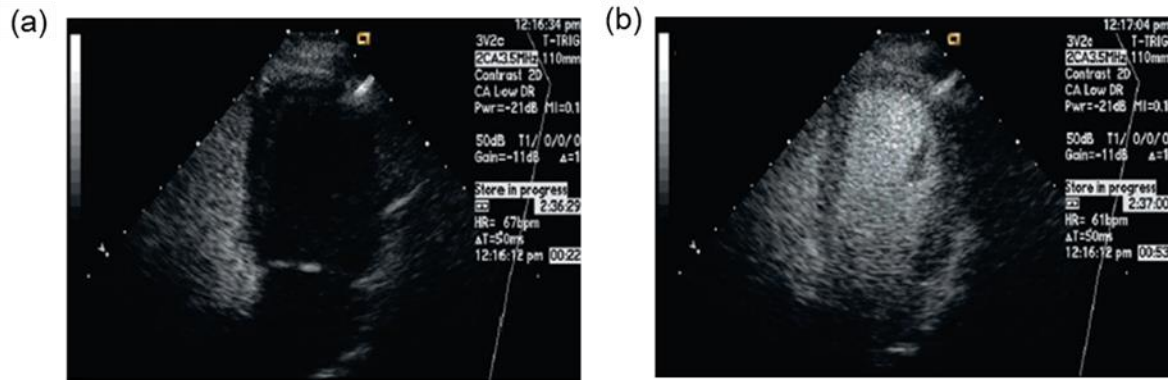

Figure 15. Ultrasound harmonic imaging of the left cardiac chambers. (a) Before microbubbles (MBs) entered and (b) after, where the ventricular myocardium border is well enhanced. Reprinted from "*Pulse inversion techniques in ultrasonic nonlinear imaging*,", Shen et al. (2005). Copyright *Medical Ultrasound*.

Despite all the benefits of CHI, there are still challenges, which limit the obtained image quality, especially under poor imaging conditions [14], [15]. E.g., when increasing the US pressure, the undesired nonlinear echoes from tissues also increase, reducing MBs signal [13]. Overall, there is a place for new advanced developments and research.

3.11 Simulating and modeling of UCA

The discovery of UCA and its unique echo properties have increased their use in diagnostic and therapeutic US applications. Therefore, there is a need for mathematical equations and models to characterize their motion and dynamics under different conditions, for further enhancements, research, and developments. There are several existing models, which provide nonlinear equations that can be solved numerically. They are all based on the gas-bubble oscillation theory, published by Lord Rayleigh in 1917 [53], but since then, there were many changes, improvements, and alternative models suggestions. The most familiar known as the Rayleigh-Plesset equation [1]:

$$\ddot{R}R + \frac{3\dot{R}^2}{2} = \frac{1}{\rho}(P_L - \frac{4\eta\dot{R}}{R} - P(t)). \tag{24}$$

where R=R(t) is the dynamic radius of the bubble to be found, P(t) is the varying acoustic pressure applied on the bubble, ρ is liquid density, η is the surrounding liquid viscosity, P_L is the pressure of the liquid near the bubble wall. However, the major shortcoming of this model is the absence of a bubble shell, which influences dramatically on its dynamics, because it modifies the effective surface tension. In addition, the shell increases the bubble's mechanical stiffness and elasticity, which stabilizes it and makes it difficult for it to shrink and expand. Therefore, for our simulations during this study, another model for bubble dynamics under US excitation was used. A model suggested by Philippe Marmottant et al. [54], takes into account the physical properties of MB's lipid shell and its non-linear behavior, triggered by large amplitude US waves. The model was validated by experimental recordings with a high-speed camera [54] and is widely used in ultrasound imaging [55] and therapy [56] research that uses MBs. Their main equation was based on dynamics are represented by its varying radius, due to its oscillation (expansion and contraction), triggered by the excitation signal. with polytropic gas law and with the following boundary condition, that describes the variable, dynamical surface tension as a function of the MB radius (R) :

$$P_g(t) - P_L(t) = \frac{2\sigma(R)}{R} + \frac{4\eta\dot{R}}{R} + \frac{4\kappa_s\dot{R}}{R^2}\ , \tag{25}$$

P_g is the gas pressure inside the bubble and is proportional to $R^{-3\kappa}$, where κ is the polytropic gas exponent. κ_s is the surface dilatational viscosity from the monolayer shell. $\frac{2\sigma(R)}{R}$ is the capillary pressure term, $\frac{4\eta\dot{R}}{R}$ is the stress arising from the frictions in the liquid and $\frac{4\kappa_s\dot{R}}{R^2}$ is the stress arising from frictions in the shell. The overall equation of the Marmottant model is:

$$\rho\left(\ddot{R}R + \frac{3\dot{R}^2}{2}\right) = \left[P_0 + \frac{2\sigma(R)}{R_0}\right]\left(\frac{R}{R_0}\right)^{-3\kappa}\left(1 - \frac{3\kappa}{c}\dot{R}\right) - P_0 - \frac{2\sigma(R)}{R} - \frac{4\eta\dot{R}}{R} - \frac{4\kappa_s\dot{R}}{R^2} - P(t) \tag{26}$$

R_0 is the equilibrium radius of the bubble and P_0 is the ambient pressure, and the tension expressed as :

$$\sigma(R) = \begin{cases} 0 & if\ R \le R_{buckling} \\ \chi\left(\frac{R^2}{R^2{}_{buckling}} - 1\right) & if\ \ R_{buckling} \le R \le R_{break-up} \\ \sigma_{water} & if\ R \ge R_{buckling} \end{cases} \quad (27)$$

This function includes three states of the bubble, also described in Figure 16. The first is the buckled state, when the bubble contracts too much, such that its lipid molecules at the interface decrease, leading to a decrease of the MB's surface tension, $\sigma = 0$. The second is the elastic state when the bubble's surface area is stable and even though it expands and contracts, this range of radius changes, is small and it maintains the same surface tension at the shell. The third is the ruptured state, $= \sigma_{water}$, when the ultrasonic pressure pulse leads the bubble to over-expansion and break-up, because of the developed stress and strain on the shell.

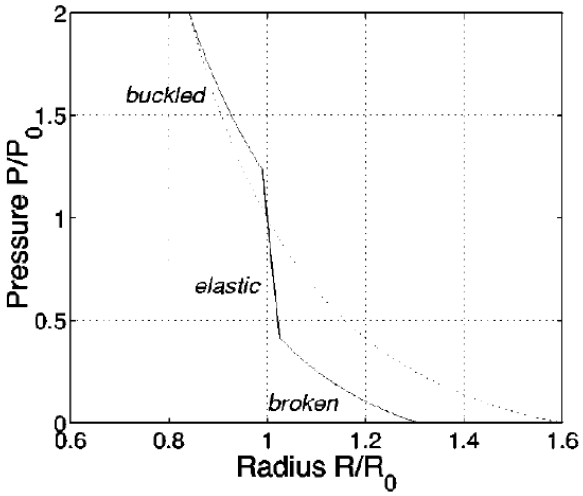

Figure 16. Three stages of bubble surface tension. Pressure rising ratio vs radius expansion ratio for an encapsulated bubble with shell. R_0 =2μm. $R_{buckling}$=1.98 μm, χ =1 N/m. Reprinted from "A model for large amplitude oscillations of coated bubbles accounting for buckling and rupture", Marmottant et al. (2005), Acoustical Society of America.

3.12 Frequency Mixing

When two or more acoustic waves interact, there is a generation of secondary waves having different frequencies from the fundamental, including harmonics, sum, and difference frequencies. This phenomenon was first reported by Peter Westervelt in his parametric acoustic array theory [57] and is usually known as the parametric effect, but in this work, we prefer to call it 'frequency mixing', inspired by optics [58] and electricity [59]. Westervelt's discovery has led to the development of new methods in various fields, based on the created difference frequency as a result of the interaction of the waves. Examples include the parametric array sonar [60], audio spotlight [61], characterization of liquid-vapor phase transition [62], nonlinear computed parameter tomography [63]–[65] and Vibro-acoustography [66]–[68]. Moreover, frequency mixing has been used to produce low-frequency waves in wideband scattering experiments [69]. In addition, it was found that the presence of a spherical scatterer, like an MB, enhances the frequency mixing effect due to two mechanisms, namely the dynamic radiation force and scattering of sound by sound [69]. Assume an MB in a fluid is notified simultaneously with two primary acoustic waves of an arbitrary wavefront, at two frequencies ω_1 and ω_2, with equal amplitude p_0 at the origin and they both propagated through the same distance x and attenuated at the same rate α. The resulted incident pressure can be described as [57]:

$$\begin{aligned} P(x,t) &= p_0 e^{-\alpha x}\left(e^{j(\omega_1 t - k_1 x)} + e^{j(\omega_2 t - k_2 x)}\right) = \\ &= p_0 e^{-\alpha x}(\cos(\omega_1 t - k_1 x) + \cos(\omega_2 t - k_2 x)) \end{aligned} \tag{28}$$

Then equation (26) can be modified to include this pressure term:

$$\rho\left(\ddot{R}R + \frac{3\dot{R}^2}{2}\right) = \left[P_0 + \frac{2\sigma(R)}{R_0}\right]\left(\frac{R}{R_0}\right)^{-3\kappa}\left(1 - \frac{3\kappa}{c}\dot{R}\right) - P_0 - \frac{2\sigma(R)}{R} - \frac{4\eta\dot{R}}{R} - \frac{4\kappa_s\dot{R}}{R^2} \tag{29}$$

$$-[p_0 e^{-\alpha x}(\cos(\omega_1 t - k_1 x) + \cos(\omega_2 t - k_2 x))] \ .$$

Using the successive approximation, a solution to this equation may be written as [16]:

$$\begin{aligned} R(t) = A_0 + A_1\, cos(\omega_1 t) + A_2\, cos(\omega_2 t) + A_3\, cos(2\omega_1 t) + A_4\, cos(2\omega_2 t) \\ + A_5\, cos((\omega_2 + \omega_1)t) + A_6\, cos((\omega_2 - \omega_1)t) + \cdots \ , \end{aligned} \tag{30}$$

where $A_i,\ i = 0,1,2,\ldots$ refers to the amplitude of the oscillating radius, corresponding to a specific frequency. Since the backscattered pressure signal is a result of the bubble oscillation, the receive echo-response contains the same frequency components and their approximated pressure magnitudes [16]. Moreover, the received spectrum contains both the difference frequency $(\omega_2 - \omega_1)$ and the sum frequency $(\omega_2 + \omega_1)$ components, in addition to the fundamental frequencies ω_1, ω_2 and their 2nd harmonics $2\omega_1$,$2\omega_2$ [9], [16], [70]. For simplicity, higher-order harmonics are not shown in (30).

For a better understanding of how the sum and difference components appear in the scattered echo, it is more convenient to substitute the expression for the incident wave with the two frequencies (28) in the general expression for the non-linear solution of the wave equation (23):

$$\begin{aligned} p(x,t) = A \cdot [\cos(\omega_1 t - k_1 x) + \cos(\omega_2 t - k_2 x)] \\ + B \cdot [\cos(\omega_1 t - k_1 x) + \cos(\omega_2 t - k_2 x)]^2 \ , \end{aligned} \tag{31}$$

where A and B are the pressure amplitudes of each component, including attenuation. For simplicity, we may ignore the spatial dimension (x) and expand the quadratic term:

$$\begin{aligned} p(x,t) = A \cdot [\cos(\omega_1 t) + \cos(\omega_2 t)] \\ + B \cdot [\cos^2(\omega_1 t) + 2\cos(\omega_1 t) \cdot \cos(\omega_2 t) + \cos^2(\omega_2 t)] \ . \end{aligned} \tag{32}$$

Using trigonometric identity for cosines multiplication, we get:

$$p(x,t) = A \cdot [\cos(\omega_1 t) + \cos(\omega_2 t)] \tag{33}$$

$$+B\cdot\left\{\cos^2(\omega_1 t)+\frac{1}{2}[\cos((\omega_1+\omega_2)t)+\cos((\omega_1-\omega_2)t)]+\cos^2(\omega_2 t)\right\},$$

which demonstrates how the new frequencies are created in the backscattered wave.

From all of the above, the non-linearity characteristic of the MBs can be expressed not only by harmonic generation in its backscattered signal but also by the frequency mixing effect. Nevertheless, it was reported that this effect is distinctly greater within MBs, rather than the surrounding tissues [15]. Therefore, these additional frequency components may provide a better MB separation and detection in tissues.

Frequency mixing was reported previously in the literature in the context of general tissue HI, without the use of MBs [17], [19], [39], [41]. In the most recent paper, three single element transducers were used for different frequency imaging: Two were used for transmit, where each transducer transmitted a different frequency (5 MHZ and 6 MHz). The two transmit transducers were mechanically aligned to focus on the sample. The third transducer was the receive transducer, with a center frequency that matched the difference frequency (1 MHz), to capture the frequency mixing result [19]. This setup (Figure 17) requires precise alignment of the three transducers, mechanical movement of the object to scan the entire FOV, and post-processing using a matched filter. Here, we aim to use a single phased array transducer for the transmit and the receive in real-time, without any moving parts or additional post-processing.

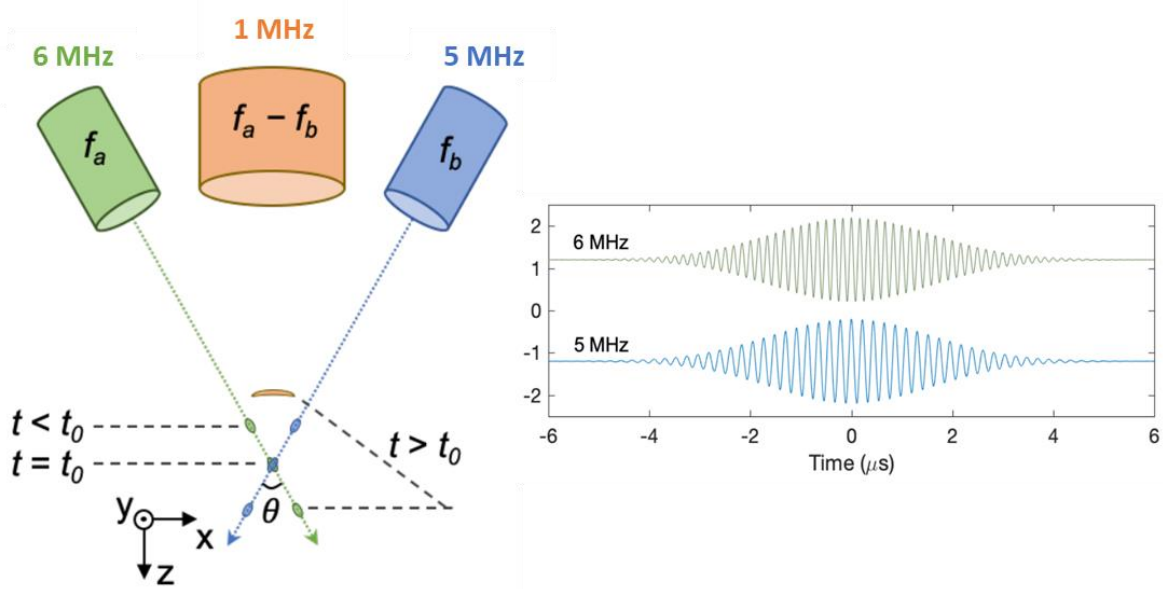

Figure 17. Setup for difference frequency imaging proposed by Li, Yilei, et al. (2019) *IEEE Transactions on Medical Imaging*.

Frequency mixing with MBs was also presented in several works [18], [20], [21], [71], [72]. However, the concept was demonstrated either only via numerical simulations [70], [72], by hydrophone measurements [15], [18], or by using single element transducers that capture the echoes at a single point [21], [71], [73] or via mechanical scanning of the object [19], [20]. All of the mentioned above methods, cannot be used for real-time imaging. Our method uses a single phased array imaging transducer for transmit and receive in real-time, without any moving parts or additional post-processing.

3.13 Proposed method concept

This study aimed to develop an enhanced and real-time contrast imaging of MBs based on the nonlinear mechanism of frequency mixing. The basic concept of the proposed method is to trigger the frequency mixing effect within MBs signal response, by exciting them with a dual-frequency waveform, that is a superposition of two different waveforms, each with a different frequency, in order to generate their sum and difference frequency components in addition to

their harmonics. The presence of additional nonlinear components, amplifies the MBs signal, leading to an increase in the resulting harmonic image quality and contrast. Figure 18 presents a schematic illustration of the proposed method. An additional major difference in our implementation, when compared to previous works and applications, such as in parametric arrays, is the absence of beams intersections applied by two simultaneous transmits from two transducers. This fact provides a larger image FOV, without the limitation of the intersection volume and eliminates the complexity of synchronization between the two pulses and the mechanical scanning. Thanks to advanced programmable US systems, this technique can be tested experimentally and not only in simulations.

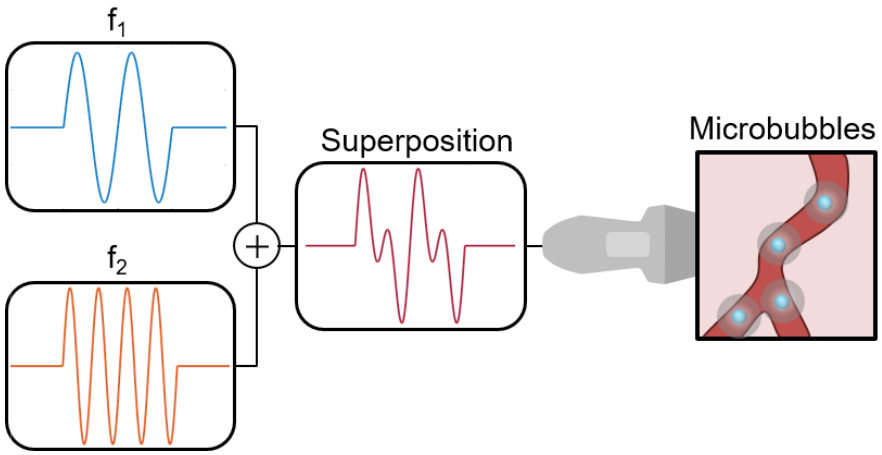

Figure 18. Schematic illustration of the proposed method. Two single frequencies are superpositioned into a multiplexed waveform. A broadband transducer is excited with this waveform for US imaging with MBs. Due to the frequency mixing effect, generated by the MBs, image quality is enhanced.

4 Materials and methods

4.1 Numerical simulations

Initially, acoustic pressure fields were simulated using Field II software [74], a MATLAB-based toolkit (version 2018a, MathWorks, Natick, MA, USA). This package provides acoustic wave propagation modeling, in various mediums and design different wavefronts with multi-element

arrays. Using this platform, we could explore the US imaging system setting and examine the effect of different transmit and receive parameters on the resulting fields. Afterward, we proceeded to other MATLAB simulations, based on the Marmottant and Rayleigh-Plesset equations, which describe MBs properties and their nonlinear behavior under US excitation in a fluid. Those simulations, provided an examination of MB's dynamics while taking into account parameters such as the effect of the surrounding medium compressibility, MB's shell composition, thickness and excitation parameters, etc. [54]. Predicting the MB's echo-response, assisted in designing optimal in-vitro experiments in the lab and minimizing risks and failures.

4.1.1 Filed II simulations

Field II is based on the concept of spatial impulse response as developed by Tupholme and Stepanishen for linear systems. Thus, only **linear propagation** of US waves can be simulated. This response gives the emitted US field, at a specific point in space, as a function of time, when the transducer is excited by a Dirac delta function. The field for any kind of excitation can then be found by just convolving the spatial impulse response with the excitation function:

$$p(\overrightarrow{r_1},t) = \rho_0 \frac{\partial v(t)}{\partial t} * h(\overrightarrow{r_1},t) \quad , \qquad h(\overrightarrow{r_1},t) = \iint \frac{\delta(t - \frac{|\overrightarrow{r_1} - \overrightarrow{r_2}|}{c})}{2\pi|\overrightarrow{r_1} - \overrightarrow{r_2}|} dS \tag{34}$$

where $|\overrightarrow{r_1} - \overrightarrow{r_2}|$ is the distance between the transducer and the field point, $v(t)$ is vibration velocity of transducer surface, proportional to applied electric voltage, $h(\overrightarrow{r_1},t)$ is the impulse response for $\overrightarrow{r_1}$ position and $p(\overrightarrow{r_1},t)$ is the resulted pressure at this point (a schematic system and its vectors are presented in Figure 19). To evaluate the total emitted pressure field, Field II sums all-spherical waves from each point on the aperture surface (transducer's elements array). It is important to note, that we did not include in these simulations the attenuation factor of the tissue.

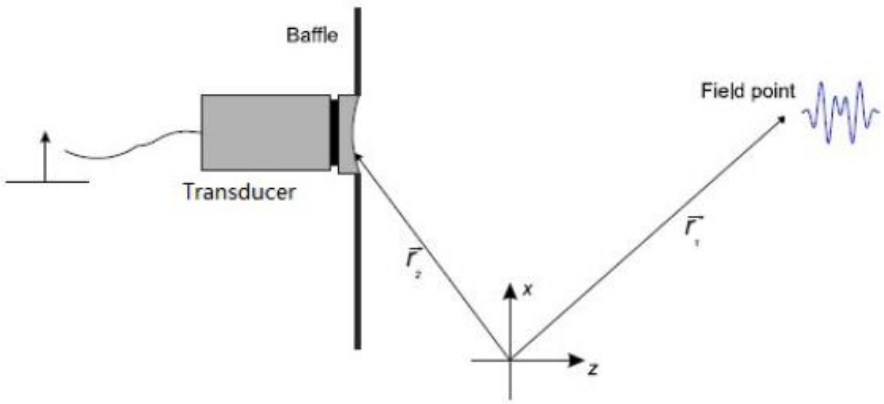

Figure 19. Transducer excitation and the obtained pressure field at a specific point in the XZ plane.

The main goal of this stage was to determine how we would create the dual-frequency transmit with a single transducer. What excitation should be applied on array elements and which waveform should be emitted? Initially, before we came to the idea of multiplexed (superposition) signal, we considered creating a cross-section between acoustic signals with different frequencies as was previously reported. Only instead of using several transducers, to use one, a broadband transducer, by dividing transducer's aperture into two synthetic sub-apertures, which transmit US waves with different frequencies.

The first configuration to manage that intersection was taken from a previously reported work [62] (in simulation only), where elements were divided into even and odd. Both groups were excited, such that their waves focused on the same point, as presented in Figure 20. Such a technique improves resolution and allows scanning, which expands the imaging region area. However, in each scan line, the region for beams intersection is very small, resulting in a low probability of the frequency-mixing effect to appear and thus, less enhancement of MBs echoes. Furthermore, this method produces grating lobes (duplication of the central lobe at the transmit field), which increase artifacts and noise in the image.

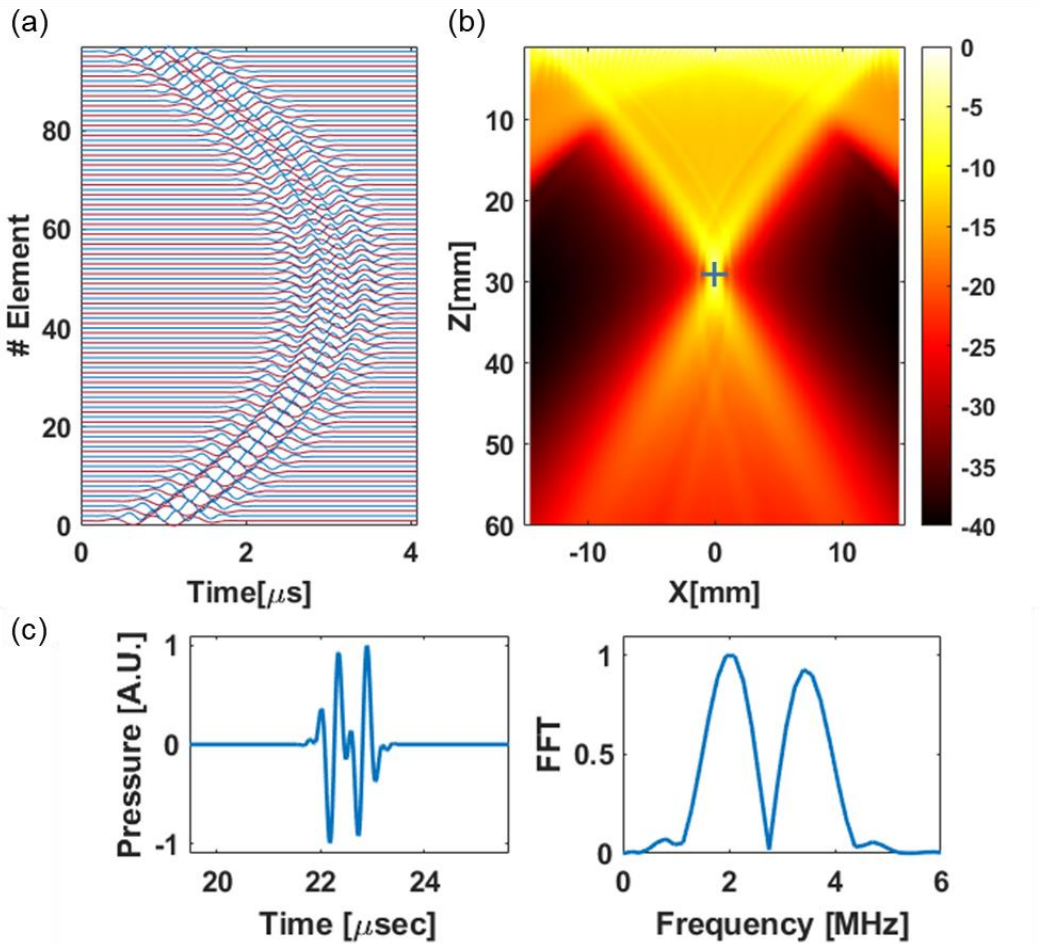

Figure 20. Field II simulation of dual-frequency transmits, by dividing aperture into even-odd elements, which excited with different frequencies 2 MHz (odd) and 3.5 MHz (even). (a)Excitation signals of 96 elements. (c)The sampled point at the focus, 30mm depth, in time and frequency domain, from the obtained transmitted field (b), displayed in 40dB scale

The second configuration is dividing the aperture into two halves, right and left, where each emits a steered PW towards the center, creating a rhombus-shaped overlapping area, as displayed in Figure 21. This region determines the imaging region, where the backscattered echo will contain the additional non-linear frequencies, due to the frequency mixing phenomenon.

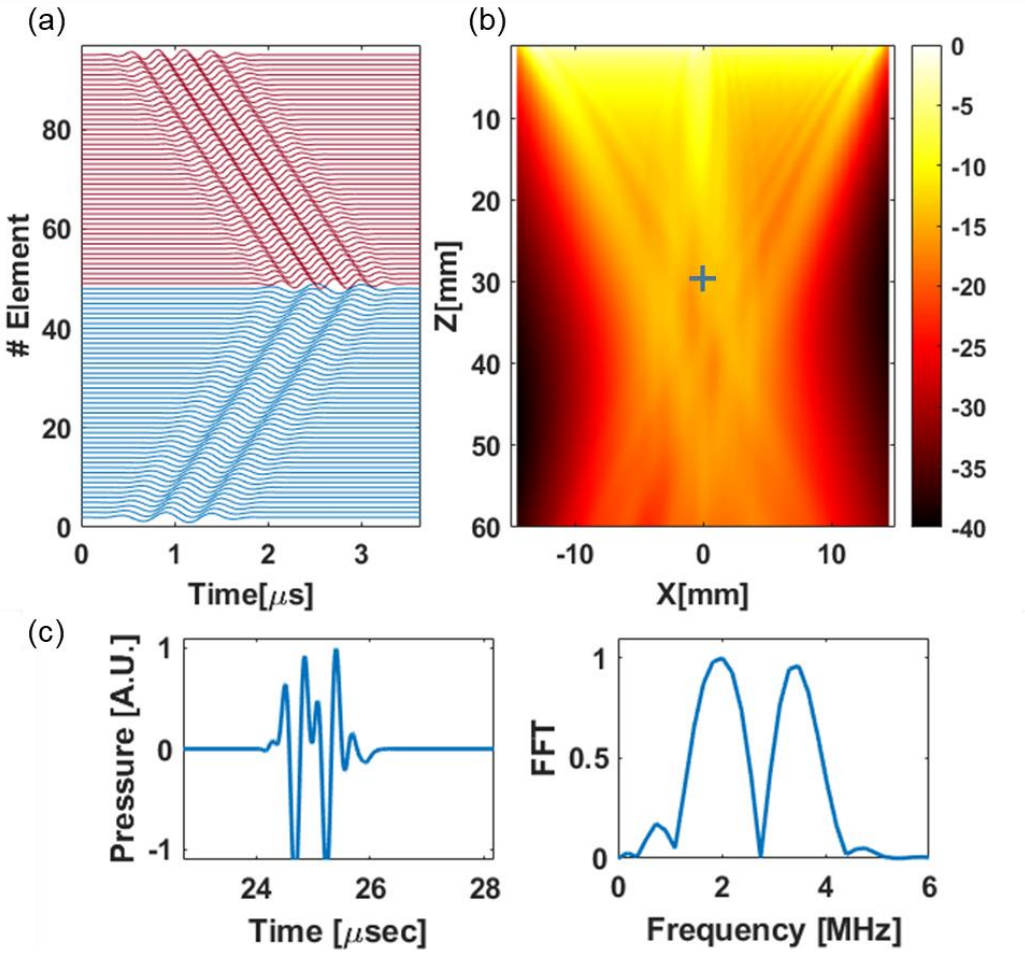

Figure 21. Field II simulation of dual-frequency transmits with X-Wave. Aperture is divided into two halves to transmit two intersectional plane waves with different frequencies: 2 MHz (left) and 3.5 MHz (right). (a)Excitation signals of 96 elements. (c)The sampled point at 30mm depth, in time and frequency domain, from the obtained transmitted field (b), displayed on a 40dB scale.

An advantage of such an implementation is that the transmission of a PW without focusing saves image acquisition time, i.e. improves frame rate. Moreover, it provides a wider overlap area for the different frequencies to intersect, which increases the frequency mixing generation. However, such implementation has limited FOV, since the imaging is confined to the area where the beams intersect. In addition, the method generates near-field artifacts at the region close to the transducer. Further, when imaging with MBs, it requires setting them up to concentrate in the overlapping region, which is a challenging task. Therefore, this method was rejected too.

The main common disadvantage of the last two configurations is that they utilize only half of the transducer's aperture and power to produce the new frequencies. In other words, the split of the aperture automatically leads to a decrease in the non-linear intensity by a factor of two. After performing several simulations, we thought we might be able to produce the same frequency mixing effect by transmitting a wave that already contains the two frequencies and doesn't require the intersection of the two waves. By defining the excitation pulse as a superposition of two sines with different frequencies (Figure 22.), we could use a full system's power (of Verasonics hardware), instead of dividing the transducer array into two synthetic sub-

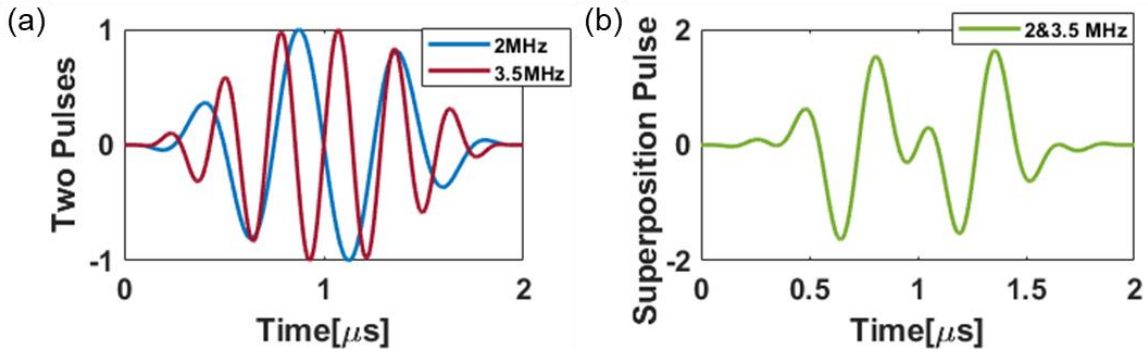

Figure 22. Excitation pulse in Field II. (a) 2 MHz and 3.5 MHz sines with the same time duration of $2\mu s$, followed by Tukey window and (b) their superposition, as were defined in ultrasound imaging experiments.

apertures.

Afterward, a focused transmit was simulated with the superposition signal, (Figure 23. (a),(b)). However, such a method still provided a limited FOV, where the MBs had to be placed. As a result, it was decided to transmit the superposition excitation with a few steered PWs (i.e., image would be formed with coherent compounding), see Figure 23. (c),(d). Without the focusing requirement, MBs backscattered signals can be enhanced in a wider region (FOV), and scanning becomes much faster, which are very precious conditions for real-time imaging.

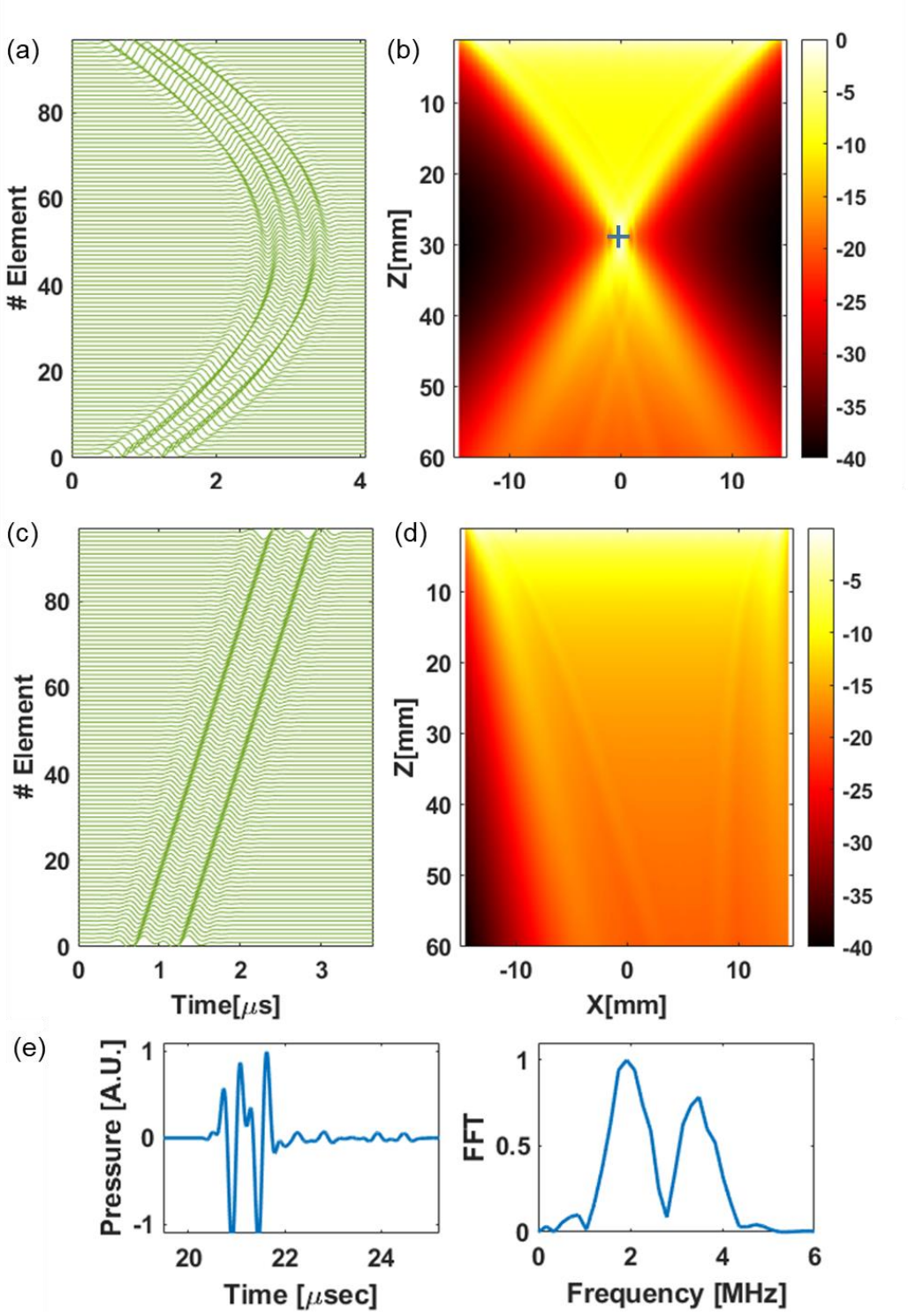

Figure 23. Field II simulation of dual frequency transmit with a superposition signal containing 2 MHz and 3.5 MHz frequencies. Two transmit fields were simulated: (b) focused and (d) steering plane-wave, displayed in 40dB scale. (a) and (c) are their corresponded excitation signals for 96 elements-array, respectively. (e)Sampled point from the focused transmit (b), at the focus, in time and frequency domain.

4.1.2 Microbubble echo-response simulation

MBs response to dual-frequency excitation was simulated via the Marmottant model, based on (26) and (27), to examine the non-linear phenomenon of harmonic and frequency mixing generation. MB's dynamics are represented by its varying radius, due to its oscillation (expansion and contraction), triggered by the excitation signal. MB parameters were identical to [54]; Shell surface dilatational viscosity was 7.2×10^{-9} N, elastic compression modulus was 0.55 N/m, the inner surface tension was 0.04 N/m, and the outer surface tension was determined as 0.073 N/m. MB's resting radius was set to 0.8×10^{-6} m, according to the physical dimensions of the MBs that were used in the experiments.

Three frequencies, f1, f2, f2 - f1, were chosen based on the transducer used in the laboratory experiments (P4-1, Philips, ATL, Andover, MA, USA), such that all fall within the transducer's BW (1-4 MHz). f1 was 2 MHz, f2 was 3.5 MHz and therefore the difference frequency is expected to be 1.5 MHz. It should be noted that, although the sum frequency is also generated, its frequency is beyond the cutoff frequency of the transducer (f2 + f1 = 5.5 MHz > 4 MHz). Therefore, our focus was on the difference frequency.

Each Marmottant simulation for PI imaging consisted of two transmits. One was the positive pulse and the second was a negative pulse, identical to the positive pulse but with a reversed polarity. Then, the simulated MB's responses were summed. As a result, the fundamental frequency was eliminated, leaving only the non-linear frequencies. Three excitation conditions were compared: 1) PI with a single frequency of f1 = 2 MHz; 2) PI with a single frequency of f2 = 3.5 MHz; 3) PI with a dual-frequency composed of a superposition of 2 and 3.5 MHz. Each excitation condition consisted of a sinusoid with the desired center frequency (or the superposition), enveloped by a Tukey window, as commonly used in the US [14], [44], [75]. For

initial validation of the method, in the simulation stage, all excitations were 10-cycle pulses, whereas, for the superposition signal, we did an alignment by the lower frequency, i.e., 2MHz. The purpose of transmitting multi-cycle pulses is a good visualization of the frequency components in the signal's spectrum (the longer the pulse is, the narrower are the spectral components). In addition, bandpass filtering between 1-4 MHz was applied to the final results to mimic the BW of the transducer used in the experiments. Spectral representation of the excitation and received signals ware performed by applying a Fourier transform to the temporal signals.

4.2 Ultrasound imaging

This stage includes designing the setup and programming the US system to perform the desired imaging protocol, considering the chosen US transducer and excitation parameters. Experiments were conducted using a programmable research US system (Vantage 256, Verasonics, Kirkland, WA, USA) with a phased array P4-1 transducer (Figure 24). The transducer had 96 elements, with a 0.295 mm pitch. All transmitted waveforms were generated and transmitted by an arbitrary waveform generator (AWG), which enables transmit of custom waveforms.

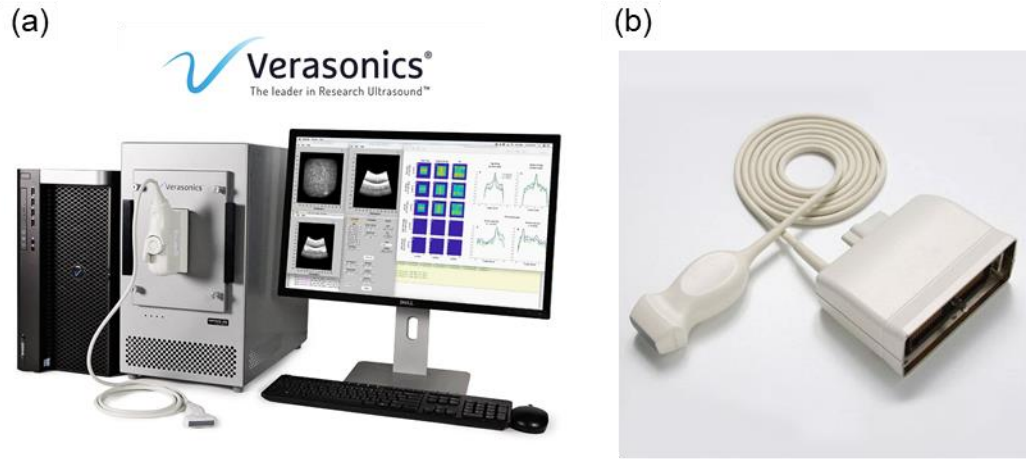

Figure 24. Hardware used in ultrasound experiments: (a) Verasonics programmable research ultrasound system and (b) P4-1 phased array.

PI US imaging protocol was used to image the tissue-mimicking phantom including coherent compounding, using 9 angled PWs spanning ±10^{o}, as was presented in [31]. The transducer was fixed to an optical plate and positioned perpendicularly to a tissue-mimicking phantom that contained a 6 mm inclusion located at a distance of z = 45 mm from the transducer (see Figure 27). In each acquisition, a solution of $1.67x10^{6}$ MBs was diluted in 0.5 ml phosphate-buffered saline and then was injected into the inclusion inside the phantom. For spectrum assessment experiments, waveforms included also a 10-cycle sinusoid, either at 2 MHz, 3.5 MHz, or 2&3.5 MHz with a Tukey window. Next, both transmit and receive were conducted by the P4-1 transducer, while imaging the tissue-mimicking phantom. The received radio frequency signals captured by each element were averaged and Fourier transform was applied to the result to display the spectra in real-time by the programmable US system. The process was repeated both for a single PW and a PI transmit for each of the three waveforms.

For imaging applications, a 1-cycle sinusoid was transmitted (2-cycle waveform with a Tukey window to yield an effective 1-cycle). This excitation was used to maximize axial resolution and eliminate the need for additional post-processing. In the imaging section, the generation of the frequency mixing component translated into contrast enhancement. Therefore, instead of looking at the frequency components, as done in the numerical simulations and hydrophone measurements, the contrast was calculated. Since the 2nd harmonic of the 3.5 MHz frequency is 7 MHz, which is beyond the cut-off frequency of the transducer, imaging results were compared for PI with a single frequency of 2 MHz, and a dual-frequency of 2&3.5 MHz. To compare the different frequencies, images were acquired with the same mechanical index (MI) which was calculated by (20). The MI increases as the frequency decrease therefore, for the

dual-frequency excitation, we chose to use the lower frequency (2 MHz) in the MI calculation, as a stricter upper limit.

In a programmable US system, like the one in our lab, the center-frequency of the receive and the transmit signals are not dependent and can be set to different values. Therefore, in addition to the two PI transmits (2 MHz and 2&3.5 MHz), three different central-frequency for the receive, $f_{receive}$, were examined in US imaging experiments: 1.5 MHz, 2.5 MHz, and a custom frequency. The first was set to be around the difference frequency we expect to receive from the frequency-mixing method, and at the second experiment, it was set to the default central-frequency value of our transducer. The third experiment, with the custom frequency, $f_{receive}$ was set to a specific match according to the transmit method. That is, for the dual-frequency transmit, $f_{receive}$ =1.5 MHz, to detect the difference frequency and for the 2 MHz transmit, $f_{receive}$ =3.5 MHz, to be close enough to detect its 2nd harmonic (4 MHz), but not at the end of transducer BW.

In each experiment, the MBs inclusion was imaged with each method. The phantom was washed between successive acquisitions and a fresh MBs suspension was injected into the inclusion. Additional US imaging experiments were performed to test the versatility of the proposed method and for further optimization. For example, the effect of the number of transmitted angles and MBs concentration were examined.

4.2.1 Microbubble's preparation

MBs used in this study were prepared as reported in [76] and composed of a phospholipid shell and a perfluorobutane (C_4F_{10}) gas core, as illustrated in Figure 25 (a).

Briefly, the lipids (2.5 mg per 1 mL) disteroylphosphatidylcholine (DSPC), and 1,2-distearoyl-sn-glycerol-3-phosphor-ethanolamine-N-[methoxy (polyethylene glycol)-2000] (ammonium salt) (DSPE-PEG2K) (Sigma Aldrich) were combined at a molar ratio of 90:10 and made using

a thin-film hydration method. A buffer (mixture of glycerol (10%), propylene glycol (10%), and saline (80%) (pH 7.4) were added to the lipids and sonicated at 62°C. The MBs precursor solution was aliquot into vials with a liquid volume of 1 mL and saturated with the gas. Upon use, the vials were brought to room temperature and shaken for 45 seconds in a vial shaker. MBs were purified via centrifugation to remove bubbles smaller than 0.5 μm in radii. Size selection via centrifugation was performed to remove MBs larger than 5 μm.

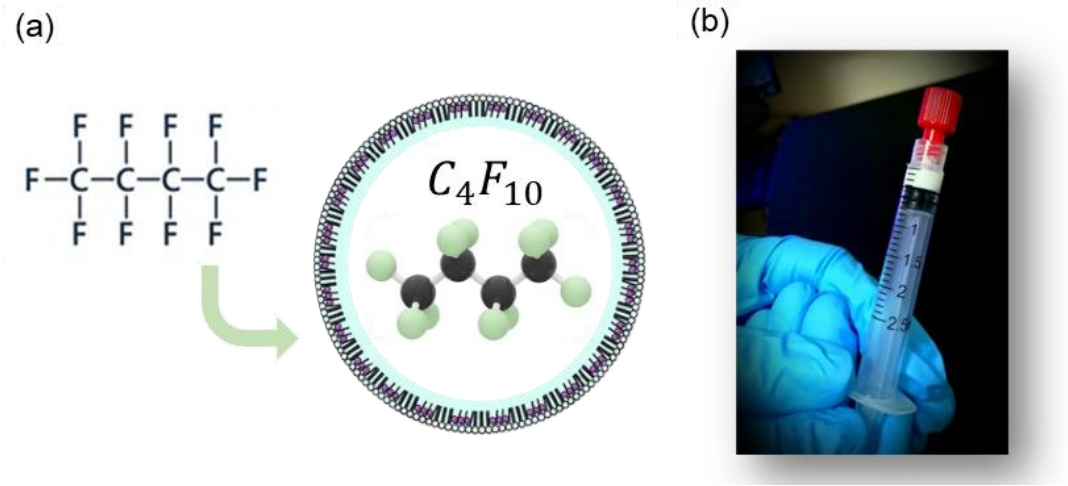

Figure 25. Microbubbles (MBs) as ultrasound contrast agents, composed of (a) phospholipid shell and a perfluorobutane (C_4F_{10}) gas core. (b) MBs (white foam) in a syringe, produced in our lab.

The size and concentration of the purified MBs (Figure 25. (b)), were measured with a particle counter system (AccuSizer® FX-Nano, Particle Sizing Systems, Entegris, MA, USA). MB's radius was ~0.8 μm and their concentration $\sim 1 \times 10^{10}$ MBs/ml. The MBs were used within three hours of their preparation.

4.2.2 Transducer calibration with a hydrophone

Verasonics US system provides control of the output power and voltage. However, for each hardware it might produce a different pressure output, mainly depending on the transducer's characterization, its frequency BW, number of elements, electrical amplifier, etc. To determine

the relationship between the measured pressure and the emitted electrical pulse, calibration was done with a wide-band needle hydrophone (NH0200, Precision Acoustics, Dorchester, UK), with an active aperture of 0.2 mm in a degassed water tank (Figure 26). The hydrophone probe was mounted on a three-dimensional positioning system (Newport motion controller ESP301, Newport 443 series). The received pressure signals for different power outputs were recorded with a digital oscilloscope (MDO3024, Tektronix, OR, USA), and further peak-negative pressure was extracted from each measurement to perform linear regression.

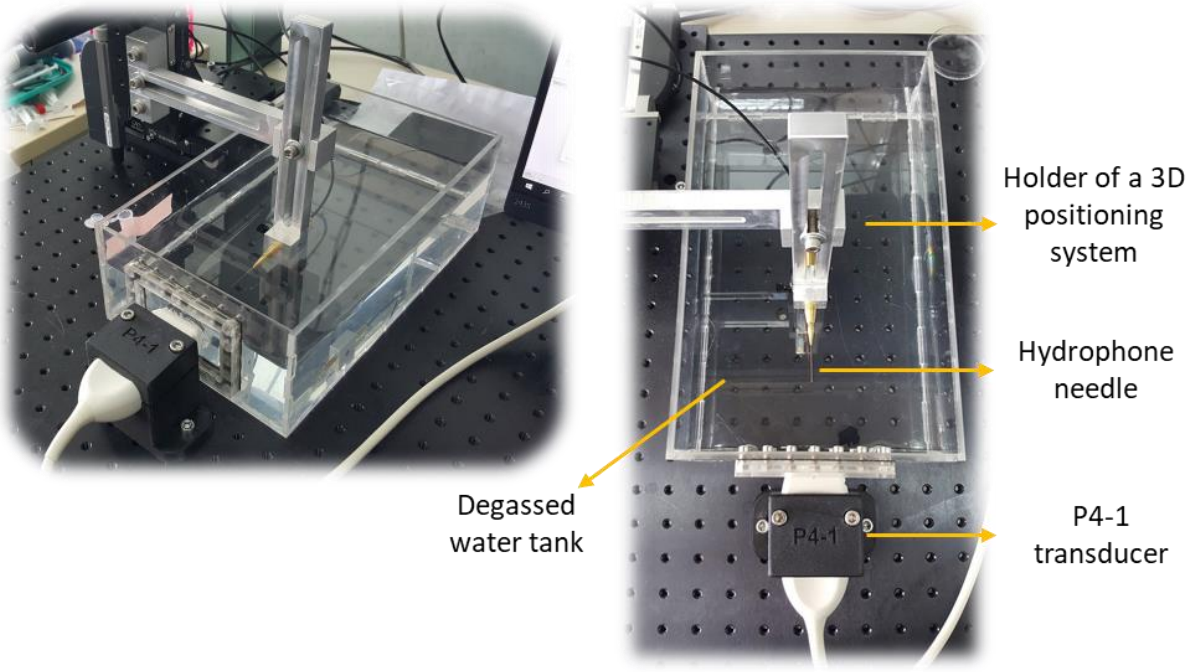

Figure 26. Pressure calibration of P4-1 transducer with a hydrophone inside a degassed water tank.

4.2.3 Tissue-mimicking phantom preparation

The phantom was prepared by mixing 1.5% agarose powder (A10752, Alfa Aesar, MA, USA) with deionized water at ambient temperature. Then, the solution was heated until all powder was completely dissolved. 1% silicon carbide (357391, Sigma Aldrich, MO, USA) was added to the solution and thoroughly mixed, to add acoustic scattering. The homogenous solution was poured

into a stainless steel $90 \times 60 \times 50$ mm^3 mold that contained a cylindrical 6 mm rod at its center and allowed to cool at ambient temperature (Figure 27. (b)).

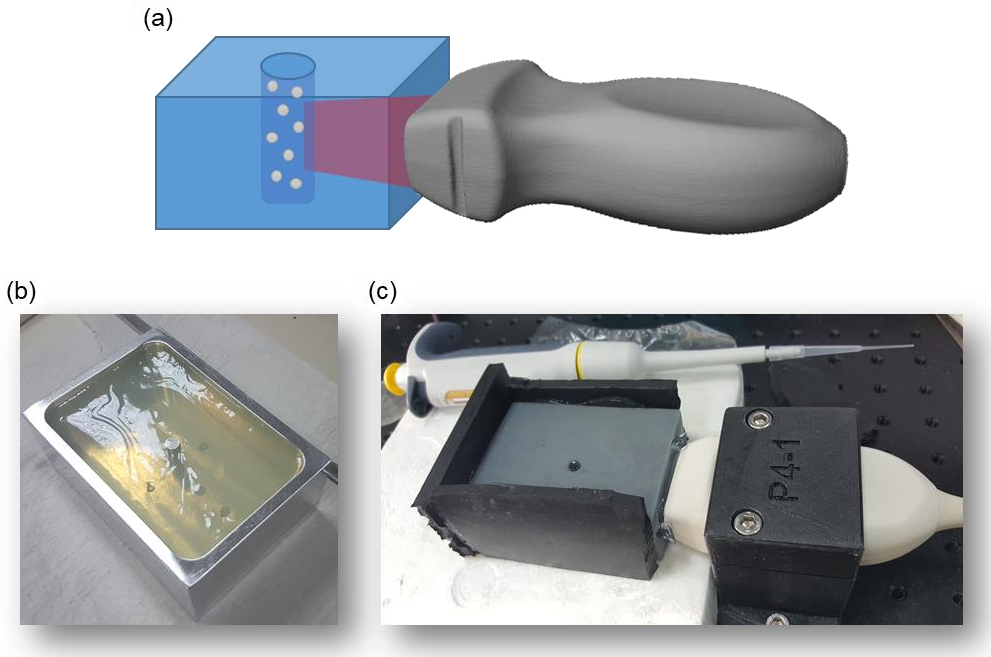

Figure 27. Tissue-mimicking phantom for ultrasound imaging experiments. (a) Setup illustration. A phased array transducer for imaging microbubbles (MBs) suspension injected into a rod inclusion in a tissue-mimicking phantom. (b) A 3D stainless steel mold with a cooling agar solution (without scatterers) with a cylindrical rod in the center, which produces its negative in the phantom. (c) Setup image. A tissue-mimicking phantom with SiC scatterers and a P4-1 phased array transducer controlled by a programmable ultrasound system. The pipettor aside is used to inject MBs suspension into the cylindrical cavity.

4.2.4 Contrast analysis

Imaging experiments were conducted for five different MI (0.04 to 0.18) and repeated 4 times for statistical analysis. Post-processing was used to calculate the inclusion contrast for each acquisition method, according to (17), whereas the contrast is calculated by the ratio between the average gray levels of MB inclusion ("cyst" region) and the surrounding background [77], [78]. To do so, the two regions were selected as marked with green and red circles in Figure 28, for all obtained US images in each experiment. Statistical analyses were performed using Prism9 software (GraphPad Software Inc.). Results are presented as mean ± STD. Statistical tests are

reported in the relevant captions. P values less than 0.05 were considered significant and were adjusted for multiple comparisons as indicated in the captions.

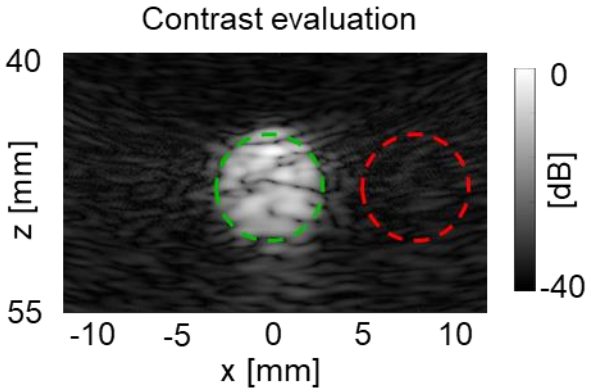

Figure 28. Selection of "Cyst" and "background" regions for US contrast image evaluations. The green circle marks a region inside the MBs inclusion, and the red circle marks a speckled background outside the inclusion.

4.2.5 Real-time display of received RF

As a part of PI protocol implementation, to ensure it performs as intended, a real-time display of the received RF signals and their frequency content was added to the conventional US imaging GUI. When imaging the MBs (inside the tissue-mimicking phantom), it allows seeing if the harmonic generation and frequency mixing appears and if the summation of the received backscattered signals of the transmitted two phased-inverted pulses, cancels the linear components and remains only the non-linear. Figure 29 presents two examples of this GUI implementation, obtained during US imaging experiments with the MBs suspension inside a tissue-mimicking phantom. Subfigures (a),(b), and (c) refer to a dual-frequency transmit of 2&3.5 MHz, whereas (d),(e), and (f) refer to a conventional "single-frequency" transmit of 2 MHz. (a) and (d) display the received RF image for one transmitted PI sequence (two phased-inverted pulses). The RF images were constructed from 1024 samples (z-axis) from 96 channels (elements in x-axis), in grayscale, and performed two dense regions, which are the corresponding backscattered echoes detected by the transducer, before beamforming.

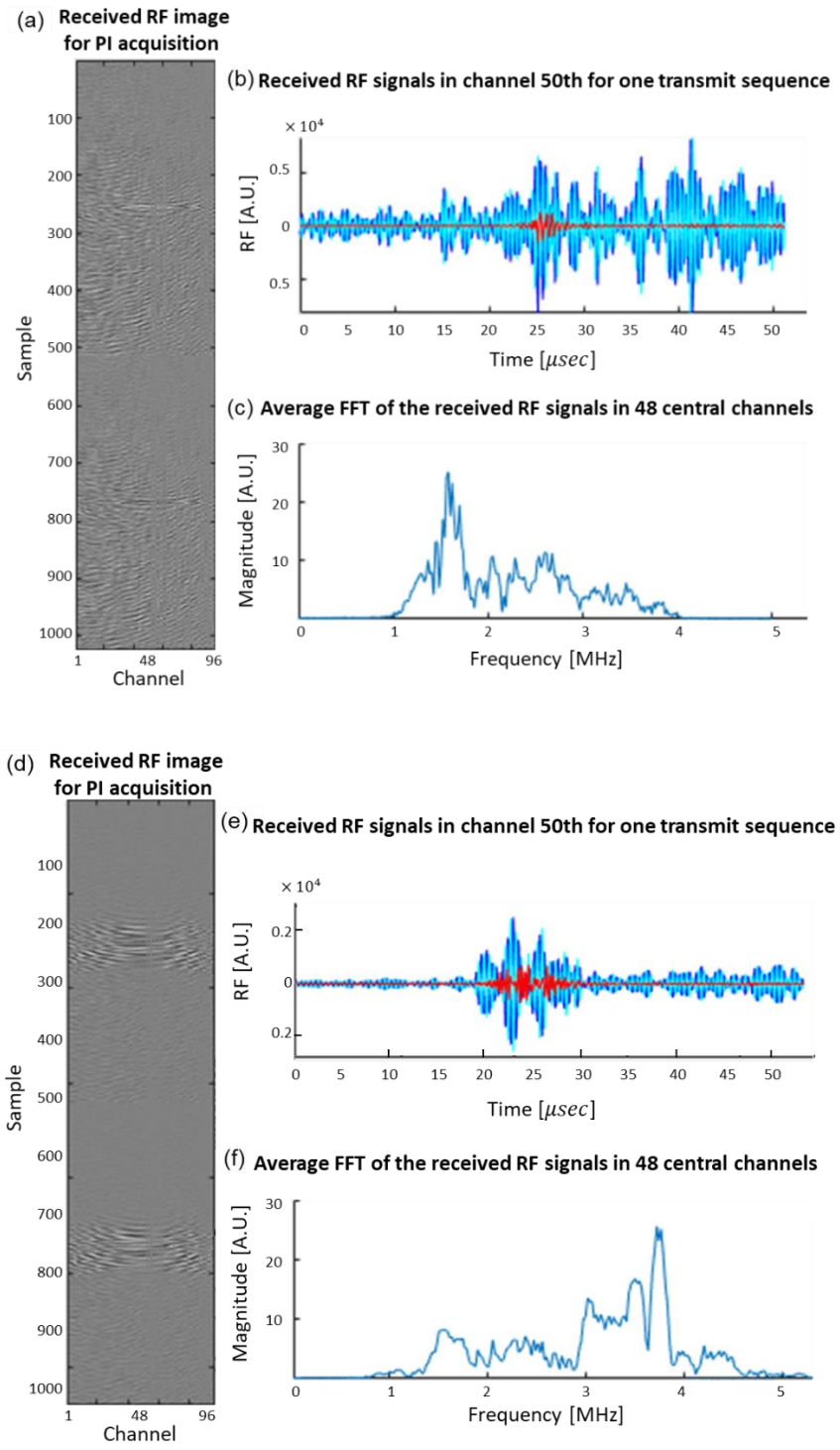

Figure 29. A real-time display of received RF signals by 96 elements, for one transmitted sequence, containing two phase-inverted pulses. (a),(b) and (c) refer to the dual-frequency transmit of 2 MHz & 3.5 MHz, whereas (d),(e) and (f) refer to a standard transmit of 2 MHz. (a) and (d) are the received RF image from 1024 samples. (b) and (e) are the received (by the 50th element), two echoes in the time domain (light and dark blue), whereas the red signal is their sum. (c) and (f) are the average frequency spectrum of the obtained RF data detected by the central 48 elements.

Subfigures (b) and (e) perform the two backscattered RF signal-responses to the PI pulses, detected by the 50th element, one on top of the other (light and dark blue), for two transmits respectively. When enlarging the RF graph, see Figure 30, it can be noted, that there is a phase delay between the two blue RF signals, as expected for the PI sequence. In addition, their sum (red signal) is mainly zero, except for a very specific time region, around the 25 μsec, where the US wave reached the MBs inclusion in the phantom, which responds nonlinearly and therefore, the echoes of the two signals are not canceled at their sum.

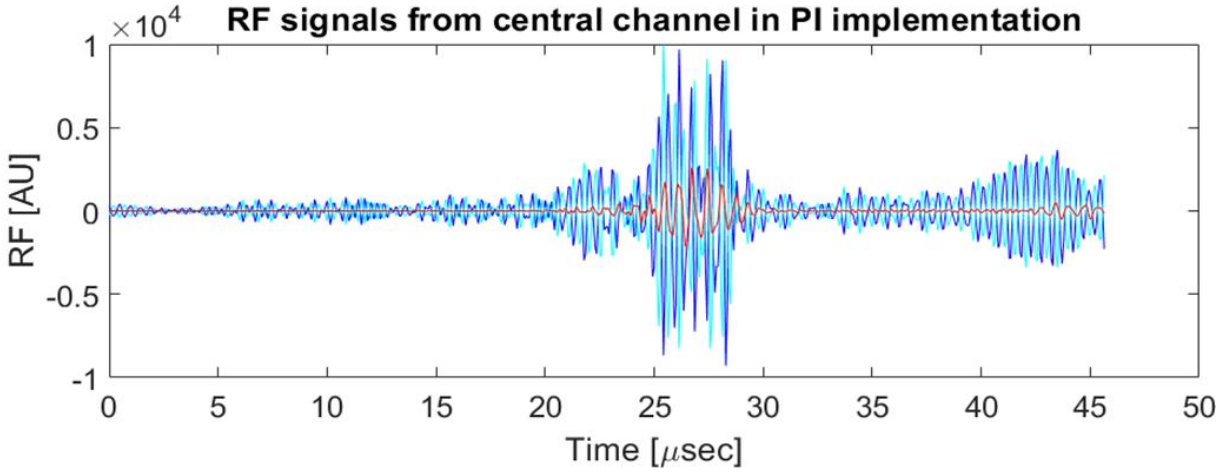

Figure 30. Zoomed-in display of the received two backscattered RF signals, light and dark blue, corresponding to the two phase-inverted pulses at one PI transmit sequence, detected by the central channel in real-time. The sum of the two echoes is represented by the red signal.

To explore the backscattered signal and its frequency content, Fourier transform (FT) of the received RF signals was also performed in real-time. An absolute average frequency spectrum of PI image acquisition is displayed in subfigures 29. (c) and (f). To do so, FT was calculated followed by the sum of the two obtained echoes from each channel (FT was calculated on each channel separately). Then the resulting FT matrix was normalized and averaged. To display the specific echoes returned from the MBs, the averaging was performed on the 48 central channels (elements), which were in front of the MBs inclusion in the phantom.

It can be noticed, that 29. (c) has a significant dominant frequency component around 1.5 MHz, which is the difference frequency for the dual-frequency transmit 2&3.5 MHz, whereas the dominant frequency component of the echoes is 29. (f), is about 3.8 MHz, which is close to the second harmonic of the 2 MHz transmit. As a result of the transducer's BW limitation, its exact 2nd harmonic (4 MHz) component, was attenuated.

5 Results

5.1 Simulation results

Three different transmit signals were simulated: 2 MHz, 3.5 MHz, and the dual-frequency 2&3.5 MHz (Figure. 31). All transmits had the same MI of 0.07. The spectral representation of the excitation signals accurately reflects the transmitted frequencies. These excitation signals (Figure. 31 (a),(c),(e)), were subsequently used as the input signals for MBs excitation using the Marmottant model. The MB response to the excitation waveforms was evaluated by their temporal expansion ratio (Figure. 32 (a),(d),(g)), which is defined by :

$$Expansion\ ratio = \frac{R(t)}{R_0}, \tag{35}$$

where R_0 is the resting MB radius, and R(t) is the changing radius as a function of time. Since the same MI was used for the excitation of the MBs, almost a similar expansion ratio of 0.85 (<1 for contraction), was achieved for the three different excitation waveforms. The Fourier transform of the temporal response signals revealed that the MBs spectrum contained the fundamental frequency as well as the 2nd harmonic for the 2 MHz excitation (Figure. 32(b)). Since the excitation was only with a single transmit with a positive polarity, the fundamental frequency (2 MHz) is not canceled and its amplitude is dominant compared to the 2nd harmonic (4 MHz).

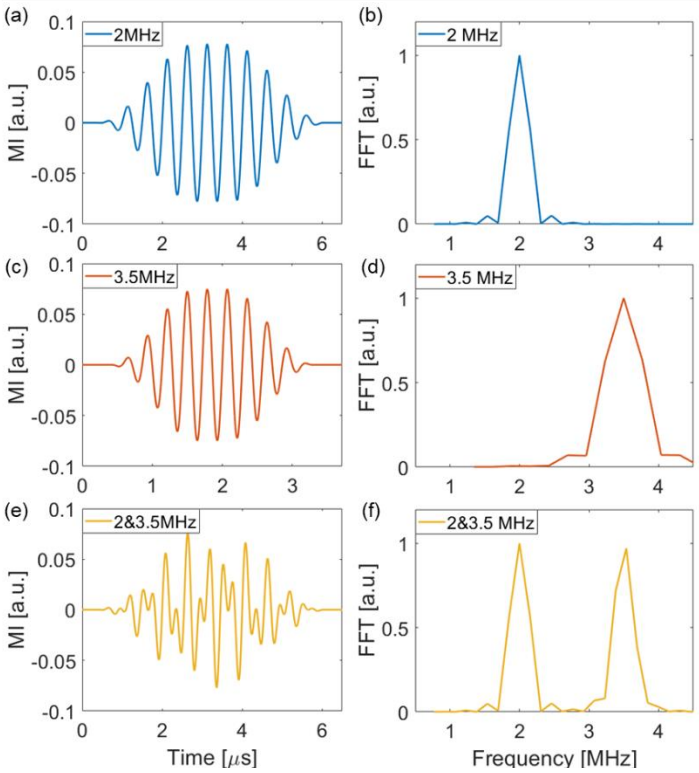

Figure 31. Excitation signals are used in the Marmottant simulation. Axes are common to subfigures (a),(c),(e), and to (b),(d),(f) respectively. Temporal excitation waveform at a center frequency of (a) 2 MHz, (c) 3.5 MHz, and (e) a superposition of 2 & 3.5 MHz. The three waveforms have the same mechanical index (MI) of 0.07. (b),(d),(f) Frequency domain representation using fast Fourier transform (FFT) of the temporal excitation signals in (a),(c),(e) respectively.

Notably, since the transducer's BW is 1-4 MHz, and the 2nd harmonic of the 3.5 MHz excitation is 7 MHz, which is beyond the cutoff frequency of the transducer, its spectrum contained only the fundamental frequency (Figure. 32(e)). For the dual-frequency excitation, aside from the fundamental frequency and the 2nd harmonic, the difference frequency at 1.5 MHz is also generated (Figure. 32(h)).

Next, the response of MBs to PI excitation was computed by exciting the MBs with a positive excitation waveform (+1) and then with a negative excitation waveform (-1), while summing the MBs responses. As a result, the fundamental frequencies are canceled (Figure. 32(c),(f),(i)). For the 3.5 MHz frequency, since the 2nd harmonic is not within the transducer BW, the signal is

eliminated (Figure. 32(f)). For the dual-frequency PI imaging, the amplitude of difference frequency at 1.5 MHz is 2.6 folds higher than the 2nd harmonic at 4 MHz. Interestingly, for the dual-frequency, the 2nd harmonic of the difference frequency (i.e. 3 MHz), and the subharmonic of the sum frequency (i.e. 2.7 MHz), are also detected.

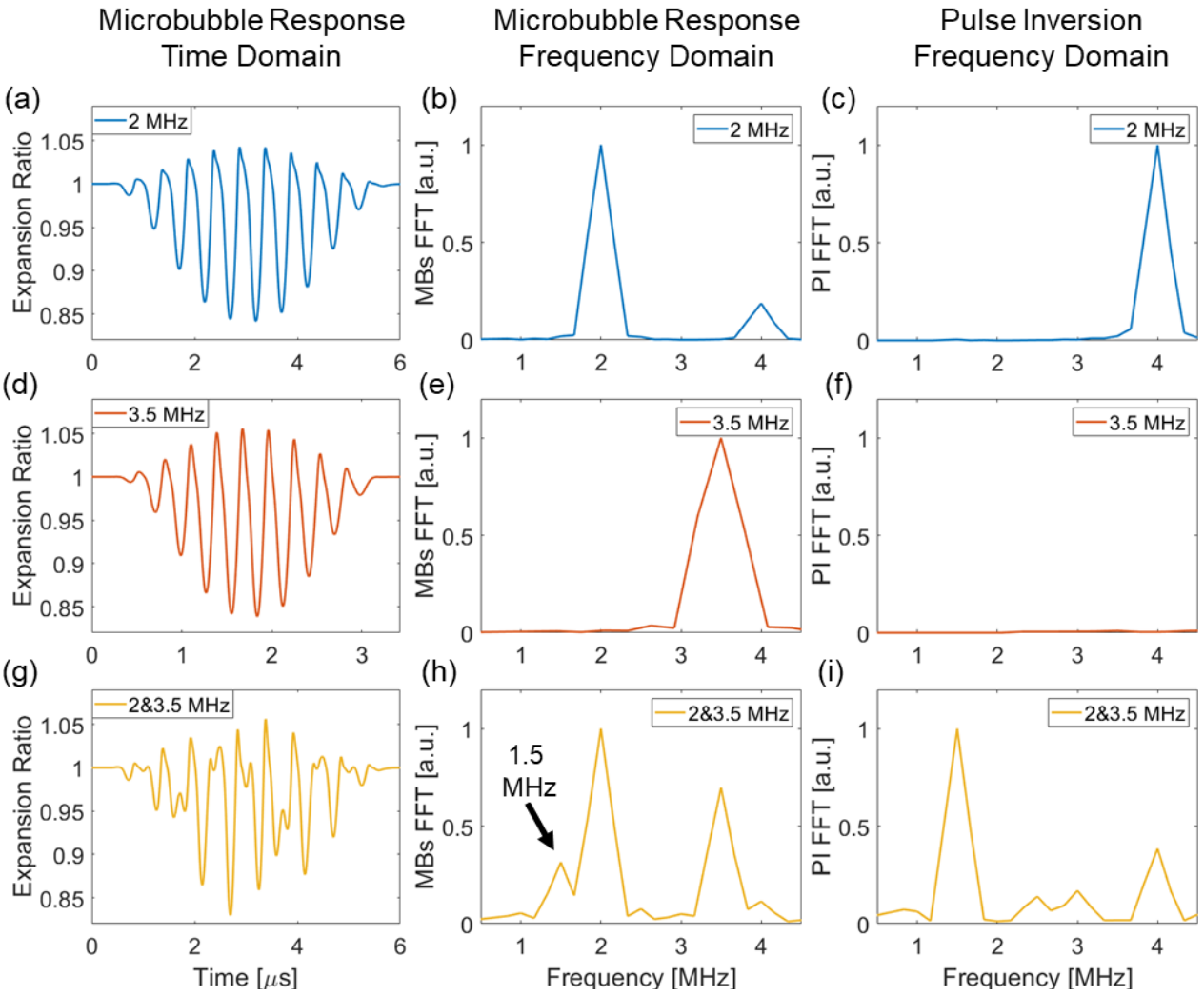

Figure 32. Simulated microbubble (MB) response. Axes are common to subfigures (a),(d),(g), and to (b),(c),(e),(f),(h),(i), respectively. Temporal MB response, in terms of expansion ratio, when excited by a center frequency of (a) 2 MHz, (d) 3.5 MHz, and (g) a superposition of 2&3.5 MHz. (b),(e),(h) Frequency domain representation of the temporal MB response for center frequencies of (a),(d),(g), respectively. Frequency response of MB following pulse-Inversion (PI) excitation at center frequencies of (c) 2 MHz, (f) 3.5 MHz, and (i) 2&3.5 MHz.

5.2 Experiment results

5.2.1 Hydrophone measurements and spectra validation

For initial validation of the method, multi-cycle excitations were used, resulting in narrow spectral components, which facilitate the detection of the difference frequency component. Hydrophone measurements of the transmitted dual-frequency waveform containing a 10-cycle PW excitation confirmed the presence of the 2 MHz and 3.5 MHz frequency components (Figure. 33(a),(b)). Since the measurement was performed in a water tank without MBs, the spectrum does not contain the difference frequency. These results are similar to the simulated transmitted signals (Figure. 31(e),(f)).

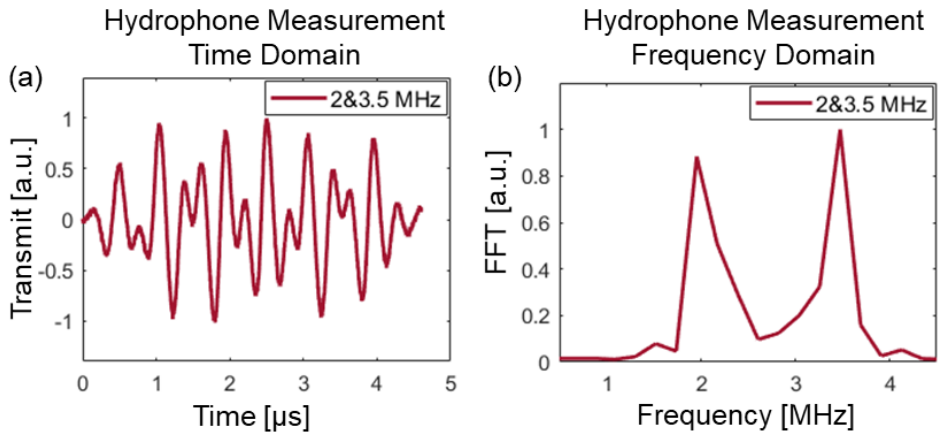

Figure 33. Hydrophone measurement of the transmitted dual-frequency waveform (2&3.5 MHz), with a 10-cycle plane-wave (PW) excitation. (b) Fast Fourier transform (FFT) of the temporal transmit signal in (a).

To validate the MBs response experimentally, a 10-cycle PW with a frequency of either 2 MHz, 3.5 MHz, or 2&3.5 MHz, was transmitted to image a tissue-mimicking phantom with inclusion at its center, filled with MBs (Figure. 27). The recorded echoes were captured by the phased array transducer, and Fourier transform was applied to the received radio frequency signals in each channel, to display the spectrum in real-time, either for a single PW transmit Figure. 34(a)), or for PI HI (Figure. 34(b)). When transmitting a single PW, the spectrum of the receive contains mainly the fundamental frequency for each transmit (Figure. 34(a)). However,

in PI imaging, the difference frequency at 1.5 MHz had the highest amplitude, whereas the second harmonic for the 3.5 MHz frequency is not detected (Figure. 34(b)), in agreement with the numerical simulations.

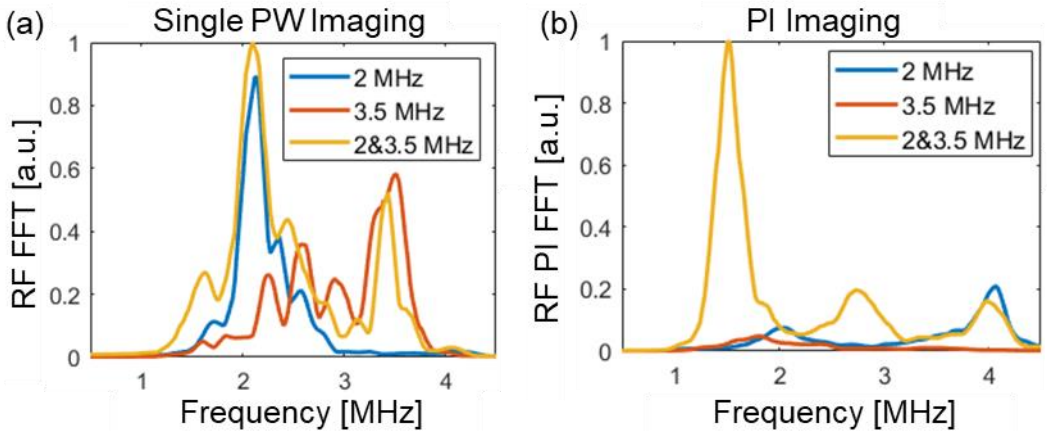

Figure 34. (a) Received spectrum following a 10 cycle plane-wave (PW) transmission with frequencies of 2 MHz (blue line), 3.5 MHz (orange line), and the dual-frequency 2&3.5 MHz (yellow line). (b) Received spectrum following pulse inversion (PI) imaging with frequencies of 2 MHz (blue line), 3.5 MHz (orange line), and the dual-frequency 2&3.5 MHz (yellow line). Axes are common to subfigures (a), and (b).

For imaging applications, a 1-cycle excitation was used to maximize axial resolution and eliminate the need for additional post-processing. Therefore, hydrophone measurements of a 1-cycle pulse of 2 MHz, 3.5 MHz, and the dual-frequency 2&3.5 MHz frequencies were recorded and displayed in Figure 35.

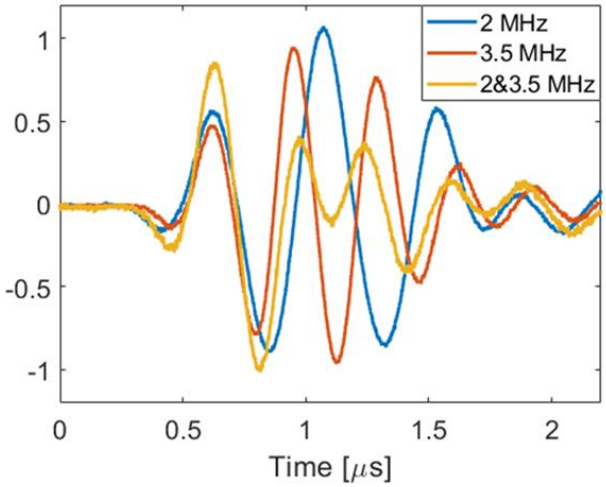

Figure 35. Hydrophone measurements of 1-cycle transmit pulses, with frequencies of 2 MHz (blue line), 3.5 MHz (orange line), and the dual frequency of 2&3.5 MHz (yellow line).

5.2.2 Axial resolution experiment

In order to assess the axial resolution for each method, imaging of a 50 µm wire target in a water tank, was performed either with a 2 MHz or 2&3.5 MHz 1-cycle, at a depth of z=45 mm (Figure 36(a),(b)). The FWHM of the results was calculated from the axial cross-sections, yielding values of 1.05 mm and 1.02 mm for 2 MHz and 2&3.5 MHz, respectively (Figure 36(c)). This result confirms that the proposed CHI approach does not affect axial resolution, which remained similar to a single frequency imaging at 2 MHz.

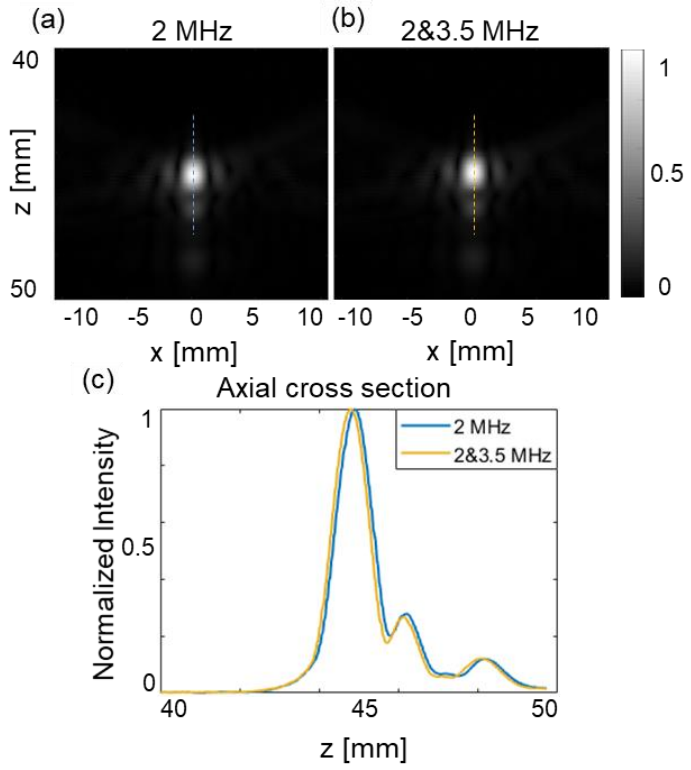

Figure 36. Experimental imaging results of a wire target in water at 45mm, obtained using a 1-cycle pulse of 5v with (a) single-frequency transmit of 2 MHz, and with (b) dual frequency transmit of 2&3.5 MHz. (c) Normalized axial cross-section profiles of the blue and yellow dashed lines marked in (a),(b), respectively.

5.2.3 Ultrasound imaging experiments with a tissue-mimicking phantom

After confirming the generation of the difference frequency experimentally, the performance of the method had to be evaluated for real-time imaging. To do so, a 1- cycle transmission was used for imaging the MBs-filled inclusion within the tissue-mimicking phantom (Figure. 27(c)).

5.2.3.1 Linear imaging

Initially, the phantom was imaged using standard linear imaging with coherent compounding at a center frequency of 2 MHz, 3.5 MHz, 2&3.5 MHz, where a hyperechoic lesion is observed due to MBs presence, with a strong speckle background. Figure. 37 (b)-(d) are screenshots of those linear output images from the US system during those tries.

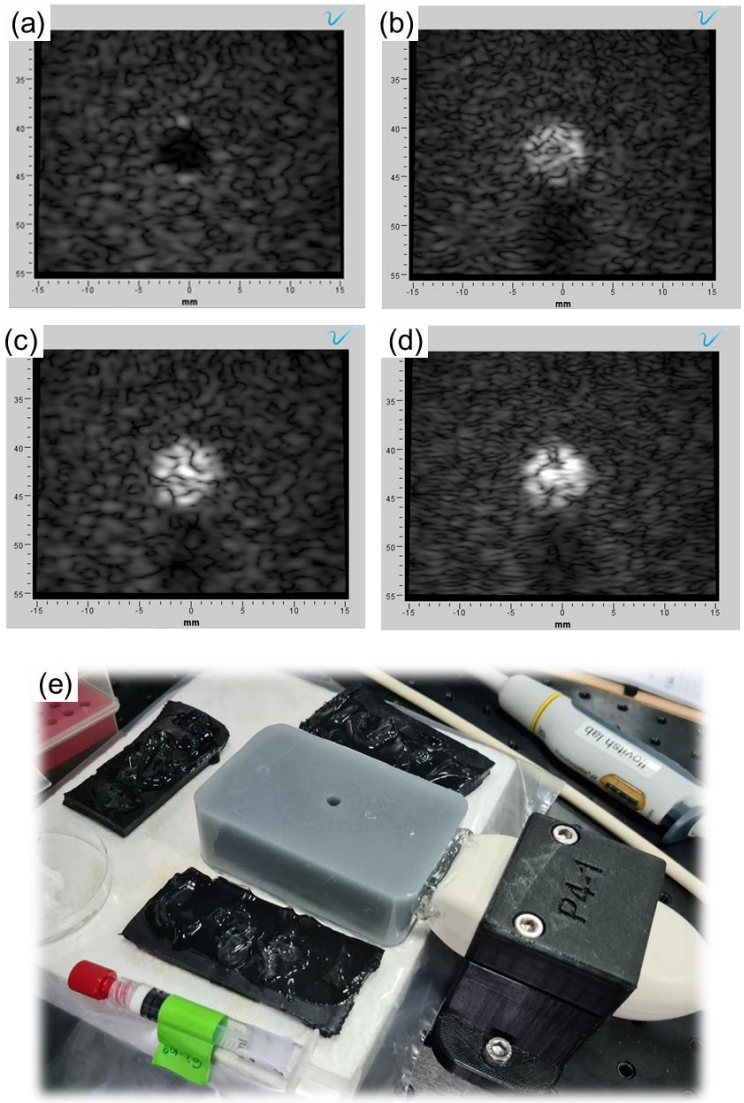

Figure 37. Screenshots of fundamental, linear imaging of a tissue-mimicking phantom with coherent compounding, provided by Verasonics US system. (a) Before MBs injection and (b)-(d) after. Images were acquired with 5v at a center frequency of (b) 3.5 MHz, (c),2 MHz, and at (d) 2&3.5 MHz. (e) Ultrasound set-up for imaging experiments. MBs suspension was injected into a cylindrical cavity in tissue-mimicking agar phantom with SiC powder, as scatters. The phantom was covered by Neoprene rubber with US gel for noise reduction caused by air refraction.

Figure 7(a) is the resulting image before MBs suspension was injected into the cylindrical cavity (contains pure PBS), therefore, the dark anechoic cyst appearance, instead of the bright hyperechoic lesion. In addition, during the experiments, it was found that, at high concentrations of MBs, there is a blockage of the US beam and a shadow appears below the MBs lesion (Figure 37(b)-(d)). Sometimes, it even transforms MB's circular shape in the image, into a "moon" shape. Therefore, concentrations were decreased and optimized, such that the obtained image would not have these artifacts but still have a strong MBs echo-response. Afterward, PI imaging was applied, reducing the tissue speckles background and enhancing the MBs signal. At the first attempts, the resulting PI images contained artifacts, noise, and MBs inclusion shape was not a perfect circle. That led to the idea of wrapping the phantom with Neoprene rubber (Figure 37(e)), which is known for its high acoustic attenuating properties. This insulation material was used to reduce image noise produced by returning echoes from phantom's boundaries caused by air refraction.

5.2.3.2 Contrast harmonic imaging and frequency mixing

After solving the noise and MBs concentration issues, the obtained PI images for the three different transmits were saved and displayed at a linear scale (Figure. 38(a),(b),(c)) and 50 dB scale (Figure. 38(d),(e),(f)), as commonly used in the diagnostic US. The first noticeable result is that, in the 50 dB scale, the background signals from the scatterers in the phantom are not completely canceled with the PI technique, but it is so weak that in the linear scale, it is neglected. In addition, since the 2nd harmonic of the center frequency of 3.5 MHz is beyond the cutoff frequency of the transducer, PI imaging with 3.5 MHz transmit (Figure. 38(b),(e)) yield a poor signal from MBs inclusion, compared to PI imaging with 2 MHz (Figure. 38(a),(d)) or the dual-frequency 2&3.5 MHz (Figure. 38(c),(f)) transmits. When comparing the last two (2 MHz and

2&3.5 MHz) qualitatively, it seems that the MBs signal for the dual-frequency transmit is indeed slightly stronger than for the 2 MHz transmit. However, when looking at their performances on a 50 dB scale, the background of the 2&3.5 MHz, has a speckle noise as much as the 2 MHz background. Therefore, quantitative contrast analyses were calculated for these two PI images (Figure. 38(d) and (f)), as described in 4.2.4. The resulted contrast values were 30.9 dB and 33.5 dB in favor of the dual-frequency method.

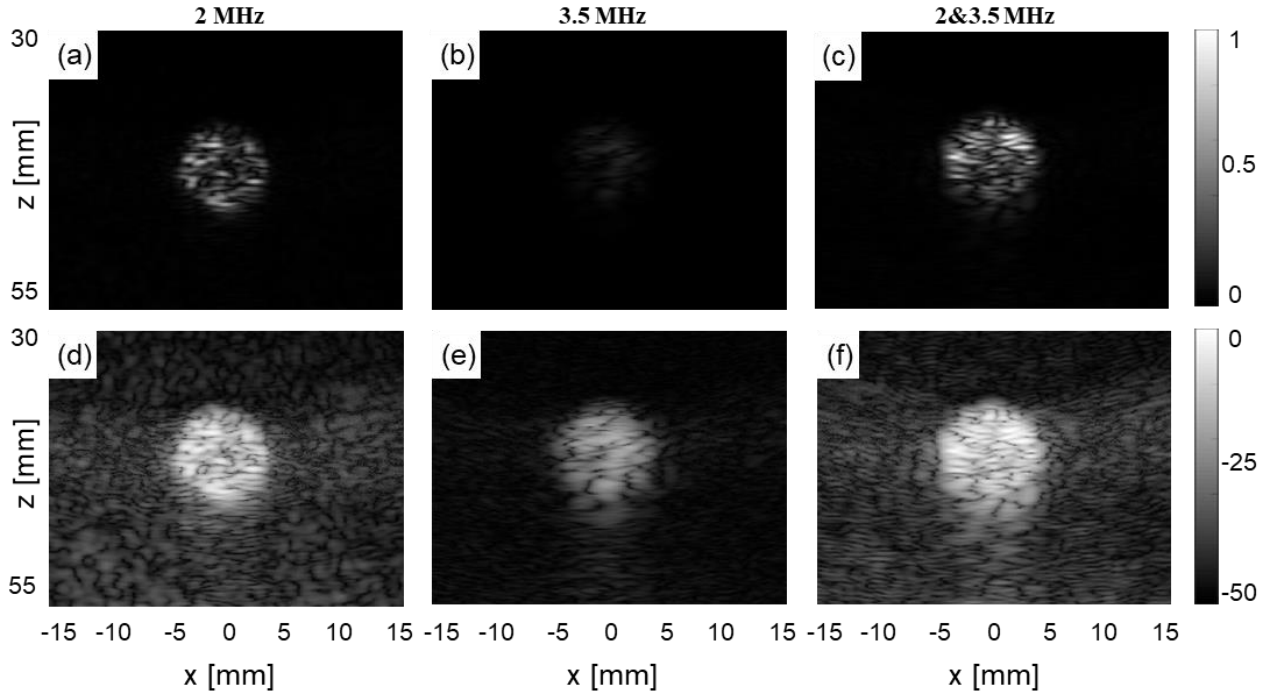

Figure 38. Exemplary results of pulse inversion (PI) imaging of the MBs inclusion in the tissue-mimicking phantom for three transmits with a center frequency of (a),(d) 2 MHz; (b),(e) 3.5 MHz and (c),(f) dual-frequency of 2&3.5 MHz. All images were acquired with a 1-cycle of 5v pulse. (a),(b),(c) are presented in linear scale and (d),(e),(f) in 50 dB scale. Axes are common to all subfigures.

Because of the transducer's BW limitation, which leads to the absence of the 2nd harmonic of the 3.5 MHz transmit, it was decided to continue the following experiments and their contrast analysis only with the two transmits of the 2 MHz and the dual-frequency transmits. Moreover, these two transmits are enough to test our hypothesis, by comparing PI imaging based on the 2nd

harmonic only against the frequency mixing method, specifically, based on the difference frequency echoes.

5.2.4 The effect of the receive center-frequency on the contrast

In parallel with the quantitative analysis of the obtained imaging contrast with the proposed method, we examined also the influence of the center-frequency defined for the **receive**, $f_{receive}$ through three experiments. Figure 39, displays some exampled images obtained with different transmit and receive frequencies, with the same applied MI:

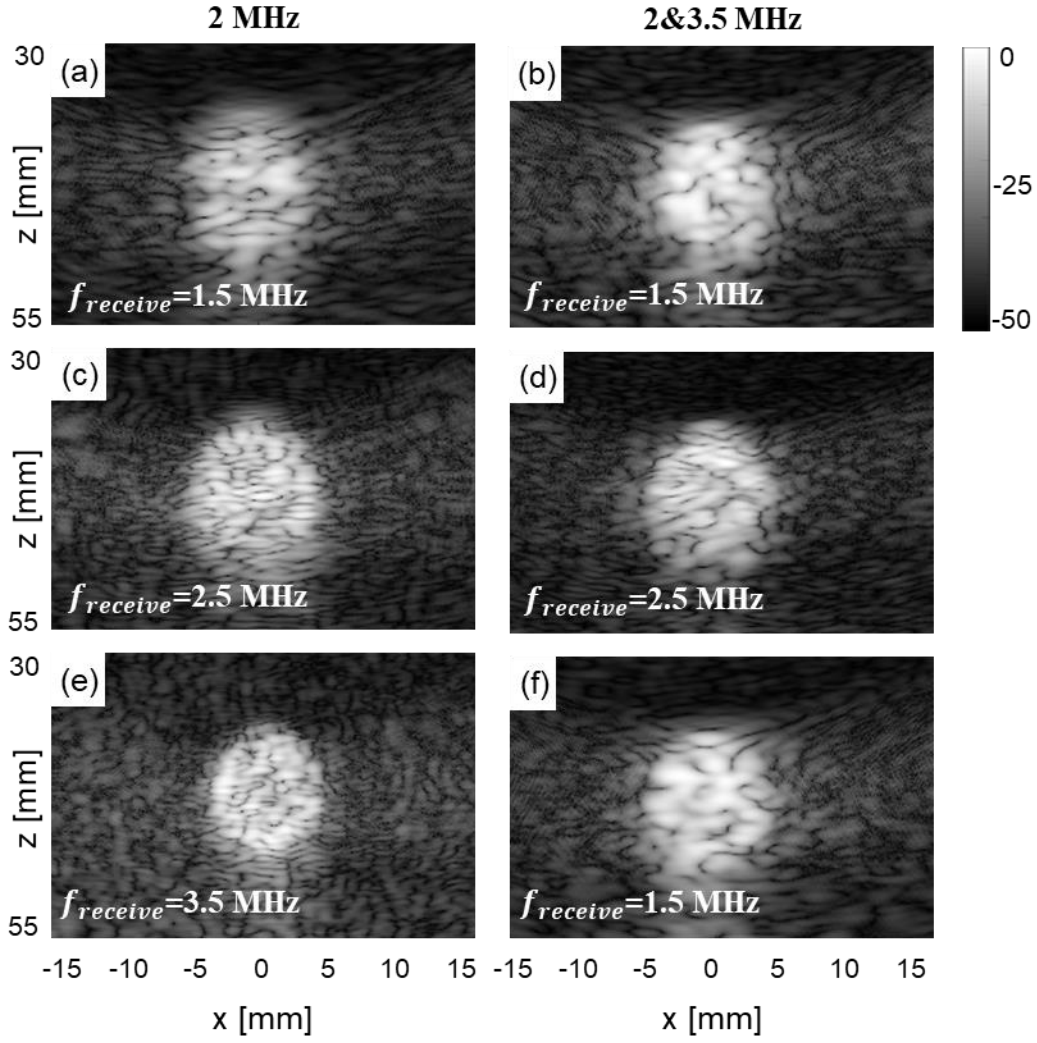

Figure 39. Exemplary results of pulse inversion (PI) imaging of the tissue-mimicking phantom obtained by (a),(c),(e) 2 MHz transmit against the (b),(d),(f) dual-frequency of 2&3.5 MHz transmit for the frequency

mixing effect. The two methods were compared for three receive center frequencies: (a),(b) 1.5 MHz, (c),(d) 2.5 MHz, and (e),(f) adjusted to the expected non-linear frequencies (e) 3.5 MHz for the generation of the 2nd harmonic at 4 MHz and (f) 1.5 MHz for the generation of the difference frequency at 1.5 MHz.

Subfigures (a),(c), and (e) represent exemplary results of PI imaging of the tissue-mimicking phantom obtained by 2 MHz transmit, whereas the (b),(d), and (f) are examples of the 2&3.5 MHz transmit for the frequency mixing effect. The images in Figure 39 were obtained with a receive frequency of: 1.5 MHz ((a) and (b)), 2.5 MHz ((c) and (d)), and the adjusted frequency((e) and (f). For the last pair, $f_{receive}$ was determined according to the expected non-linear frequencies: (e) 3.5 MHz, for the generation of the 2nd harmonic at 4 MHz, and (f) 1.5 MHz, for the generation of the difference frequency at 1.5 MHz.

For quantitative evaluation of the two PI methods for different receive frequency, contrast ratios, CR [dB], were calculated by (17). The MB's contrast was presented as a function of MI, at 2 MHz (orange line), and dual-frequency of 2&3.5 MHz (green line), in Figure 40(b),(d),(f) with 1.5 MHz, 2.5 MHz, and adjusted receive frequency, respectively. For statistical analysis, three pairs of PI images were sampled for each MI. Figure 40 summarizes the all resulted contrast ratios at the three experiments with the different receive frequencies, for the two PI methods and five MI values, between 0.04 to 0.18. The results are plotted as mean ± STD with their obtained p values, **p <0.01 ***p <0.001, ****p <0.0001, based on two-way ANOVA with Bonferroni's multiple comparisons tests. Subfigures (a),(c),(e), contain the detailed lists of the results plotted in (b),(d),(f), in Figure 40.

In the first experiment, where the receive center-frequency was set to 1.5 MHz (Figure.40 (a),(b)), the PI with the dual-frequency transmit, achieved a maximal contrast improvement of 3.43 ± 1.34 dB (p<0.0001). Notably, the contrast at an MI of **0.18** for the 2 MHz frequency was 27.8 ± 0.7 dB, compared to the contrast at a MI of **0.04** for the **dual-frequency** that was 28.85 ±

0.8 dB. This implies that the MI can be reduced by a factor of 4.5 for the dual-frequency transmit and the resulting contrast will remain higher than PI with 2 MHz. At the second experiment, where the center-frequency was set to 2.5 MHz, the dual-frequency PI achieved a maximal contrast improvement of 2.84 ± 1.21 dB ($p<0.001$). At the third experiment, where the receive center-frequency was adjusted to the transmitted signal, 1.5 MHz / 3.5 MHz for transmit of 2&3.5 MHz / 2 MHz respectively, the dual-frequency PI achieved a maximal contrast improvement of 3.71 ± 0.87 dB ($p<0.0001$).

(a)

$f_{receive}$=1.5 MHz

MI	Contrast Enhancement [dB] ± STD
0.04	3.43 ± 1.34
0.07	2.95 ±0.65
0.11	3.02 ±1.12
0.14	2.81 ±0.89
0.18	2.51 ±0.84

(b)

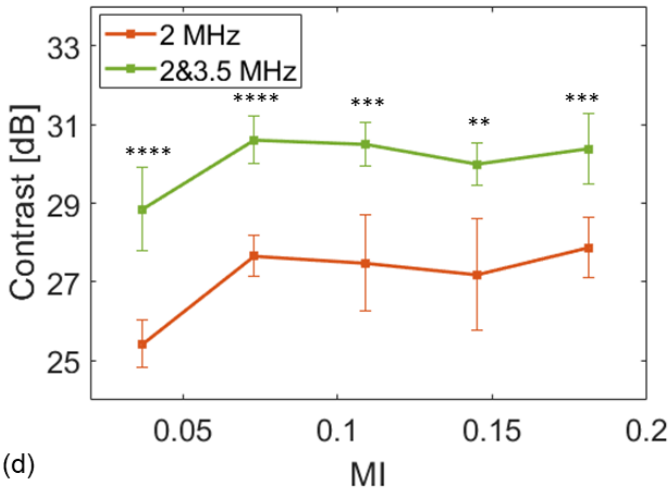

(c)

$f_{receive}$ =2.5 MHz

MI	Contrast Enhancement [dB] ± STD
0.04	1.94 ± 1.43
0.07	2.38 ±0.55
0.11	2.30 ±0.80
0.14	2.50 ±0.80
0.18	2.84 ±1.21

(d)

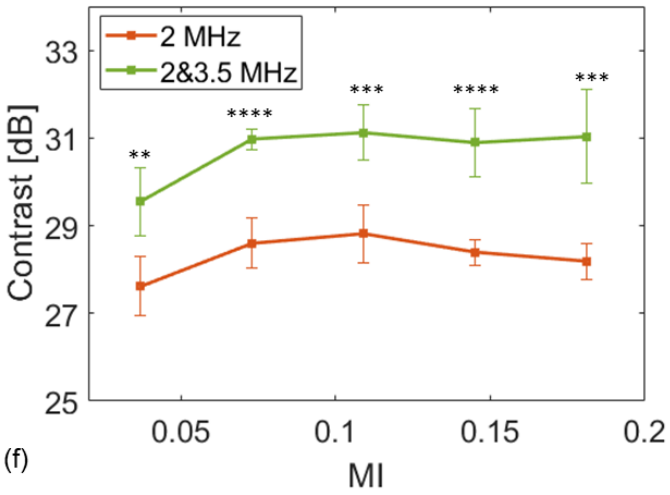

(e)

$f_{receive}$ =1.5 MHz / 3.5 MHz

MI	Contrast Enhancement [dB] ± STD
0.04	2.50 ± 1.83
0.07	3.71 ±0.87
0.11	2.95 ±1.48
0.14	2.60 ±0.59
0.18	2.31 ±0.85

(f)

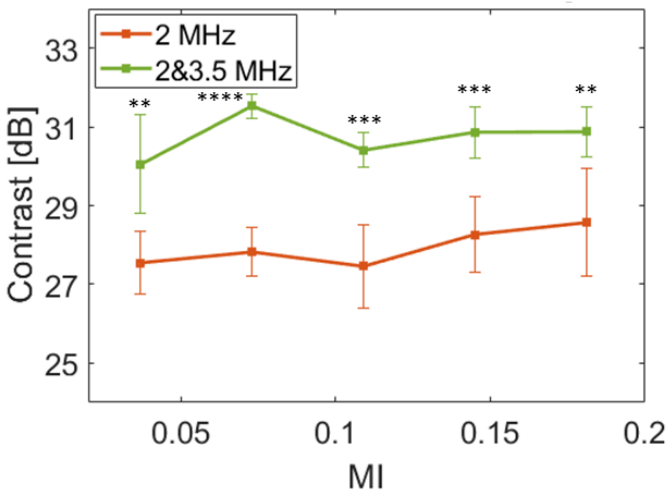

Figure 40. The Contrast enhancements with the dual-frequency transmit for the different MI values and the three receive center-frequency, are listed in (a)$f_{receive} = 1.5\ MHz$, (c) $f_{receive} = 2.5\ MHz$ and (e) $f_{receive} = 1.5/3.5\ MHz$ for the adjusted receive center-frequency. Contrast measurements of the two PI methods, plotted as mean ± STD with their obtained p values, **p <0.01 ***p <0.001, ****p <0.0001 in (b),(d),(f) for the three receive center-frequency, respectively.

5.2.5 MBs concentration optimization

The dependence of the MBs' concentration on the imaging contrast results was examined through imaging experiments (of the phantom with the MBs). Three PI images were acquired for 6 different concentrations, from $4 \cdot 10^5$ to $1 \cdot 10^8$ $\frac{MBs}{ml}$, with the three transmit signals: 2 MHz, 3.5 MHz, and 2& 3.5 MHz, applying the same MI of 0.07. The contrast results are summarized in the following graph :

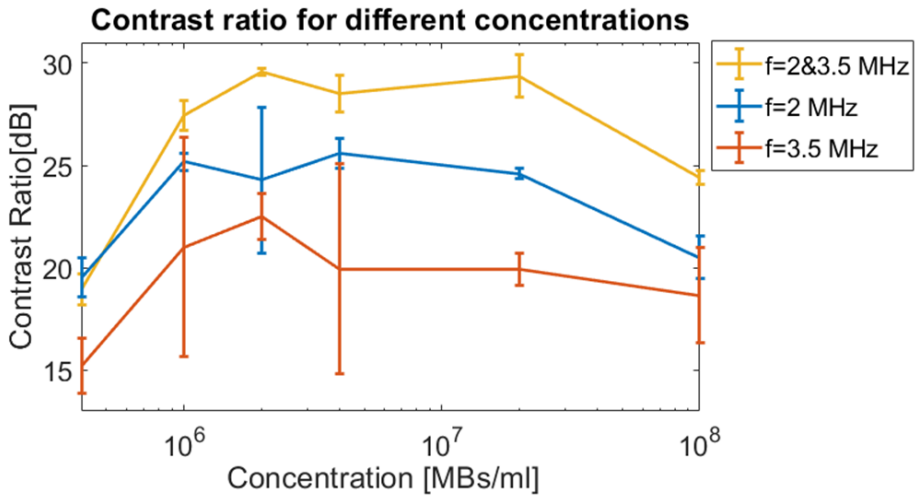

Figure 41. Contrast ratio results for 6 different microbubbles (MBs) concentrations in the imaged phantom. Three transmits are compared: 2 MHz (blue), 3.5 MHz (orange), and frequency mixing with 2&3.5 MHz (yellow).

It may be noticed, that starting from a concentration of $2 \cdot 10^6$ $\frac{MBs}{ml}$, the contrast ratio reaches a plateau and there is no further improvement, in all three transmits. In addition, starting from $2 \cdot 10^7$ $\frac{MBs}{ml}$, there is even a decrease in contrast, due to the blockage of the US waves by the MBs. The US beam fails to penetrate the entire inclusion and significantly reduces the imaging performance in all transmits. What is important to note is that our method achieves a higher contrast for all concentrations.

5.2.6 The effect of the number of transmitted plane-waves

In the main imaging experiments, the coherent compounding was implemented with 9 angles for the positive pulses emissions and 9 angles for the negative pulses emissions, hence a total of 18 PW emissions. To test the versatility of the method, we examined how the number of angles

affects the CHI contrast improvement. To do that, we repeated the experiments with 3 angles PW, yielding a total of 6 PW emissions. When comparing the 2 MHz and the 2&3.5 MHz transmits, the frequency mixing method still performed higher contrast results. The general contrast ratios were lower for both methods, but the dual frequency transmit achieved higher, by 2.8 dB, results (Figure 42).

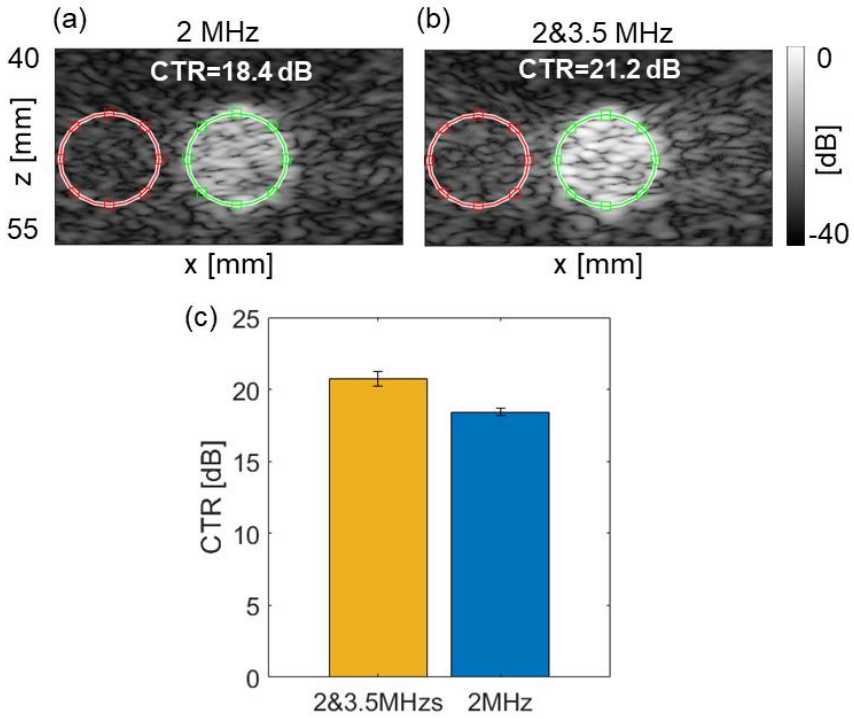

Figure 42. Contrast ratio results for 3 angled plane-waves for (a) 2 MHz (blue) and (b) 2&3.5 MHz(yellow).

6 Discussion

CHI with MBs is a growing field with many clinical applications including vascular imaging [79], cancer diagnosis and monitoring [80], [81], cardiac imaging [82], and super-resolution imaging [83]. This method offers higher contrast, sensitivity, and specificity compared to standard HI. Yet, it suffers from reduced contrast due to tissue nonlinearity and weaker harmonic signals compared to the fundamental frequency. In this study, we developed an enhanced CHI method by triggering an additional mechanism of frequency mixing that adds nonlinear

components and amplifies the MBs signal for a greater image contrast enhancement. Due to advances in US programmable systems, greater freedom and flexibility in designing custom pulse sequences and imaging methods now exist. The implementation of the method in real-time using a single array transducer was feasible here due to the AWG feature in the programmable system that enables control of the transmit of custom pulse sequences to individual elements, precisely. This facilitates the development of new imaging methods that were not applicable in the past [84]. Here, the frequency mixing mechanism was generated by exciting the MBs with a dual frequency waveform that was engineered as the superposition of two different frequencies and transmitted via the AWG in the programmable US system. Notably, while the method requires a custom transmit, on receive, standard dynamic beamforming was used. Hence, no additional post-processing was required and the built-in beamformer displayed the image in real-time .

Our approach has several advantages over previous works. While most dual-frequency excitations were performed by mechanically aligning two single element transducers combined with the mechanical movement of the sample [19], [69], in this study, the method is implemented using a single transducer that can be electronically steered. Furthermore, it does not require dividing the transducer elements into two groups for each frequency component but rather uses the entire aperture to transmit the frequency multiplexed waveforms [85]. Further, 1-cycle excitation can be used here, eliminating the need for filtering and additional post-processing when using multi-cycle transmissions [13], [19], [41], [86]. This is a major step towards a practical implementation, that had not been demonstrated previously, and is a paradigm shift in implementing dual-frequency excitations with a single array transducer. Moreover, since the method utilizes coherent compounding of angled PW, and does not require focusing, the obtained frame rate is enhanced .

The method was implemented with a broadband transducer (P4-1), to include both transmitted frequencies (2 and 3.5 MHz), as well as their difference frequency (1.5 MHz). The method is likely applicable for any other commercially available broadband transducer, given an informed choice of the transmitted frequencies and the difference frequencies. Conversely, array-based dual frequency transducers are currently being developed and might further enhance the method's performance [87], [88].

Another important contribution of the proposed method is that it allows better utilization of the transducer's bandwidth. For example, since the transducer used in this study has a bandwidth of 1-4 MHz, CHI at a frequency of 3.5 MHz is not feasible since its harmonics are beyond the transducer bandwidth. However, by taking advantage of the frequency mixing effect, we can use this frequency, enabling an effective usage of the transducer's bandwidth.

Numerical simulations were performed to assess the MB response to a dual-frequency excitation and confirmed the generation of the difference frequency, both when transmitting PW or when using PI CHI (Figure 32. (h),(i)). To accurately compare the different excitation frequencies, all waveforms were transmitted with the same MI, such that the resulting expansion ratios remained similar. It should be noted that the sum frequency is also generated, however, the difference frequency has a lower attenuation and was reported previously to improve image quality in general HI [17] and hence was the focus of our study. The tissue-mimicking phantom experiments with the MBs-filled inclusion aimed to affirm the numerical simulations via an experimental observation and to assess the method's performance when used for imaging with a 1-cycle transmission (Figure 35-42). To validate the generation of the difference frequency experimentally, a multi-cycle waveform was transmitted either for 2 MHz, 3.5 MHz, or 2&3.5 MHz. The received radio frequency signals were captured by the transducer and displayed in

real-time (Figures 29 and 30), for validating the numerical simulations and revealing that the difference frequency has a higher amplitude compared to the standard 2nd harmonics (Figure 34. (b)).

Imaging of the MBs-filled inclusion was performed with PI CHI based on coherent compounding of angled PW (Figure 38). Implementation of CHI can be performed using multiple approaches, such as PI, contrast pulse sequencing, and amplitude modulation [89]. Although as a proof of concept we chose to use PI, the method is general and can be compatible with the other CHI techniques, and in the future might be incorporated into advanced CHI methods [90]. Since the 2nd harmonic of 3.5 MHz was beyond the cutoff frequency of the transducer, the received MBs signal in the PI image (Figure 38. (b) and (e)), was significantly lower than the 2nd harmonic of the 2 MHz frequency or the difference frequency of the dual-frequency transmit.

One of the main considerations when developing the PI imaging protocol, was to decide which center-frequency should be set for the receive, because it is not necessarily, has to be the same as in the transmit. Moreover, since we perform CHI and not fundamental imaging, the frequency components from the echoes that form the PI image are different from the transmitted center-frequency and therefore, setting it around the expected frequencies at the receive, may optimize the nonlinear image construction and reduce remained linear signals, that are likely to be removed. From all mentioned above, three different receive center-frequencies were tested through three PI imaging experiments, in addition to the two transmit methods comparison. All three experiments performed a significant contrast improvement for the dual-frequency transmit, in the range of 1.94 dB to 3.71dB (Figure 40). Since the improvements were relatively similar, it can be concluded, that the receive center-frequency does not drastically affect the contrast improvement results. Moreover, it confirms our claim, that the contrast enhancement is achieved

due to the frequency mixing effect and not because of the transducer BW. Notably, the maximal improvement was achieved when the receive center-frequency was set to 1.5 MHz, which is the difference frequency

All imaging results confirm that PI can suppress tissue background (e.g., Figure 38) compared to standard coherent compounding of the phantom (Figure 37). In addition, the dual-frequency transmit (e.g., Figure 39. (b),(d),(f)), enhances MBs signal, yielding a brighter inclusion compared to PI with a single frequency of 2 MHz (e.g., Figure 39. (a),(c),(e)). This is attributed to the generation of the difference frequency in addition to the standard 2nd harmonic. Quantitative evaluation of the method's performance in terms of contrast as a function of the MI (Figures 40), yielded a maximal contrast improvement of 3.71 ± 0.87 dB ($p<0.0001$). The results also confirm that for the dual-frequency transmit, the MI can be reduced by a factor of 4.5 and the contrast will remain higher than conventional PI CHI with a single frequency transmit. Thus, the method is applicable for imaging under poor conditions with low MI.

One limitation in this work was the high sensitivity to MB's concentrations, their movement, exploding, and floating, which affect the imaging performance. Therefore, MBs were replaced frequently and mixed with a pipette between each acquisition.

As for the versatility of the proposed method, it was confirmed that its advantage over the conventional PI imaging with a single frequency transmit, is achieved also for a variety of MBs concentrations and even when reducing to 3 PW angels imaging instead of 9.

7 Conclusions and future work

This thesis performed a study and development of an enhanced CHI method using MB contrast agents by triggering a nonlinear frequency mixing mechanism that amplifies their signal. The method is incorporated into a standard PI sequence, yet instead of transmitting a single frequency,

the waveform is replaced by a superposition of two frequencies. The resulting contrast is improved by a maximal 3.71 dB, without any additional post-processing. Thus, the method can be implemented in real-time on programmable US systems, and facilitate MBs-based CHI, while reducing the required MI by 4.5 folds. Therefore, the method can be applied to applications where contrast harmonic imaging is used and improve the resulting image contrast while decreasing the transmitted mechanical index. Specific applications of the method include abdominal imaging of obese patients [91]. The difference frequency has a lower attenuation and thus is likely to perform well in the variety of tissues that exist in vivo, yielding a higher image quality. Additionally, the method is likely to facilitate applications where low microbubbles concentrations are used such as in ultrasound localization microscopy [92]. Implementing the method for super-resolution and in vivo ultrasound imaging, will be evaluated in future studies. Moreover, the method can be beneficial for imaging clinical conditions that limit perfusion, which result in a low contrast image, such as acute coronary syndrome, vascular stenosis, and thrombosis [93]–[95].

The aim of the paper was to provide a proof of concept for the developed method, by testing its performance in numerical simulations, hydrophone measurements, and tissue-mimicking phantom experiments. In a future study, we will focus on applying the method in vivo, and evaluating its performance. The ability to image moving objects depends on the frame rate and the flow velocity. Since our implementation of PI has used a typical coherent compounding script, which is known for its advantages of high frame rate and has been previously demonstrated in-vivo imaging with MBs [52], we anticipate that our method could be able to succeed as well. Furthermore, the difference frequency has a lower attenuation and thus is likely to perform well in the variety of tissues that exist in vivo. Future work may also include optimizing the proposed method and the experimental set-up for a better contrast performance for example, by using a

wider bandwidth transducer, to detect also the generated sum frequency, in order to strengthen the MB's backscattered signal even more.

Contrast harmonic imaging is becoming a standard in all modern US devices and its advantages over the standard, linear imaging, have been demonstrated in breast, axillary lymph node, thyroid, hepatobiliary, pancreatic, genitourinary, cardiac, pediatric, and more imaging applications [9]. Therefore, new enhancements and improvements of this method can make it even more useful and essential in practice.

8 References

[1] Thomas L. Szabo, *Diagnostic Ultrasound Imaging: Inside Out*, 2nd ed. Elsevier Science & Technology, 2013.

[2] T. Ilovitsh, A. Ilovitsh, J. Foiret, B. Z. Fite, and K. W. Ferrara, "Acoustical structured illumination for super-resolution ultrasound imaging," *Communications Biology*, vol. 1, no. 1. 2018, doi: 10.1038/s42003-017-0003-5.

[3] O. H. Baltarowich *et al.*, "National ultrasound curriculum for medical students," *Ultrasound Q.*, vol. 30, no. 1, pp. 13–19, 2014, doi: 10.1097/RUQ.0000000000000066.

[4] S. V Ranganayakulu, N. R. Rao, and L. Gahane, "Ultrasound applications in Medical Sciences," *Int. J. Mod. Trends Eng. Res.*, vol. 3, no. 2, pp. 287–293, 2016.

[5] K. K. Shung, "Diagnostic ultrasound: Past, present, and future," *J. Med. Biol. Eng.*, vol. 31, no. 6, pp. 371–374, 2011, doi: 10.5405/jmbe.871.

[6] C. Kollmann, "New sonographic techniques for harmonic imaging-Underlying physical principles," *Eur. J. Radiol.*, vol. 64, no. 2, pp. 164–172, 2007, doi: 10.1016/j.ejrad.2007.07.024.

[7] T. Ilovitsh, A. Ilovitsh, J. Foiret, and K. W. Ferrara, "Imaging beyond ultrasonically-

impenetrable objects," *Sci. Rep.*, vol. 8, no. 1, pp. 1–11, 2018, doi: 10.1038/s41598-018-23776-7.

[8] T. Szasz, "Ultrasound imaging and the associated inverse problems," pp. 57–64, 2017, [Online]. Available: https://tel.archives-ouvertes.fr/tel-01506629v1/document.

[9] A. Anvari, F. Forsberg, and A. E. Samir, "A primer on the physical principles of tissue harmonic imaging," *Radiographics*, vol. 35, no. 7, pp. 1955–1964, 2015, doi: 10.1148/rg.2015140338.

[10] T. Albrecht *et al.*, "B-mode enhancement at phase-inversion US with air-based microbubble contrast agent: Initial experience in humans," *Radiology*, vol. 216, no. 1, pp. 273–278, 2000, doi: 10.1148/radiology.216.1.r00jl27273.

[11] H. Lee *et al.*, "Microbubbles used for contrast enhanced ultrasound and theragnosis: a review of principles to applications," *Biomed. Eng. Lett.*, vol. 7, no. 2, pp. 59–69, 2017, doi: 10.1007/s13534-017-0016-5.

[12] M. Ahmed and M. Aboellail, "ADVANCES IN MEDICAL ULTRASOUND: TISSUE HARMONIC IMAGING," 2017, Accessed: Sep. 25, 2021. [Online]. Available: https://www.researchgate.net/publication/323183899.

[13] S. Hirata, C. H. Leow, M. E. G. Toulemonde, and M.-X. Tang, "Selection on Golay complementary sequences in binary pulse compression for microbubble detection," *Jpn. J. Appl. Phys.*, 2021, doi: 10.35848/1347-4065/abfdc0.

[14] C. C. Shen, Y. H. Chou, and P. C. Li, "Pulse inversion techniques in ultrasonic nonlinear imaging," *J. Med. Ultrasound*, vol. 13, no. 1, pp. 3–17, 2005, doi: 10.1016/S0929-6441(09)60073-4.

[15] Q. Y. Ma, Y. Y. Qiu, B. Huang, D. Zhang, and X. F. Gong, "Difference-frequency

ultrasound generation from microbubbles under dual-frequency excitation," *Chinese Phys. B*, vol. 19, no. 9, 2010, doi: 10.1088/1674-1056/19/9/094302.

[16] V. L. Newhouse and P. M. Shankar, "Bubble size measurements using the nonlinear mixing of two frequencies," *J. Acoust. Soc. Am.*, vol. 75, no. 5, pp. 1473–1477, 1984, doi: 10.1121/1.390863.

[17] S. Chiou and F. Forsberg, "Harmonic and Fundamental Gray Scale Imaging of the Liver," pp. 1557–1563, 2007.

[18] C. P. Keravnou and M. A. Averkiou, "Harmonic generation with a dual frequency pulse," *IEEE International Ultrasonics Symposium, IUS*. pp. 1998–2001, 2013, doi: 10.1109/ULTSYM.2013.0510.

[19] Y. Li *et al.*, "Difference-Frequency Ultrasound Imaging with Non-Linear Contrast," *IEEE Trans. Med. Imaging*, vol. 39, no. 5, pp. 1759–1766, 2020, doi: 10.1109/TMI.2019.2957280.

[20] C. C. Shen, C. H. Cheng, and C. K. Yeh, "Phase-dependent dual-frequency contrast imaging at sub-harmonic frequency," *IEEE Trans. Ultrason. Ferroelectr. Freq. Control*, vol. 58, no. 2, pp. 379–388, 2011, doi: 10.1109/TUFFC.2011.1815.

[21] A. Bouakaz, M. Versluis, J. Borsboom, and N. De Jong, "Radial modulation of microbubbles for ultrasound contrast imaging," *IEEE Trans. Ultrason. Ferroelectr. Freq. Control*, vol. 54, no. 11, pp. 2283–2290, 2007, doi: 10.1109/TUFFC.2007.532.

[22] H. Azhari, *Basics of biomedical ultrasound for engineers*. 2010.

[23] J. Prince and J. Links, *Medical imaging signals and systems*. 2006.

[24] H. Azhari, J. A. Kennedy, N. Weiss, and L. Volokh, "Ultrasound Imaging," *From Signals to Image*, pp. 321–364, 2020, doi: 10.1007/978-3-030-35326-1_7.

[25] Q. Zhou, K. H. Lam, H. Zheng, W. Qiu, and K. K. Shung, “Piezoelectric single crystal ultrasonic transducers for biomedical applications,” *Progress in Materials Science*, vol. 66. pp. 87–111, 2014, doi: 10.1016/j.pmatsci.2014.06.001.

[26] R. Panda, *Development of novel piezoelectric composites by solid freeform fabrication techniques*. 1998.

[27] J. A. Jensen, “Linear description of ultrasound imaging systems, Notes for the International Summer School on Advanced Ultrasound Imaging,” p. 81, 2015.

[28] T. Szasz, “Advanced beamforming techniques in ultrasound imaging and the associated inverse problems,” Universit´e Toulouse 3 Paul Sabatier (UT3 Paul Sabatier).

[29] J. M. Mari and C. Cachard, “Acquire real-time RF digital ultrasound data from a commercial scanner,” no. January 2007, pp. 1–16, 2007.

[30] S. W. Smith, H. Lopez, and W. J. Bodine, “Frequency independent ultrasound contrast-detail analysis,” *Ultrasound Med. Biol.*, vol. 11, no. 3, pp. 467–477, May 1985, doi: 10.1016/0301-5629(85)90158-9.

[31] G. Montaldo, M. Tanter, J. Bercoff, N. Benech, and M. Fink, “Coherent plane-wave compounding for very high frame rate ultrasonography and transient elastography,” *IEEE Trans. Ultrason. Ferroelectr. Freq. Control*, vol. 56, no. 3, pp. 489–506, 2009, doi: 10.1109/TUFFC.2009.1067.

[32] J. Jensen, “Fast Plane Wave Imaging,” *Citation*, 2020, [Online]. Available: www.bme.elektro.dtu.dk.

[33] I. Karagoz and M. K. Kartal, “Evaluation of nonscanned mode soft-tissue thermal index in the presence of the residual temperature rise,” *Ultrasound Med. Biol.*, vol. 32, no. 5, pp. 741–750, May 2006, doi: 10.1016/J.ULTRASMEDBIO.2006.02.1404.

[34] T. Şen, O. Tüfekçioğlu, and Y. Koza, “Mechanical index,” *Anatol. J. Cardiol.*, vol. 15, no. 4, p. 334, 2015.

[35] G. Taraldsen, “A generalized Westervelt equation for nonlinear medical ultrasound,” *J. Acoust. Soc. Am.*, vol. 109, no. 4, pp. 1329–1333, 2001, doi: 10.1121/1.1344157.

[36] Y. Gong, D. Zhang, and X. Gong, “The nonlinear oscillation of encapsulated microbubbles in ultrasound contrast agents,” *AIP Conference Proceedings*, vol. 838. pp. 279–283, 2006, doi: 10.1063/1.2210362.

[37] N. Rognin, “Advances in Medical Ultrasound Imaging,” no. January, pp. 1–26, 2015.

[38] N. De Jong, P. J. A. Frinking, A. Bouakaz, and F. J. Ten Cate, “Detection procedures of ultrasound contrast agents,” *Ultrasonics*, vol. 38, no. 1, pp. 87–92, 2000, doi: 10.1016/S0041-624X(99)00071-2.

[39] B. R. Bollinger *et al.*, “Detection of stationary microbubbles in tissue,” *UHM*, vol. 36, no. 2, 2009, Accessed: Jul. 14, 2021. [Online]. Available: http://archive.rubicon-foundation.org.

[40] T. S. Desser and R. B. Jeffrey, “Tissue harmonic imaging techniques: Physical principles and clinical applications,” *Semin. Ultrasound CT MRI*, vol. 22, no. 1, pp. 1–10, 2001, doi: 10.1016/S0887-2171(01)90014-9.

[41] C. C. Shen and C. H. Lin, “Chirp-encoded excitation for dual-frequency ultrasound tissue harmonic imaging,” *IEEE Trans. Ultrason. Ferroelectr. Freq. Control*, vol. 59, no. 11, pp. 2420–2430, 2012, doi: 10.1109/TUFFC.2012.2474.

[42] P. N. Burns, D. Hope Simpson, and M. A. Averkiou, “Nonlinear imaging,” *Ultrasound Med. Biol.*, vol. 26, no. SUPPL. 1, pp. 19–22, 2000, doi: 10.1016/S0301-5629(00)00155-1.

[43] T. Ilovitsh *et al.*, "Enhanced microbubble contrast agent oscillation following 250 kHz insonation," *Sci. Rep.*, vol. 8, no. 1, pp. 1–15, Dec. 2018, doi: 10.1038/s41598-018-34494-5.

[44] M. A. Averkiou, M. F. Bruce, J. E. Powers, P. S. Sheeran, and P. N. Burns, "Imaging Methods for Ultrasound Contrast Agents," *Ultrasound Med. Biol.*, vol. 46, no. 3, pp. 498–517, 2020, doi: 10.1016/j.ultrasmedbio.2019.11.004.

[45] M. Emmer, H. J. Vos, D. E. Goertz, A. van Wamel, M. Versluis, and N. de Jong, "Pressure-Dependent Attenuation and Scattering of Phospholipid-Coated Microbubbles at Low Acoustic Pressures," *Ultrasound Med. Biol.*, vol. 35, no. 1, pp. 102–111, 2009, doi: 10.1016/j.ultrasmedbio.2008.07.005.

[46] J. Wu and J. Tong, "Measurements of the nonlinearity parameter B/A of contrast agents," *Ultrasound Med. Biol.*, vol. 24, no. 1, pp. 153–159, Jan. 1998, doi: 10.1016/S0301-5629(97)00207-X.

[47] D. W. Droste, R. Jürgens, D. G. Nabavi, G. Schuierer, S. Weber, and ; E Bernd Ringelstein, "Echocontrast-Enhanced Ultrasound of Extracranial Internal Carotid Artery High-Grade Stenosis and Occlusion," 1999. [Online]. Available: http://ahajournals.org.

[48] P. Frinking, T. Segers, Y. Luan, and F. Tranquart, "Three Decades of Ultrasound Contrast Agents: A Review of the Past, Present and Future Improvements," *Ultrasound Med. Biol.*, vol. 46, no. 4, pp. 892–908, 2020, doi: 10.1016/j.ultrasmedbio.2019.12.008.

[49] P. Ricci *et al.*, "Acta Radiologica Contrast-Enhanced Color Doppler Us in Malignant Portal Vein Thrombosis," 2000, doi: 10.1080/028418500127345703.

[50] M. Krix *et al.*, "Low Mechanical Index Contrast-Enhanced Ultrasound Better Reflects High Arterial Perfusion of Liver Metastases Than Arterial Phase Computed

Tomography," *Invest. Radiol.*, vol. 39, no. 4, pp. 216–222, 2004, doi: 10.1097/01.rli.0000116361.62063.b5.

[51] C. Balleyguier *et al.*, "New potential and applications of contrast-enhanced ultrasound of the breast: Own investigations and review of the literature," *European Journal of Radiology*, vol. 69, no. 1. pp. 14–23, 2009, doi: 10.1016/j.ejrad.2008.07.037.

[52] J. Foiret, H. Zhang, T. Ilovitsh, L. Mahakian, S. Tam, and K. W. Ferrara, "Ultrasound localization microscopy to image and assess microvasculature in a rat kidney," *Sci. Rep.*, vol. 7, no. 1, pp. 1–12, 2017, doi: 10.1038/s41598-017-13676-7.

[53] L. R. O. M. F.R.S., "VIII. On the pressure developed in a liquid during the collapse of a spherical cavity," *https://doi.org/10.1080/14786440808635681*, vol. 34, no. 200, pp. 94–98, Aug. 2009, doi: 10.1080/14786440808635681.

[54] P. Marmottant *et al.*, "A model for large amplitude oscillations of coated bubbles accounting for buckling and rupture," *J. Acoust. Soc. Am.*, vol. 118, no. 6, pp. 3499–3505, 2005, doi: 10.1121/1.2109427.

[55] T. Faez, M. Emmer, M. Docter, J. Sijl, M. Versluis, and N. de Jong, "Characterizing the Subharmonic Response of Phospholipid-Coated Microbubbles for Carotid Imaging," *Ultrasound in Medicine and Biology*, vol. 37, no. 6. pp. 958–970, 2011, doi: 10.1016/j.ultrasmedbio.2011.02.017.

[56] M. Bismuth, S. Katz, H. Rosenblatt, M. Twito, R. Aronovich, and T. Ilovitsh, "Acoustically Detonated Microbubbles Coupled with Low Frequency Insonation: Multiparameter Evaluation of Low Energy Mechanical Ablation," *Bioconjugate Chemistry*. 2021, doi: 10.1021/acs.bioconjchem.1c00203.

[57] P. J. Westervelt, "Parametric Acoustic Array," *J. Acoust. Soc. Am.*, vol. 35, no. 4, pp.

535–537, 1963, doi: 10.1121/1.1918525.

[58] G. S. He and S. H. Liu, “Second-Order Nonlinear (Three-Wave) Frequency Mixing,” *Adv. Nonlinear Opt.*, pp. 49–81, Feb. 2018, doi: 10.1142/9789813223059_0003.

[59] P. K. Tien, “Parametric amplification and frequency mixing in propagating circuits,” *Journal of Applied Physics*, vol. 29, no. 9. pp. 1347–1357, 1958, doi: 10.1063/1.1723440.

[60] R. H. Mellen, D. G. Browning, and W. L. Konrad, “Parametric Sonar Transmitting Array Measurements Propagation of Plane Sound Waves of Finite Amplitude in Nondissipative Fluids,” *Parametr. Acoust. Transm. Arrays J. Acoust. Soc. Am.*, vol. 49, p. 1481, 1971, doi: 10.1121/1.1912438.

[61] M. Yoneyama, J.-I. Fujimoto, and Y. Kawamo, “The audio spotlight: An application of nonlinear interaction of sound waves to a new type of loudspeaker design,” *Cit. J. Acoust. Soc. Am.*, vol. 73, p. 1532, 1983, doi: 10.1121/1.389414.

[62] N. Mujica, R. Wunenburger, and S. Fauve, “Scattering of Sound by Sound in the Vicinity of the Liquid-Vapor Critical Point,” *Phys. Rev. Lett.*, vol. 90, no. 23, p. 4, 2003, doi: 10.1103/PhysRevLett.90.234301.

[63] N. Ichida, T. Sato, and M. Linzer, “Imaging the nonlinear ultrasonic parameter of a medium,” *Ultrason. Imaging*, vol. 5, no. 4, pp. 295–299, Oct. 1983.

[64] D. Kim, J. F. Greenleaf, and C. M. Sehgal, “Ultrasonic imaging of the nonlinear parameter B/A: Simulation studies to evaluate phase and frequency modulation methods,” *Ultrasound Med. Biol.*, vol. 16, no. 2, pp. 175–181, Jan. 1990, doi: 10.1016/0301-5629(90)90146-4.

[65] D. Zhang, X. F. Gong, and X. Chen, “Experimental imaging of the acoustic nonlinearity

parameter B/A for biological tissues via a parametric array," *Ultrasound Med. Biol.*, vol. 27, no. 10, pp. 1359–1365, Oct. 2001, doi: 10.1016/S0301-5629(01)00432-X.

[66] M. W. Urban, S. Member, G. T. Silva, M. Fatemi, and J. F. Greenleaf, "Multifrequency Vibro-Acoustography," vol. 25, no. 10, pp. 1284–1295, 2006.

[67] M. Fatemi and J. F. Greenleaf, "Ultrasound-stimulated vibro-acoustic spectrography," *Science (80-.).*, vol. 280, no. 5360, pp. 82–85, Apr. 1998, doi: 10.1126/SCIENCE.280.5360.82.

[68] G. T. Silva and F. G. Mitri, "Difference-frequency generation in vibro-acoustography," *Phys. Med. Biol.*, vol. 56, no. 18, pp. 5985–5993, 2011, doi: 10.1088/0031-9155/56/18/013.

[69] G. T. Silva and A. Bandeira, "Difference-frequency generation in nonlinear scattering of acoustic waves by a rigid sphere," *Ultrasonics*, vol. 53, no. 2, pp. 470–478, 2013, doi: 10.1016/j.ultras.2012.08.015.

[70] S. Krishnan and M. O'Donnell, "Transmit aperture processing for nonlinear contrast agent imaging," *Ultrason. Imaging*, vol. 18, no. 2, pp. 77–105, 1996, doi: 10.1006/uimg.1996.0005.

[71] C. X. Deng, F. L. Lizzi, A. Kalisz, A. Rosado, R. H. Silverman, and D. J. Coleman, "Study of ultrasonic contrast agents using a dual-frequency band technique," *Ultrasound Med. Biol.*, vol. 26, no. 5, pp. 819–831, Jun. 2000, doi: 10.1016/S0301-5629(00)00217-9.

[72] R. Hansen and B. A. J. Angelsen, "Contrast imaging by non-overlapping dual frequency band transmit pulse complexes," *IEEE Trans. Ultrason. Ferroelectr. Freq. Control*, vol. 58, no. 2, pp. 290–297, 2011, doi: 10.1109/TUFFC.2011.1806.

[73] Y. N. Zhang, Y. N. Zhang, and S. C. Li, “Bubble dynamics under acoustic excitation with multiple frequencies,” *IOP Conference Series: Materials Science and Engineering*, vol. 72, no. Forum 1. 2015, doi: 10.1088/1757-899X/72/1/012003.

[74] J. A. Jensen, “Field: A Program for Simulating Ultrasound Systems,” *Med. Biol. Eng. Comput.*, vol. 34, no. 1, pp. 351–353, 1996.

[75] S. Qin and K. W. Ferrara, “A model for the dynamics of ultrasound contrast agents in vivo,” *J. Acoust. Soc. Am.*, vol. 128, no. 3, p. 1511, 2010, doi: 10.1121/1.3409476.

[76] T. Ilovitsh *et al.*, “Low-frequency ultrasound-mediated cytokine transfection enhances T cell recruitment at local and distant tumor sites,” *Proc. Natl. Acad. Sci. U. S. A.*, vol. 117, no. 23, pp. 12674–12685, 2020, doi: 10.1073/pnas.1914906117.

[77] Y. Huang, J. Yu, Y. Wang, S. Li, and Y. Chen, “Improvement of ultrasound contrast imaging with adaptive beamformer based on pulse inversion plane wave transmission,” *2016 URSI Asia-Pacific Radio Sci. Conf. URSI AP-RASC 2016*, pp. 1442–1445, 2016, doi: 10.1109/URSIAP-RASC.2016.7601401.

[78] A. Ilovitsh, T. Ilovitsh, and K. W. Ferrara, “Multiplexed ultrasound beam summation for side lobe reduction,” *Sci. Rep.*, vol. 9, no. 1, pp. 3–10, 2019, doi: 10.1038/s41598-019-50317-7.

[79] Y. Kono *et al.*, “Carotid Arteries: Contrast-enhanced US Angiography-Preliminary Clinical Experience,” *Radiology*, vol. 230, no. 2, pp. 561–568, 2004, doi: 10.1148/radiol.2302020318.

[80] G. Korpanty, J. G. Carbon, P. A. Grayburn, J. B. Fleming, and R. A. Brekken, “Monitoring response to anticancer therapy by targeting microbubbles to tumor vasculature,” *Clinical Cancer Research*, vol. 13, no. 1. pp. 323–330, 2007, doi:

10.1158/1078-0432.CCR-06-1313.

[81] J. Jiang, Y. Chen, Y. Zhu, X. Yao, and J. Qi, “Contrast-enhanced ultrasonography for the detection and characterization of prostate cancer: Correlation with microvessel density and Gleason score,” *Clinical Radiology*, vol. 66, no. 8. pp. 732–737, 2011, doi: 10.1016/j.crad.2011.02.013.

[82] T. R. Porter *et al.*, “Guidelines for the cardiac sonographer in the performance of contrast echocardiography: A focused update from the American society of echocardiography,” *Journal of the American Society of Echocardiography*, vol. 27, no. 8. pp. 797–810, 2014, doi: 10.1016/j.echo.2014.05.011.

[83] O. Solomon, R. J. G. Van Sloun, H. Wijkstra, M. Mischi, and Y. C. Eldar, “Exploiting Flow Dynamics for Superresolution in Contrast-Enhanced Ultrasound,” *IEEE Trans. Ultrason. Ferroelectr. Freq. Control*, vol. 66, no. 10, pp. 1573–1586, 2019, doi: 10.1109/TUFFC.2019.2926062.

[84] A. Ilovitsh, T. Ilovitsh, J. Foiret, D. N. Stephens, and K. W. Ferrara, “Simultaneous Axial Multifocal Imaging Using a Single Acoustical Transmission: A Practical Implementation,” *IEEE Trans. Ultrason. Ferroelectr. Freq. Control*, vol. 66, no. 2, pp. 273–284, 2019, doi: 10.1109/TUFFC.2018.2885080.

[85] A. Bouakaz, S. Frigstad, F. J. Ten Cate, and N. de Jong, “Super harmonic imaging: A new imaging technique for improved contrast detection,” *Ultrasound Med. Biol.*, vol. 28, no. 1, pp. 59–68, 2002, doi: 10.1016/S0301-5629(01)00460-4.

[86] J. Song, S. Kim, H. yeol Sohn, T. kyong Song, and Y. M. Yoo, “Coded excitation for ultrasound tissue harmonic imaging,” *Ultrasonics*, vol. 50, no. 6, pp. 613–619, 2010, doi: 10.1016/j.ultras.2010.01.001.

[87] L. Wu, X. Chen, G. Wang, and Q. Zhou, “Dual-frequency piezoelectric micromachined ultrasonic transducers,” *Appl. Phys. Lett.*, vol. 115, no. 2, 2019, doi: 10.1063/1.5097624.

[88] J. Yang *et al.*, “Characterization of an Array-Based Dual-Frequency Transducer for Superharmonic Contrast Imaging,” *IEEE Trans. Ultrason. Ferroelectr. Freq. Control*, vol. 68, no. 7, pp. 2419–2431, 2021, doi: 10.1109/TUFFC.2021.3065952.

[89] K. G. Brown and K. Hoyt, “Evaluation of nonlinear contrast pulse sequencing for use in super-resolution ultrasound imaging,” *IEEE Trans. Ultrason. Ferroelectr. Freq. Control*, vol. 75080, no. c, pp. 1–1, 2021, doi: 10.1109/tuffc.2021.3092172.

[90] D. Maresca, D. P. Sawyer, G. Renaud, A. Lee-Gosselin, and M. G. Shapiro, “Nonlinear X-Wave Ultrasound Imaging of Acoustic Biomolecules,” *Phys. Rev. X*, vol. 8, no. 4, p. 41002, 2018, doi: 10.1103/PhysRevX.8.041002.

[91] B. Benacerraf, “The use of obstetrical ultrasound in the obese gravida,” *Semin. Perinatol.*, vol. 37, no. 5, pp. 345–347, Oct. 2013, doi: 10.1053/J.SEMPERI.2013.06.012.

[92] R. J. G. Van Sloun *et al.*, “Super-Resolution Ultrasound Localization Microscopy through Deep Learning,” *IEEE Trans. Med. Imaging*, vol. 40, no. 3, pp. 829–839, 2021, doi: 10.1109/TMI.2020.3037790.

[93] T. R. Porter and F. Xie, “Myocardial Perfusion Imaging With Contrast Ultrasound,” *JACC Cardiovasc. Imaging*, vol. 3, no. 2, pp. 176–187, Feb. 2010, doi: 10.1016/J.JCMG.2009.09.024.

[94] V. Rafailidis, A. Charitanti, T. Tegos, E. Destanis, and I. Chryssogonidis, “Contrast-enhanced ultrasound of the carotid system: a review of the current literature,” *Journal of Ultrasound*, vol. 20, no. 2. pp. 97–109, 2017, doi: 10.1007/s40477-017-0239-4.

[95] K. Wei *et al.*, “Comparison of usefulness of dipyridamole stress myocardial contrast echocardiography to technetium-99m sestamibi single-photon emission computed tomography for detection of coronary artery disease (PB127 Multicenter Phase 2 Trial results),” *Am. J. Cardiol.*, vol. 91, no. 11, pp. 1293–1298, Jun. 2003, doi: 10.1016/S0002-9149(03)00316-3.

תקציר

אולטרסאונד היא שיטת ההדמיה הרפואית הנפוצה ביותר כיום בקליניקה, בין היתר מכיוון שהיא בטוחה לשימוש ולא פולשנית, מאפשרת עומק חדירה גדול, זולה ומספקת תמונות איכותיות בזמן אמת. מיקרובועות משמשות כחומר ניגוד בהדמיית אולטרסאונד, מכיוון שהניגודיות בינן לבין כלי הדם והרקמה הסובבת אותן, היא גבוהה. דימות הרמוני עם מיקרובועות, מבוסס על התכונות האי לינארית של מיקרובועות שיוצרות תדרים הרמוניים בתכולה התדרית של הסיגנל החוזר מהן. התכונה הזו מאפשרת להפריד את הסיגנל החוזר מהמיקרובועות ומההדים החוזרים מהרקמה הלינארית שמקיפה אותן. ע"י ביטול ההדים הלינאריים והשארת הסיגנל האי לינארי, ניתן לקבל תמונת אולטרסאונד של המיקרובועות. השיטה הנפוצה לעשות זאת, היא באמצעות שידור של שני פולסים של גלי קול בקוטביות הפוכה אל הרקמה, וסכימה של ההדים החוזרים, בשיטה המכונה Pulse-Inversion. בעוד ששיטה זו נמצאת בשימוש קליני, המכשולים העיקריים שלה, נובעים מהאי לינאריות של הרקמה עצמה ומהעוצמה החלשה של התדרים ההרמוניים ביחס לסיגנל הלינארי. כתוצאה מכך, דימות הרמוני סובל ממגבלות בקונטרסט (ניגודיות), ביחס אות לרעש ובארטיפקטים שנוצרים.

מטרת מחקר זה, היא לפתח טכניקת דימות הרמוני משופרת בזמן אמת של מיקרובועות. טכניקה זו מסתמכת על עירור של מיקרובועות עם גל קול המכיל ריבוב של שני תדרי אולטרסאונד שונים. כתוצאה מהתכונות האי לינאריות שלהן, המיקרובועות מייצרות אפקט של ערבוב תדרים שיוצר רכיבי תדר חדשים נוספים בספקטרום החוזר מהן, הכולל תדרי סכום והפרש של שני התדרים שנשלחו, בנוסף להרמוניות הסטנדרטיות של כל תדר מרכזי. באופן זה, ניתן להעצים את התגובה האי-לינארית של המיקרובועות ולשפר את איכות וניגודיות תמונת האולטרסאונד.

שיטת הדמיה זו מתבצעת בזמן אמת ומסתמכת על סופרפוזיציה של שני גלי קול בעלי תדרים שונים ויצירת גל קול אחד המרבב שני תדרים בו זמנית. הגל המתקבל, משולב בשידור סטנדרטי של דימות הרמוני מסוג Pulse-Inversion, ע"י מתמר הדמיה ובאמצעות שימוש במחולל אותות במערכת אולטרסאונד מתכנתת. בקליטה, בניית התמונה נעשית באופן אוטומטי ע"י מערכת האולטרסאונד, כפי שמתבצע בדימות הרמוני, ללא צורך בעיבוד תמונה נוסף.

השיטה המוצעת מתוארת בצורה אנליטית בסימולציות נומריות, שמשתמשות במודלים של חיזוי התנהגות המיקרובועות בתגובה לאולטרסאונד, כדי לוודא את הופעת תדרי הסכום וההפרש בתגובה לעירור המורכב משני התדרים. הערכת

השיפור באיכות תמונת האולטרסאונד המתקבלת, מתבצעת ע"י הדמיית פנטום מדמה רקמה, המכיל תמיסת מיקרובועות. השיטה המוצעת הניבה שיפור ניגודיות מקסימלי של 3.71dB בהשוואה לדימות הרמוני מבוסס Pulse-Inversion סטנדרטי, וכן מאפשרת הפחתה של האינדקס המכאני פי 4.5 מבלי לפגוע באיכות התמונה המתקבלת.

אוניברסיטת תל אביב

הפקולטה להנדסה ע"ש איבי ואלדר פליישמן

בית הספר לתארים מתקדמים ע"ש זנדמן-סליינר

ריבוב תדרי אולטרסאונד כפלטפורמה לדימות הרמוני מועצם עם מיקרובועיות

חיבור זה הוגש כעבודת גמר לקראת התואר "מוסמך אוניברסיטה" בהנדסה ביו-רפואית

על-ידי

קרן קרלינסקי

העבודה נעשתה במחלקה להנדסה ביו-רפואית

בהנחיית ד"ר טלי אילוביץ'

אוניברסיטת תל אביב

הפקולטה להנדסה ע"ש איבי ואלדר פליישמן

בית הספר לתארים מתקדמים ע"ש זנדמן-סליינר

ריבוב תדרי אולטרסאונד כפלטפורמה לדימות הרמוני מועצם עם מיקרובועיות

חיבור זה הוגש כעבודת גמר לקראת התואר "מוסמך אוניברסיטה" בהנדסה ביו-רפואית

על-ידי

קרן קרלינסקי

העבודה נעשתה במחלקה להנדסה ביו-רפואית

בהנחיית ד"ר טלי אילוביץ'